

University of St Andrews



Full metadata for this thesis is available in
St Andrews Research Repository
at:

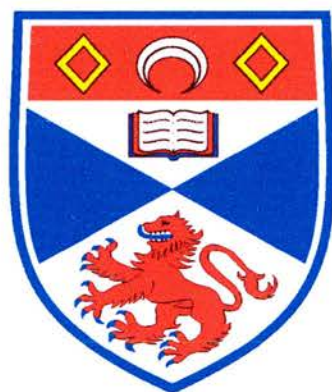
<http://research-repository.st-andrews.ac.uk/>

This thesis is protected by original copyright

Structural investigations of some Novel doped Zirconias with potential as Solid Oxide Fuel Cell Electrolytes

A thesis presented for examination for the title of
Doctor of Philosophy

Jeremy Dobson



University of St. Andrews

February 2002



TL E250

I, Jeremy William Louis Dobson, hereby certify that this thesis, which is approximately 30,000 words in length, has been written by me, that it is the record of work carried out by me and that it has not been submitted in any previous application for a higher degree.

Date 18-10-02

Signature of Candidate

I was admitted as a research student in September 1997 and as a candidate for the degree of Doctor of Philosophy in September 1998, the higher study for which this is a record was carried out in the University of St. Andrews between 1997 and 2002.

Date 18-10-02

Signature of Candidate

I hereby certify that the candidate has fulfilled the conditions of the Resolution and Regulations appropriate for the degree of Doctor of Philosophy in the University of St. Andrews and that the candidate is qualified to submit this thesis in application for that degree.

Date 18/10/02

Signature of Supervisor

In submitting this thesis to the University of St. Andrews I understand that I am giving permission for it to be made available for use in accordance with the regulations of the University Library for the time being in force, subject to any copyright vested in the work not being affected thereby. I also understand that the title and abstract will be published, and that a copy of the work may be made and supplied by any *bona fide* library or research worker.

Date 18-10-02

Signature of Candidate

Table of contents

Abstract	4
Chapter 1 – Introduction	10
Chapter 2 – Experimental and Theory	47
Chapter 3 – Boron Doping of YSZ	84
Chapter 4 – EXAFS Studies on Doped Zirconia	112
Chapter 5 – Neutron Diffraction Studies on Doped Zirconia	162
Chapter 6 – Discussion and Conclusions	177

Abstract

This research has concentrated on the doping of the already well-studied zirconia system, and the structural changes caused by this doping. These were all considered as potential electrolyte materials for solid oxide fuel cells.

Initially, boron doping was investigated as a potential new method of doping that had yet to be studied. Borate loss was found to be a major problem, but this could be worked around using carefully controlled preparations. Results from structural investigations were ambiguous, with XRD showing little change in the structure, but also showing no second crystalline phase. NMR showed the boron to be in a similar environment to the system YBO_3 yet IR showed differences between the two systems. Thus it was concluded that boron was inserted into the structure in a manner similar to the YBO_3 structure.

EXAFS studies were conducted on three doping systems, yttria doping (YSZ), scandia doping (SSZ) and dual doping with both yttria and scandia (YScSZ). These systems were found to have subtle but extremely important differences. In YSZ, vacancies were found to be clustered preferentially around the zirconium ions, until doping levels became so high that yttrium co-ordination also had to decrease. Multi cluster refinements confirmed this theory and suggested the possibility of microdomain formation in this system. In SSZ vacancies were more evenly distributed through the system, with both zirconium and scandium showing a preference for a six fold co-ordination system, which is not possible in the fluorite structure, suggesting a local structure perhaps closer to rutile may be likely. Evidence

of microdomains was also seen. The YScSZ showed most similarity to the SSZ system, with lowered co-ordination numbers on all three metals, and evidence for short range six co-ordinate structure and the formation of microdomains.

Neutron diffraction work on the YScSZ showed modulation in the background which was attributed to the formation of microdomains. There was also considerable disorder on the metal site which fell linearly with reducing scandium concentration. The fact that scandium is off site yet the yttrium is on is further evidence that the local structure around scandium is distorted six co-ordinate rather than fluorite.

Acknowledgements

No work is done in a vacuum, and this is no exception. Many people have helped me during my doctorate, and I would like to thank a few of them, in no particular order.

Firstly, my boss, Professor John Irvine, for his continuing belief throughout my studies. He hates being called Professor, so I'll just leave it in there for him to find later.

Secondly, to Juliet, for always being there. Not content with just making my life worth living, you even found time to read the thesis for me. This would never have been finished without your love and support, and I will always be grateful for it.

Thirdly, to the research group, for friendship and coffee, in equally large quantities. In particular, John Bradley and Julian Tolchard, with whom I shared a flat as well as an office, have my gratitude for helping and hindering me along the way. Paul Connor was always on hand to discuss cricket, films, kites, the weather and occasionally even chemistry, and his reading of the thesis is much appreciated. To everyone who suffered Daresbury food with me, Alan, David, John, Derek, Paul and Martin, your help is much appreciated. We actually got some data, no matter how unlikely it may have seemed at the time.

Finally, my parents, who as well as offering moral support and encouragement actually read the thesis for me. My father claims to understand it all, which is more than I can sometimes claim. My brother Patrick also deserves my thanks for reminding me a PhD wasn't really bad by becoming an accountant.

Abbreviations used in this work

Within each chapter I have attempted to explain all acronyms as they come up. However, as Solid State Chemistry is awash with acronyms, they are gathered here as well to aid the reader.

AFC	Alkali Fuel Cell
BCC	Body Centred Cubic – a type of unit cell
CHP	Combined Heat and Power
ESRF	European Synchrotron Radiation Source
EXAFS	Extended X-ray Absorption Fine Structure
FCC	Face Centred Cubic – a type of unit cell
FWHM	Full Width Half Maximum
GT	Gas Turbine
HRPD	High Resolution Powder Diffraction – an instrument at RAL
LSGM	Lanthanum Gallate doped with strontium and magnesium – a new highly conducting oxide ion conductor
MAS	Magic Angle Spinning
MCFC	Molten Carbonate Fuel Cell
NASA	National Aeronautics and Space Administration
NMR	Nuclear Magnetic Resonance
NN	Nearest Neighbour
NNN	Next Nearest Neighbour
NPD	Neutron Powder Diffraction – an instrument at Studsvik
PAFC	Phosphoric Acid Fuel Cell
PEMFC	Polymer Exchange Membrane Fuel Cell
PFC	Polymer Fuel Cell
PTFE	Polytetrafluorethylene, or TEFLON®, a polymer made entirely of carbon and fluorine. Very stable and hydrophobic.
RAL	Rutherford Appleton Laboratories
ScSZ	Scandia stabilised Zirconia
SOFC	Solid Oxide Fuel Cell
TEY	Total Electron Yield – a form of EXAFS

XRD	X-Ray Diffraction
XRF	X-Ray Fluorescence
YScSZ	Co doped yttria and scandia stabilised zirconia
YSZ	Yttria stabilised Zirconia

Writing is easy. All you do is stare at a blank sheet of paper until drops of blood form on your forehead. - Gene Fowler, Author (1890 - 1960)

Introduction

FUEL CELLS	12
THE BASIC CONCEPTS	12
A BRIEF HISTORY OF FUEL CELLS	13
THE CASE FOR FUEL CELLS	15
FUEL ISSUES WITH FUEL CELLS	19
TYPES OF FUEL CELLS	20
Alkali Fuel Cell (AFC)	21
Polymer Fuel Cells/Proton Exchange Membrane fuels cells (PEM/PEMFC)	22
Phosphoric Acid Fuel Cell (PAFC)	24
Molten Carbonate Fuel Cell (MCFC)	24
Solid Oxide Fuel Cell (SOFC)	25
SOLID OXIDE FUEL CELLS IN MORE DETAIL	26
Components of a solid oxide fuel cell	27
The Electrolyte	28
The Anode	29
The Cathode	30
SOLID OXIDE FUEL CELL RESEARCH GOALS	30
ZIRCONIA	33
STABILISATION OF FLUORITE ZIRCONIA	35
YTTRIA STABILISED ZIRCONIA (YSZ)	36

SCANDIA STABILISED ZIRCONIA (SCSZ)	40
CO-DOPED YTTRIA AND SCANDIA STABILISED ZIRCONIA (YSCSZ)	41
OTHER STABILISED ZIRCONIAS	42
REFERENCES	43

This thesis relates to an investigation of various doped zirconia materials that are considered to be potential electrolytes for solid oxide fuel cells. As an introduction to this work, the basics of fuel cells and their operation are discussed. A more detailed description of solid oxide fuel cells (SOFCs) is then presented before moving on to introduce the zirconia materials and oxide ion conduction.

Fuel Cells

The Basic Concepts

Fuel cells are devices for the electrochemical generation of electrical energy from oxidation of hydrogen or hydrocarbon fuel. Similarly to batteries, they convert chemical energy into electrical energy, but this takes the form of electrical generation rather than storage of energy.

Operation is very simple. Fuel enters the cell on one side and an oxidant gas (usually air or oxygen) enters on the other. The conducting species is ionised at the electrode and crosses the electrolyte to react in an electrochemical combustion at the

other electrode. The electrons released by this pass through an external circuit, driving a load en route, to complete the circuit. An example system is shown in Figure 1.1.

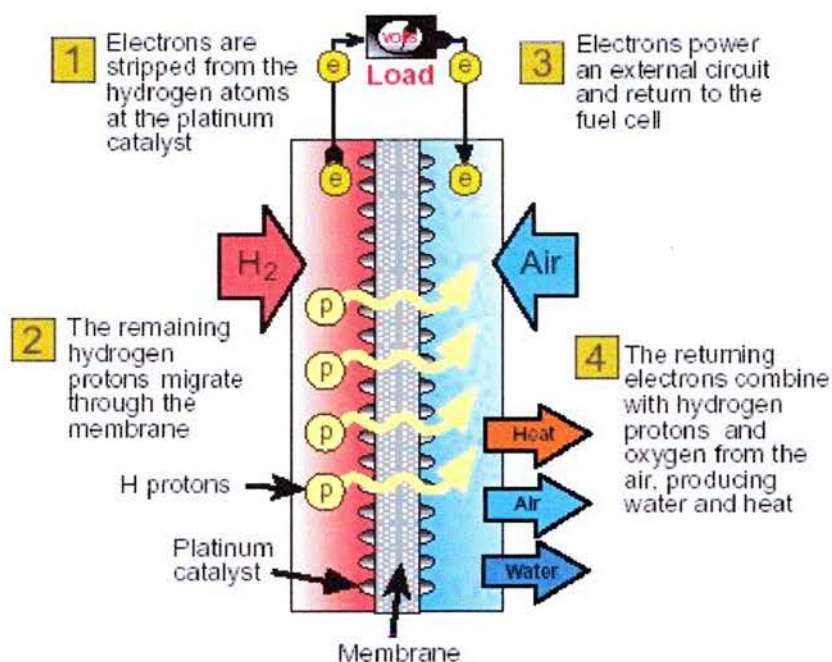


Figure 1.1 – How a fuel cell works, in this case a PEMFC. ¹

A Brief History of Fuel Cells

The production of a voltage when working with hydrogen and oxygen under electrochemical conditions was probably first observed in the early part of the nineteenth century. ² The first correct analysis of the effect was from Schönbein in 1839 ³ and the first fuel cell, a hydrogen-oxygen cell using platinum electrodes, was built by William Grove in 1845. ⁴ The further work done by Grove on his ‘Gas Battery’ ^{5,6} and his work in trying to encourage its use have earned him the accolade as the father of the fuel cell. It is worth noting that this work was performed long before

the invention of the internal combustion engine. Grove's own picture of his device is shown in Figure 1.2.

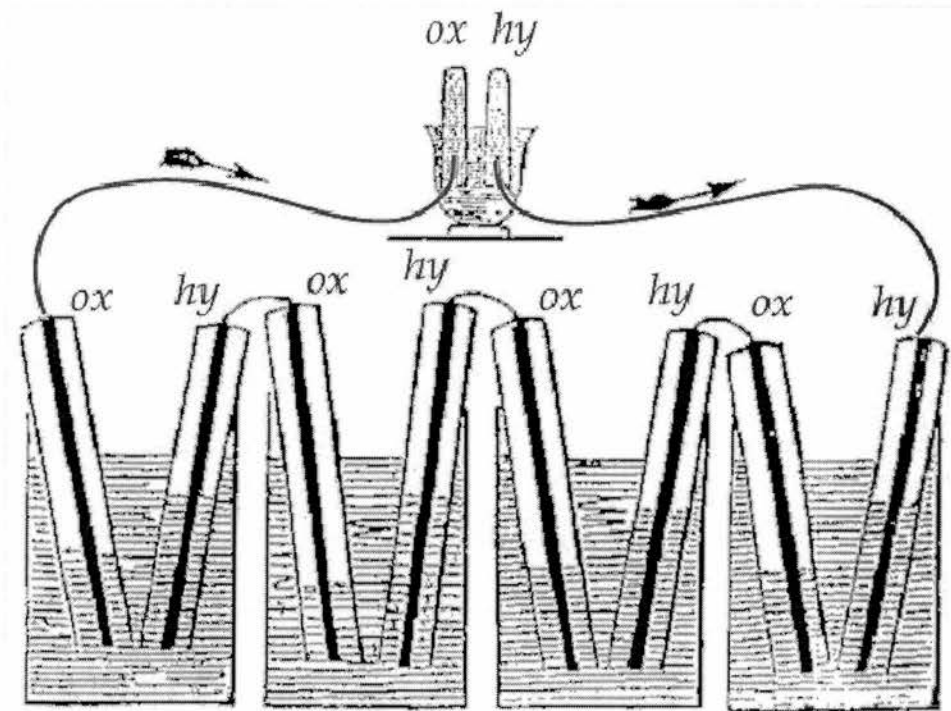


Figure 1.2 – William Grove's own picture of his 'gas battery'

After Grove's invention, there was some effort, mainly from Grove himself, to commercialise the fuel cell for electricity production, but it never took off. Von Siemens' invention of the dynamo in 1866 killed off the last commercial interest in the fuel cell as the dynamo could generate electricity more effectively using existing technologies, such as wind and water wheels, and could also be driven by prime movers powered by readily available fuels like coal, whereas the fuel cell needed pure, expensive hydrogen. The rest is history.

The fuel cell thus remained nothing more than an academic curiosity for many years. The first fuel cells to be used for any real purpose were employed in the 1960's,

when NASA used fuel cells to power the Gemini and Apollo spacecraft.⁷ The other options, nuclear and solar power, had been considered too risky and too inefficient respectively. NASA still uses fuel cells to provide electricity and water for the space shuttle.

In more recent times, there has been a gradual shift in the public perception of environmental issues, caused by the increasing number of high profile issues such as the degradation of the atmospheric ozone layer. This has caused a re-examination of how we use energy and how we cause pollution. While this has only recently started, it has allowed fuel cells to enjoy something of a renaissance. Fuel cells, of various types, have been touted as potential solutions to these pressing environmental concerns in both the popular press^{8,9} and the scientific¹⁰ and technical¹¹ press.

The Case for Fuel Cells

The main benefit of the fuel cell system over conventional turbine systems is that it is far more efficient and, with the correct fuels, far cleaner. The high efficiency of fuel cells in comparison to other methods of power generation arises from the Carnot Limitation of efficiencies in heat engines. The Carnot equation is as follows¹²:

$$\text{Carnot Efficiency} = 1 - T_c/T_h$$

Thus, the maximum efficiency is dependent solely on the difference in temperature between the hot sink and the cold sink and efficiency only tends towards unity as T_h tends towards infinity or T_c tends towards zero.

As an example, a typical power station using superheated steam at 550°C and a cold sink at 100°C has a maximum efficiency of roughly 55% and probably a practical efficiency, because of other losses, of more like 20-25%.¹²

Precise measurement of efficiencies in fuel cell systems is the subject of some debate,^{13,14} but Siemens-Westinghouse claim an efficiency of 73% with a combined heat and power system (CHP) for a 100kW SOFC demonstration system at Arnhem in the Netherlands and predict a potential electrical efficiency of up to 57% for SOFCs and 70% electrical efficiency for combined solid oxide fuel cell – gas turbine (SOFC-GT) systems.¹⁵ By direct electrochemical conversion of the fuel into energy and end products, rather than through wasteful heating of water to drive turbines, fuel cells are not restricted by the Carnot limitation and may have an electrical efficiency of up to 70%, or higher if the waste heat is used in a combined heat and power plant.

It has long been known that human activity affects the environment and the land around us. The Victorians complained of the London smog caused by the many coal fires and Edinburgh was called “Auld Reekie” for centuries. However, it is only recently that the true scale of these effects has been fully realised. The hole discovered in the Antarctic ozone layer in the 1970s, its explanation in the 1980s, and more recent debates on global warming are finally bringing acceptance that humans are massively changing the world through their actions, and not necessarily for the good.

The issue which is perceived as the most serious is the so-called “Greenhouse effect”, where certain heat trapping gases such as carbon dioxide and methane build up

in the atmosphere, causing the average temperature of the planet to rise and thus change the climate. The effect has been debated for many years but is now accepted as real by the majority of scientists. It is also now widely accepted that the main cause of this effect is human activity.

The largest contributor to this effect is carbon dioxide, and fuel cells are seen as a potential solution. Fuel cells powered by hydrogen would emit only water, with minimal greenhouse repercussions, unlike a coal burning power station which would also emit a large amount of carbon dioxide and other gases. Even a fuel cell utilising a hydrocarbon fuel would, due its high efficiency have a smaller emission of carbon dioxide (per unit of work produced) than a conventional power source such as an internal combustion engine.

While the greenhouse effect is widely (if not totally) accepted among scientists as a serious and human-caused problem, this acceptance is not so widespread among governments and industrialists. However a secondary benefit of the high efficiencies of fuel cells is that they use less fuel, thus conserving supplies of fossil fuels, reducing costs and dependency on imported fuels. This is of great concern to many governments due to the unstable geo-politics of most oil producing regions and ultimately because of the essentially limited amount of fossil fuels available.

The liberalisation of energy markets across the world may also benefit the fuel cell, with more companies using novel approaches to power generation and competing to sell their electricity to consumers. The marketing benefit of selling “Green” electricity from fuel cells to conservation-minded consumers could well be

considerable. Additionally, the initial capital cost of a fuel cell stack should be much lower than that for a coal fired power station, meaning a quicker return on investment.

Finally, the mode of operation and fuel choices of fuel cells offer several ancillary benefits. They are quiet, having few or no moving parts. They emit few pollutants, mainly due to their requirements for clean fuels. The removal of particulates (which fuel cells do not emit) alone from car exhaust would save 50,000 to 60,000 lives a year in the USA ¹⁶ alone. Fuel cells are also generally modular, with small individual cells stacked together for the job required. This makes them very customisable, being suited for a wide range of tasks depending solely on the size of the stack.

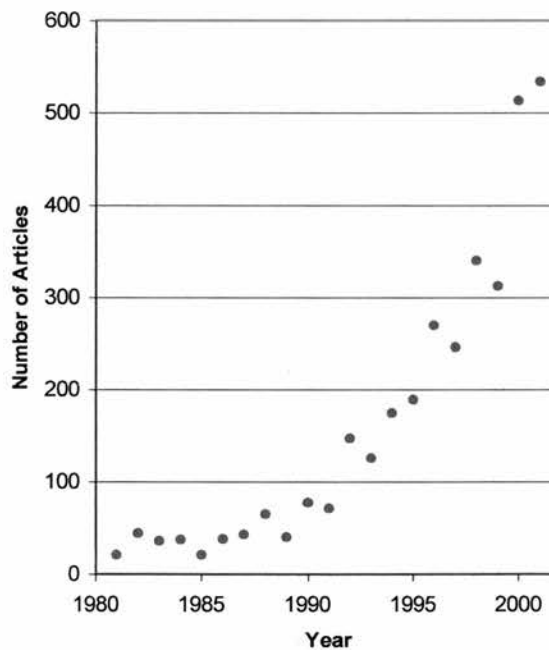


Figure 1.3 - Growth of Fuel Cell Research

(Papers mentioning "Fuel Cell" recorded in the Science Citation database ¹⁷)

As a result of all this, research in the general field of fuel cells has increased exponentially in the last few years, as a quick search on a database such as the Web of Science will show. This is demonstrated in the graph in Figure 1.3.

Fuel Issues with Fuel Cells

The fuel of choice for fuel cells of all forms would be hydrogen. This has caused several commentators to talk about the emergence of a “hydrogen economy”. The main benefits of hydrogen as a fuel are that it is clean and renewable. The combustion of hydrogen in air produces only water, which has a minimal environmental impact. Depending on its method of production, hydrogen is also renewable in a way that fossil fuels can never be.

Of course, there are several problems with hydrogen as a fuel. The hydrogen must be produced in some way, either on-site (with a loss of overall efficiency) or off-site (with storage and transportation difficulties). There are also safety issues to be considered.

There are several methods for the production of hydrogen, including the on site reformation of a hydrocarbon, usually a fossil fuel or methanol, or off-site by the electrolysis of water, possibly using another ‘clean’ energy source such as wind or solar power. More adventurous methods, such as the controlled action of sunlight on algae in stagnant ponds¹⁸, have also been postulated.

A major source of concern about the use of hydrogen as a fuel is its flammability and explosive nature, as illustrated in public consciousness by the destruction of the hydrogen filled Zeppelin *Hindenburg* in 1937. However, while hydrogen is dangerous and should be treated with caution, the hydrocarbon fuels in current use are no less dangerous, yet there is a safe storage and distribution network in place for these fuels. On the subject of the *Hindenburg*, the facts of the accident are that the fire was caused by the skin of the Zeppelin rather than the fuel itself.¹⁹ As almost two thirds of the passengers survived, rather better than many modern aircraft accidents, the accident was not as severe as it has appeared in popular folklore. The dangers are merely different from, rather than greater than, those posed by fossil fuels.

As there is currently little hydrogen produced, and that which is produced is usually produced inefficiently, there is a strong case for fuel cells running on hydrocarbons, probably methanol or natural gas. If the methanol is from a crop source, similar to the Brazilian 'Gasohol', then the process is carbon neutral. Otherwise, they are still environmentally beneficially from their higher efficiencies.

Types of fuel cells

There are five main types of fuel cell that, by convention, are grouped by their electrolyte, although the temperature of operation is also a good way to separate them. They are described briefly in Table 1.1, below, and discussed in greater detail afterward.

Table 1.1 – Types of Fuel Cell ²⁰

Type	Electrolyte Material	Charge Carrier	Temperature of operation	Application
Alkaline	NaOH or KOH	OH ⁻	50-200°C	Military and Space. Failed experiments in transportation.
Proton Exchange Membrane	Conducting Polymer (e.g. NAFION)	H ⁺	50-200°C	Transport and small scale. Probably the best developed cell.
Phosphoric Acid	Phosphoric acid supported in a SiC matrix	H ⁺	50-200°C	Small scale CHP. Many 200kW Stacks.
Molten Carbonate	Li, K or NA carbonate in a LiAlO ₂ matrix	CO ₃ ²⁻	~650°C	Distributed power generation and CHP. Up to MW Capacity.
Solid Oxide	Proton or oxide ion conducting ceramic	O ²⁻ or H ⁺	500-1000°C	Distributed power generation and CHP. 2kW to several MW.

Alkali Fuel Cell (AFC)

Alkali fuel cells are low temperature fuel cells made with an alkaline electrolyte, usually sodium or potassium hydroxide, that conducts OH⁻ ions. The principles for these have been known since at least 1902, ²¹ but they were first practically demonstrated in the 1940s and 1950s by F. T. Bacon at Cambridge. They were then employed by NASA in the Apollo space missions and have been used by NASA ever since. ²²

The success of polymer fuel cells has diminished the opportunities for alkali fuel cells and there are few examples of them working at the moment. Ze Tek Power plc demonstrated a prototype London cab running on an alkali fuel cell,²³ but this company has gone into compulsory administration, as of the 5th of November 2001.²⁴ Even the space shuttle is to have a PEMFC in the near future,²⁵ thus losing the AFC its only traditional area of dominance.

The major problems with the AFC are its slow reaction rate and the fact that carbon dioxide reacts with the electrolyte. This means it cannot be used with air as an oxidant. The corrosive nature of the electrolyte can also cause problems, particularly if there is any chance of damage to the cell, such as in an automotive application. The main benefit of the alkali fuel cell is that it does not require especially exotic or expensive materials.

It is possible to see a use for these fuel cells in a regenerative solar power system, where a renewable source would split water to form hydrogen and oxygen which the cell would recombine overnight, guaranteeing full-time electricity. This would overcome the problems with CO₂.

Polymer Fuel Cells/Proton Exchange Membrane fuels cells (PEM/PEMFC)

Proton exchange membrane fuel cells were first developed in the 1960s by General Electric for the early manned space missions of NASA,²² although they were soon superseded by alkali fuel cells. This was because they needed a considerable

amount of platinum catalyst in their electrodes and had complex water management issues, so the AFC was seen as an easier option.

The first crucial step in their development was the development of NAFION® by DuPont in 1967, which quickly became a standard for PEMFCs. NAFION is a form of Polytetrafluorethylene (PTFE) modified with sulphonate groups on side chains. The bulk PTFE is highly hydrophobic whereas the sulphonate is highly hydrophilic. Thus, when the polymer is moist it becomes an excellent conductor of protons from sulphonate group to sulphonate group. However, the water management is extremely complex, as too much water will impede the gas flow in the electrodes. Thus water management is a major area of research, with the ultimate aim being management using the water produced from the oxidation of the hydrogen fuel.

Recent development of the PEMFC has been made possible by great improvement in catalyst technologies. As far less platinum is required, down from 28 mgcm⁻² in its earliest NASA incarnations to 0.2 mgcm⁻² in a modern system, the cost of the platinum is no longer a limiting factor. Much of the renaissance of the PEMFC is due to the work of Ballard Power systems of Vancouver,²⁶ who now have contracts to provide several large car manufacturers with fuel cell power systems.

Due to its scalability (it has been proposed for uses from laptop computers to factory stack systems) and the backing of several very large car manufacturers, the polymer fuel cell is probably the closest to full commercialisation of any fuel cell system.

Phosphoric Acid Fuel Cell (PAFC)

In this cell the electrolyte is H_3PO_4 supported in the pores of silicon carbide particles, which are, in turn, held together by PTFE. The electrodes are made of carbon black, impregnated with platinum or other noble metal catalyst. The electrode reactions take place on the surface of the catalyst.

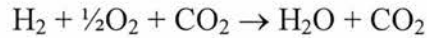
PAFCs are highly tolerant of CO_2 and can use simple hydrocarbons as fuel. However, the temperature must be carefully managed, as at temperatures below 42°C the electrolyte freezes and causes stress in other components and at high temperature the electrolyte evaporates.

PAFCs are generally aimed at stationary power uses. It is one of the best developed of all types of fuel cells and many are currently being tested around the world, generally in the 50 to 200 kW range, but there are stacks of up to 5 MW size, being run by companies such as Toshiba. The power they produce is still relatively expensive, and one of the major research goals is to lower the cost of fabrication.

Molten Carbonate Fuel Cell (MCFC)

Molten Carbonate Fuel Cells are medium/high temperature cells made with a carbonate electrolyte that conducts CO_3^{2-} ions. They are aimed at stationary power uses, in particular as combined heat and power (CHP) solutions.

The electrolyte consists of Li_2CO_3 and K_2CO_3 , or Li_2CO_3 and Na_2CO_3 , set in a LiOAlO_2 matrix. It is peculiar in being the only fuel cell to require carbon dioxide to function. The general reaction for the cell is given below, with CO_2 on both sides as it is the only conducting species.



The main benefits of the MCFC come from the high temperature of operation. Similarly to the solid oxide fuel cells that form the main aim of this thesis, the high temperature can be used to reform hydrocarbons internally and the hot exhaust gases can be used for heating directly (in a CHP system) or to drive a turbine as a so-called “bottoming cycle”.

The main disadvantage of the MCFC is the corrosive nature of the electrolyte, which makes for stringent construction and material requirements and a relatively short life span. The requirement for CO_2 also calls for this to be managed to ensure a steady supply at the cathode for conduction to be maintained.

Solid Oxide Fuel Cell (SOFC)

Solid Oxide Fuel Cells are medium to high temperature fuel cells, using oxide ion or proton conducting ceramics as electrolytes. They are entirely solid state devices and are generally being developed for distributed power generation.

While a high temperature heat engine can also achieve a high theoretical efficiency, SOFCs are often favoured as they produce high quality heat and hot exhaust gas as a by product which can be used for heating purposes in a CHP, for preheating the fuel itself, for the internal reformation of a hydrocarbon fuel or for driving an ancillary turbine generator in a bottoming cycle.

The components and principles of a solid oxide fuel cell are discussed in greater detail later on in this chapter.

Solid oxide fuel cells in more detail

The concept of the solid oxide fuel cell depends on ionic conductivity; the conduction of either hydrogen or oxygen ions across a solid electrolyte. This will be explained in greater detail later in the chapter. Oxide ion conductivity was first demonstrated by Nernst²⁷ in 1899. His compound, which became known as the Nernst Mass, was zirconia doped with 15 wt % yttria that he used as a filament for a lamp, an idea that never caught on. The idea was further developed in 1935 when Schottky²⁸ suggested that the Nernst Mass could be used as the electrolyte in a high temperature fuel cell. In 1937, Baur and Peris²⁹ demonstrated the first ceramic fuel cells. They used doped zirconia electrolytes, but the current generated was insufficient to make them anything but an academic curiosity.

It wasn't until the 1940s that the first practical ceramic fuel cells began to be developed in Germany and experiments with zirconia ceramic oxide ion conductors began in the 1950s. The development of modern SOFCs was started in the U.S. in the

1960s. The two major forces were Westinghouse (who pioneered the tubular cell) in the U.S. and Siemens (who pioneered the planar cell) in Germany. These two companies eventually merged a few years ago to form Siemens Westinghouse. The new company inherited both sets of technology (planar and tubular) and have decided to continue with only the tubular design.

There are now several companies developing fuel cells for commercialisation, such as Sulzer*Innotec* in Switzerland, Ceramic Fuel Cells Ltd in Australia and Accumetrics and SOFCo in the U.S.. With so many companies beginning to put serious research and money into commercialisation, the SOFC should become a mainstay of modern power generation.

Components of a solid oxide fuel cell

There are four main components that make up a solid oxide fuel cell. These are the anode, cathode, electrolyte and interconnect. While each component has distinct requirement, there are also several requirements that are the same for all the components.

Each component has to be stable, ideally for at least 50,000 hours, at operating temperature, typically 700°C to 1000°C. The materials must be chemically compatible with the adjoining components. They must also have similar expansion coefficients to their neighbours, otherwise the cell will crack on thermal cycling. Ideally, the materials will also be relatively cheap and easily fabricated in conjunction with each other.

The Electrolyte

The electrolyte is considered first as it is the part usually chosen first in system design, thus the other sections have to conform to it, rather than the other way around.

The ideal electrolyte should be a good ionic conductor but not an electronic conductor, otherwise it will short circuit some of the generated electricity across the electrolyte. As an aside, if an electrolytic material has an extremely high ionic conductivity and some electronic conductivity, it could still be a useful electrolyte if its net ionic conductivity (ionic minus electronic) is higher than that of alternative materials, as it would still have a higher power density, or if it had other (for example, manufacturing or cost) benefits. An electrolyte must also be stable at high temperature and in both the oxidising and reducing atmospheres present in the cell. It should also be dense to prevent the mixing of fuel and oxidant. As in all commercial systems, cost is also an important issue.

The traditional material of choice has been yttria stabilised zirconia (YSZ), which has been used since the very early days on account of its relatively high ionic conduction and its good stability. Much work has been performed on various types of doping of this material, and much work has also been done on finding high conducting alternatives, but it still remains the electrolyte of choice in most test-bed systems.

Some prototype systems use a proton conducting electrode, where the charge carrier is H^+ rather than O^{2-} . This has benefits of not diluting the fuel stream as the reaction take place on the oxidant side of the cell, with the water (from the oxidation of

the hydrogen) exiting in the air stream rather than the fuel stream. For systems like these, a completely different set of materials is needed, such as is demonstrated in the work of Kreur.³⁰

The Anode

The anode is the fuel electrode, where the fuel is oxidised. It must conduct both ionically and electrically and provide reaction sites for the conducted oxygen to react with the fuel and release its electrons. The anode has to be stable in the highly reducing environment of the hot fuel gas. It should also be chemically and morphologically compatible with the electrolyte and supporting structure. It should also be porous to allow the passage of fuel. Additionally, if the fuel is to be internally reformed in the cell, rather than an external reformer, the anode has to provide catalytic sites for this reformation to take place.

The traditional material is a cermet (ceramic metal composite) of nickel and yttria stabilised zirconia. This is stable with the electrolyte as it is based on YSZ. The YSZ provides the ionic conductivity and the nickel provides the electronic conductivity. However, there are considerable problems with Ni/YSZ cermets. As the conduction pathways of the electrons and the oxide ions is different, reactions can only take place at the so called 'triple point' where fuel, nickel and YSZ all meet, reducing the maximum power density. They cannot be used with hydrocarbon fuels as nickel is a catalyst for the cracking of hydrocarbons, which can result in the formation of carbon and the 'coking' of the anode, preventing further use without cleaning. Thus, there has been

considerable research into alternate materials, particularly mixed conductors to avoid these problems.

The Cathode

The main function of the cathode is to provide reaction sites for the electrochemical reduction of the oxidant. It must conduct both ionically and electrically and should also be porous to allow the passage of the oxidant gas. It has to be stable at the high temperatures of operation and should also be chemically and morphologically compatible with the electrolyte and supporting structure.

Doped Lanthanum Manganate (LaMnO_3) is the usual choice and has been used extensively in most test bed systems.

Solid Oxide Fuel Cell Research Goals

There are still considerable problems preventing the full introduction of SOFCs into general use. The main problem is the high cost of the electricity produced by SOFCs, especially when one allows for the system costs, and this is being addressed in several ways. A major advance would be to lower the temperature of operation. This would allow the use of cheaper materials in the fabrication of the cell. Currently cells are built from expensive alloys of Lanthanum Chromate but at a temperature of 800°C or so it would be possible to use the slightly cheaper yttria containing chromium steels and at 750°C stainless steel, which is both cheaper and has better mechanical properties,

could be used. Problems with the durability of seals would also be avoided if temperatures were lower.

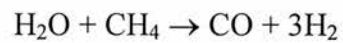
Lower temperature operation requires a higher conductivity for the electrolytes – either better materials (higher conductivity at low temperature) or new designs such as thin electrolytes from e.g. supported electrolytes. However, if the temperature is taken too low then the benefit of high quality exhaust heat and reformation of fuel is lost.

There is considerable research into new conducting ceramics and there have been some notable successes with materials such as lanthanum gallates doped with strontium and magnesium LSGM³¹ and conducting apatites.³² While many interesting compounds have been discovered, none have yet approached the maturity of the current choices, with the full issues and characteristics of the new materials, such as the loss of gallium from LSGM,³³ still being worked out.

The second big research challenge is that of fuel. While fuel cells would ideally run on hydrogen, this is currently impractical on a large scale. There is currently insufficient capacity to generate a large amount of hydrogen renewably and generating hydrogen using power from traditional sources is no real solution. Therefore the ideal solution in the near future would be to run on hydrocarbons. This would still be environmentally beneficial, as the conversion to energy and fuel utilisation would still be more efficient, reducing (rather than eliminating) greenhouse gas produced for a given amount of power generation.

There are several issues with the use of a hydrocarbon as the fuel for an SOFC. The technically easiest way is to add an external reformer to the fuel cell stack. However, this causes a considerable loss in efficiency of the whole system. The other option is internal reformation. This is technically more challenging, and there is therefore considerable interest in new materials for the fuel electrodes of SOFCs.

As an SOFC is run at such a high temperature there is enough energy to reform methane if steam is present in the fuel mix and there is a suitable catalysis site, as is shown below:



Zirconia

Zirconium is the eleventh most abundant element in the Earth's crust, more abundant than either copper or lead. Its oxide, zirconia, is an exceptionally hard refractory oxide, used to make heat-resistant crucibles, foundry bricks, ceramics and abrasives. It is so hard that it can even be used to make scissors and knives. Single crystals of zirconia are sometimes used as artificial diamonds.

Table 1.2 – Crystallographic data for the three ambient pressure polymorphs of Zirconia

Monoclinic	Tetragonal	Cubic
Space Group $P2_1/c$	Space Group $P4_2/nmc$	Space Group $Fm\bar{3}m$
$a = 5.3129 \text{ \AA}$	$a = 5.094 \text{ \AA}$	$a = 5.124 \text{ \AA}$
$b = 5.2125 \text{ \AA}$	$b = 5.177 \text{ \AA}$	
$c = 5.1471 \text{ \AA}$		
$\beta = 99.218^\circ$		

There are four polymorphs of pure zirconia, although only three are seen at ambient pressures. At room temperature it is in a seven co-ordinate monoclinic baddeleyite structure.³⁴ At 1100°C it reversibly transforms to an eight co-ordinate tetragonal structure³⁵ and it transforms to the cubic zirconia phase at above 2300°C.³⁶ The orthorhombic phase is only seen at higher pressure.³⁷ Fan *et. al.*³⁸ also reported the existence of a $Y_2Zr_2O_7$ pyrochlore phase, but this is not universally accepted.^{39,40} An

ordered $Y_4Zr_3O_{12}$ phase has also been reported.⁴¹ These are illustrated in Figure 1.4 and crystallographic detail is given in Table 1.2.

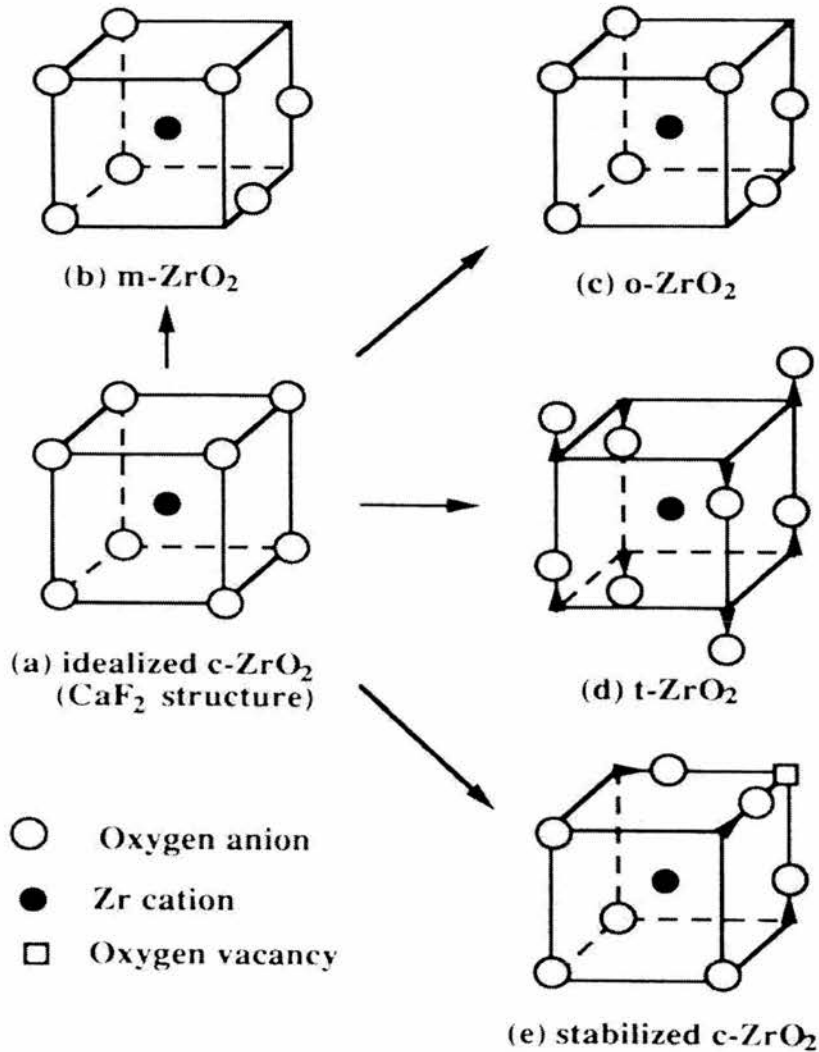


Figure 1.4 – The different polymorphs of zirconia.⁴² Orthorhombic zirconia is only seen at elevated pressures.

The peculiar structural behaviour of zirconia can in part be explained by the fact that the zirconium ion is slightly too small to fit comfortably into the eight co-ordinate cation site in the fluorite structure, but is slightly too large to fit into the six co-ordinate cation site in the rutile structure, which is the high symmetry structure that the majority

of MO_2 compounds with smaller metal ions adopt. Thus at lower temperatures it takes up the low symmetry baddeleyite structure which has a seven co-ordinate metal site and only transforms to the tetragonal phase, which has an eight co-ordinate metal site, at elevated temperatures. The fluorite phase is thus only achieved at very great temperatures.

Tetragonal zirconia can be observed at room temperature when the particle size is small, below 30 nm, as it is too small to sustain monoclinic, probably due to the large surface to volume ratio.

Stabilisation of Fluorite Zirconia

While in pure zirconia the fluorite phase only exists at above 2370°C , it is possible to stabilise the phase at room temperature by substituting other metals on to the cation lattice. Several examples of this stabilisation are discussed in the text below.

This is not a simple subject and is not entirely understood, although several theories have been put forward. The simplest is that the larger dopants, such as yttrium with an ionic radius of 1.015 \AA compared to 0.84 \AA for the zirconium ion, force the structure into the slightly larger, eight-fold co-ordinated fluorite rather than the slightly smaller seven-fold monoclinic. While this is probably partly true it does not explain the stabilisation caused by the addition of scandium, with an ionic radius which is similar to that of the zirconium ion at 0.87 \AA . As the addition of a little scandia can stabilise the cubic phase by some 1700°C ($\sim 2370^\circ\text{C}$ down to $\sim 650^\circ\text{C}$ at the $\text{Sc}_2\text{Zr}_7\text{O}_{17}$ point in the $\text{Sc}_2\text{O}_3 - \text{ZrO}_2$ Phase Diagram), the vacancies must also provide some form of

stabilisation, probably by allowing the metals to have a lower co-ordination number while retaining the fluorite structure. Thus both vacancies and size are important, but the full story is not entirely known.

Table 3 – Effective Ionic Radii of zirconia and its dopants (based on $r(\text{VI O}^{2-}) = 1.40$)^{43,44}

Co-Ordination Number	Zirconium (4+)	Yttrium (3+)	Scandium (3+)
VI	0.72	-	0.730
VII	0.78	0.892	-
VIII	0.84	1.015	0.87
IX	-	1.10	-

Yttria stabilised Zirconia (YSZ)

The best known and almost certainly the most studied form of stabilised zirconia is yttria stabilised zirconia.

The exact phase relationships are the subject of some debate, with many phase diagrams, all of which are broadly similar but subtly different, having been proposed. As a general rule, when there have been different interpretations possible, we have followed the diagram according to Scott, which is shown in Figure 1.5, as this has generally been found to be the most reliable in our previous studies. A schematic of the many different interpretations is shown in Figure 1.6.

The reason for so many different phase diagrams being proposed is the very slow reaction dynamics at relatively low temperatures (below about 800°C). Because

both yttria and zirconia are extremely high melting refractory oxides, they do not react well together at low temperature and the phases at low temperature take a long time (geological ages in some cases) to transform. Thus, 'meta-stable' or 'kinetically stable' phases are formed. These are phases which are stable, but are not in the most thermodynamically stable form, yet, due to the low temperature, they do not possess enough energy to start the transformation to the most favourable phase, the thermodynamically stable phase. The misinterpretation of some meta-stable phases as thermodynamic in some studies will lead to different phase diagrams being proposed.

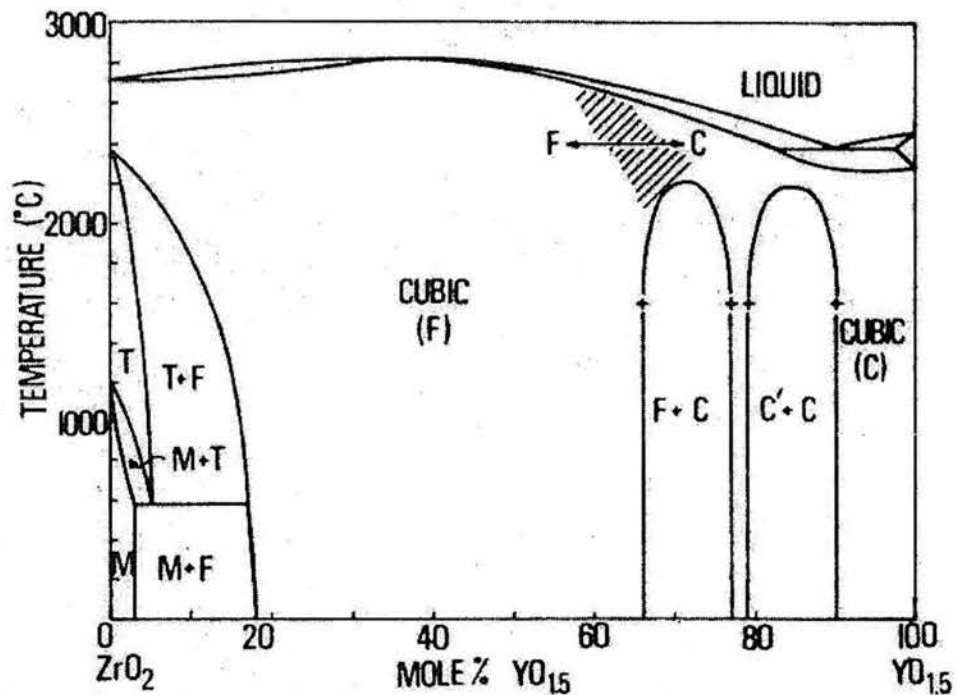


Figure 1.5 – The Phase diagram of yttria stabilised zirconia, according to Scott.⁴⁵

It is entirely possible that no completely correct diagram has yet been drawn, though, as stated previously, we have used the diagram of Scott⁴⁵ throughout this study, as it has been the most accurate in our experience.

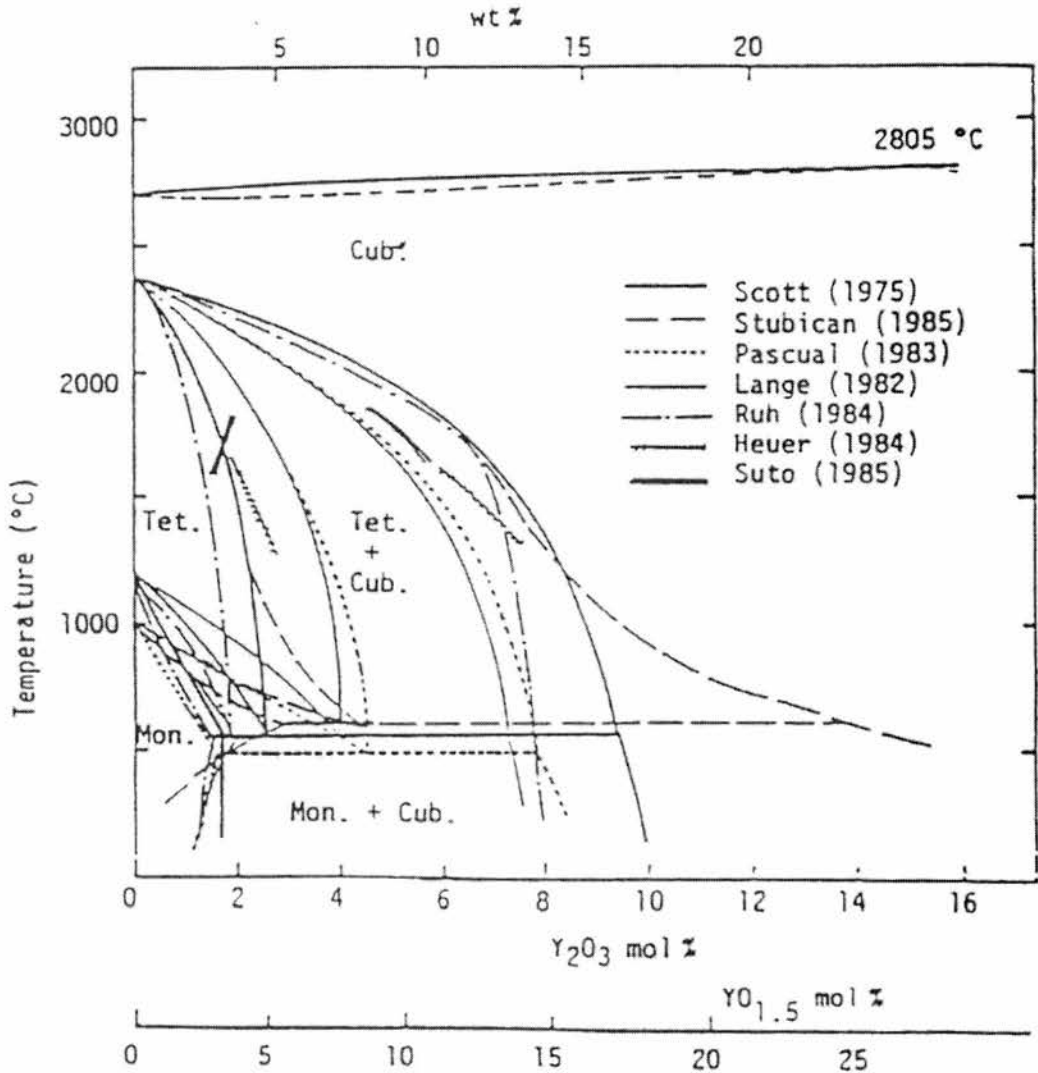
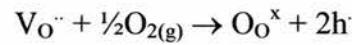


Figure 1.6 – Illustration of the differences in various yttria-zirconia phased diagrams.⁴⁶

The substitution of the aliovalent yttrium into the zirconia requires charge compensation. This is done by removing some oxygen from the lattice to leave vacancies on the oxygen site as shown in the Kröger – Vink⁴⁷ equation below. The presence of the oxygen vacancies allows for the possibility of mobility on the oxygen sub-lattice and thus oxide ion conductivity, which will be discussed further on in this introduction.



There is a possible follow-up reaction, in which the vacancies are filled with atmospheric oxygen and two holes are created to preserve electro-neutrality. However, the equilibrium point for this is far to the left, so it can be largely ignored for zirconias.



This brings us to the question of the correct structure for yttria stabilised zirconia. It is a fluorite structure with some of the anions absent and is usually described as the defect fluorite structure. The simple fluorite structure is illustrated in Figure 1.7.

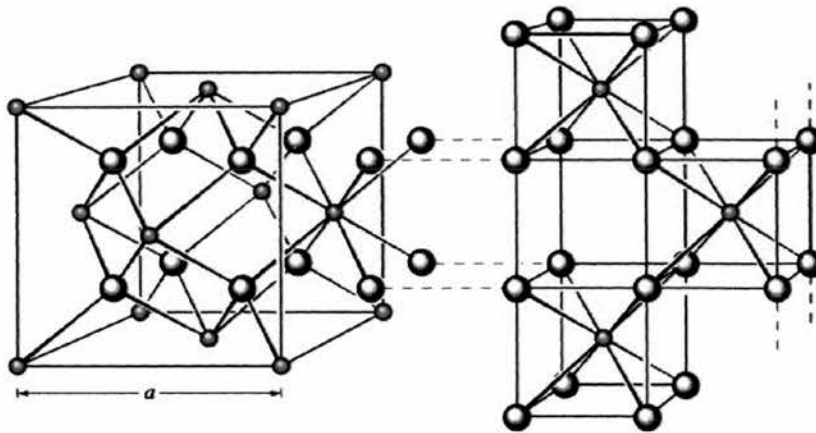


Figure 1.7- The Fluorite Structure⁴⁸

The defect fluorite structure assumes that the oxygen vacancies are evenly distributed throughout the lattice. In the case of YSZ, it has been suggested that this is not entirely correct. The falling conductivity with increasing levels of aliovalent dopant

is usually attributed to vacancy clustering,⁴⁹ causing blocking of the movement of oxide ions. Other work has also suggested the formation of microdomains of ordered oxygen vacancies within a matrix of fully co-ordinated fluorite structure.⁵⁰

Scandia stabilised Zirconia (ScSZ)

The alternate stabilisation provided by scandium has long been known as has its extremely high oxide ion conduction.⁵¹ However, only limited work has been done on the system, mainly because of the high cost and difficulty in obtaining scandium. As the price of scandium has recently fallen considerably, more work is being done on this promising system.

There is even less agreement on the exact formation of this phase system than for that of YSZ. Different phase diagrams have been proposed by several groups of workers and most bear little resemblance to each other, unlike the YSZ system where there is broad general agreement. The main issue in most of the work has been the presence of either a rhombohedral solid solution or the single compound $\text{Sc}_2\text{Zr}_7\text{O}_{17}$ at low temperature, which is exceedingly difficult to confirm. We have used the phase diagram of Spiridonov *et. al.* as our guide throughout this work.

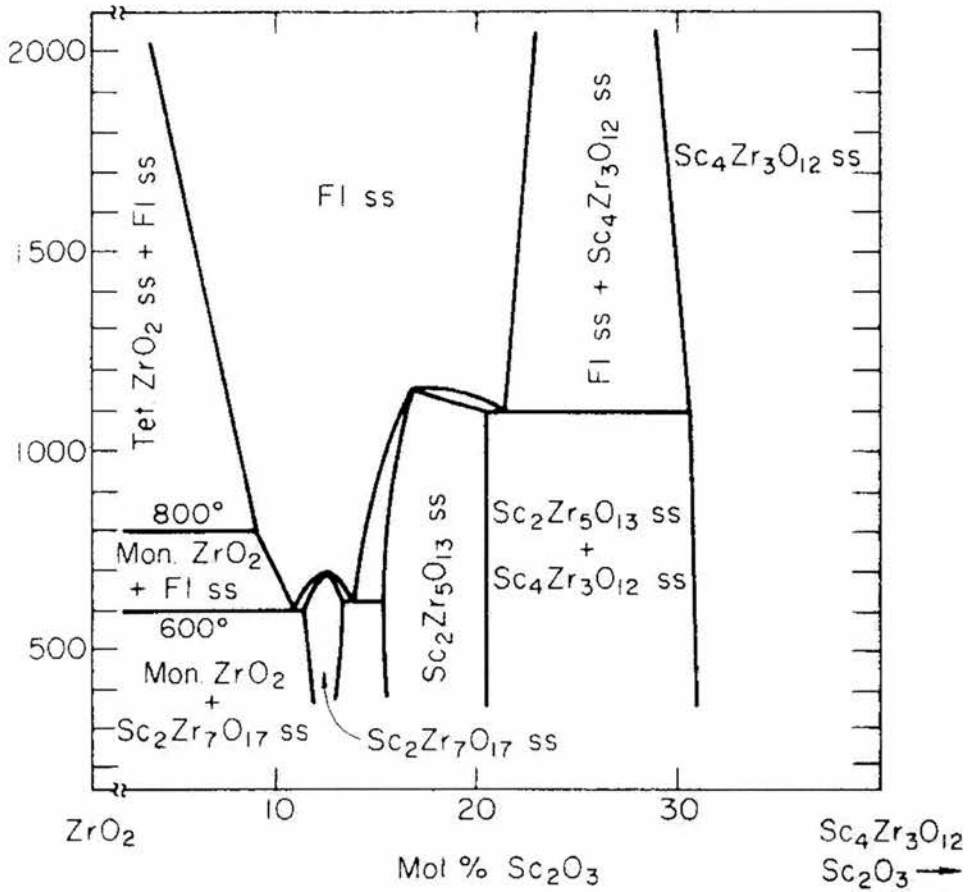


Figure 1.8 – Phase diagram of the scandia stabilised zirconia system, according to Spiridonov *et. al.*⁵²

Co-doped yttria and scandia stabilised zirconia (YScSZ)

In recent years some research into ways of combining the benefits of the stability of yttria doping with the high conductivity of scandia doping has been performed. The idea of co-doping yttria and scandia has been proved a beneficial one.^{53,54}

As in all double dopings, the conductivity of the material falls as the second dopant is added. However, as opposed to most doping regimes in yttria stabilised

zirconia the base conductivity comes from the scandia which provides a much higher conductivity than the yttria so the conductivity of the new materials is still much higher than simple YSZ. The fluorite structure is also retained at room temperature even when doped with mostly scandia and only a small amount of yttria is present. A side benefit is that the final sintered materials are extremely hard, harder than either scandia or yttria stabilised zirconia on their own. This is beneficial for the construction of strong cells, but has occasionally hindered the characterisation of these materials.

Given the extensive work already performed on SOFC test systems based on zirconia electrolytes, the raised conductivity of this material compared to YSZ, its retention of fluorite structure and better phase stability than ScSZ combined with its excellent mechanical properties make this an excellent choice for next generation SOFC test systems and possibly for full commercialisation.

Other Stabilised Zirconias

Several other metals have been used to stabilise the fluorite phase in zirconia, most notably calcium in calcia stabilised zirconia,⁵⁵ which has been considered as an SOFC electrolyte material.⁵⁶ Other metals that can be used to stabilise zirconia include ruthenium, ytterbium,⁵⁷ magnesium and many more.

While zirconia is an old and well studied system, it is continually surprising. New forms, such as nano-crystalline YSZ or mesoporous YSZ,⁵⁸ and new uses are still being discovered after a hundred years of work.

References

- 1 R. Barlow, *Home Power*, 1999, **72**, 19.
- 2 U. Bosell, *The Birth of the Fuel Cell*, European Fuel Cell Forum, Oberrohrdorf, 2000.
- 3 C. F. Schönbein, *Philos. Mag. (III)*, 1839, **14**, 43.
- 4 W. R. Grove, *Phil. Transactions (I)*, 1845, 351.
- 5 W. R. Grove, *Philos. Mag. (III)*, 1842, **21**, 417.
- 6 W. R. Grove, *Phil. Transactions (I)*, 1843, 91.
- 7 M. Krumpelt, R. Kumar and K. Myles, *J. Power Sources*, 1994, **49**, 37.
- 8 *Economist*, 1997, Oct 25, 143.
- 9 *The Independent* 2001, Jun 8,
(also at <http://www.independent.co.uk/story.jsp?story=76855>)
- 10 S. R. Ovshinsky, *Nature*, 2000, **406**, 457
- 11 *Chemistry and Industry*,
- 12 P. W. Atkins, *Physical Chemistry, 3rd Ed.*, Oxford Press, Oxford, 1990.
- 13 E. N. Balko and W. Avery, *Int. J. Hydrogen Energy*, 1981, **6**, 255.
- 14 C. Haynes, *J. Power Sources*, 2001, **92**, 199.
- 15 S. C. Singhal, *Solid State Ionics*, 2000, **135**, 305.
- 16 Harvard School of Public Health estimates.
- 17 Accessed through the Web of Science at wos.mimas.ac.uk
- 18 A. Melis, L. Zhang, M. Forestier, M. L. Ghirardi and M. Seibert, *Plant Physiol.*, 2000, **122**, 127.
- 19 A. Bain and W. D. VanVost, *Int. J. Hydrogen Energy.*, 1999, **24**, 399.
- 20 J. Larminie and A. Dicks, *Fuel Cell Systems Explained*, Wiley, Chichester, 2000.

-
- 21 J. H. Reid, US patent No 736 016 017, 1902.
- 22 M. Warshay and P. R. Prokopius, *J. Power Sources*, 1990, **29**, 193.
- 23 <http://www.power-technology.com/contractors/fuel/zetek/> and D. Magada, Reuters News Service, 17 September 2001.
- 24 http://www.zetekpower.com/News_Events/admin_announce.htm
- 25 M. Warshay, P. R. Prokopius, M. Le and G. Voecks, *Proc. Intersoc. Energy Convers. Eng. Conf.*, 1996, **1**, 1717.
- 26 T. Koppel, *Powering the Future – the Ballard fuel cell and the race to change the world*, Wiley, Chichester, 1999.
- 27 W. Nernst, *Z. Elektrochem*, 1899, **6**, 41.
- 28 W. Schottky, *Wiss. Veröff. Siemens Werken*, 1935, **14**, 1.
- 29 E. Baur and H. Preis, *Z. Elektrochem*, 1937, **43**, 727.
- 30 K. D. Kreuer, *Solid State Ionics*, 1997, **97**, 1.
- 31 T. Ishihara, H. Matsuda and Y. Takita, *J. Am. Chem. Soc.*, 1994, **116**, 3801.
- 32 S. Nakayama, H. Aono and Y. Sadoka, *Chem. Lett.*, 1995, **6**, 431.
- 33 K. Yamaji, H. Negishi, T. Horita, N. Sakai and H. Yokokawa, *Solid State Ionics*, 2000, **135**, 389.
- 34 J. D. McCullough and A. M. Heuer, *Acta Crystallogr.*, 1959, **12**, 507.
- 35 G. Teufer, *Acta Crystallogr.*, 1962, **15**, 1187
- 36 D. K. Smith and C. F. Cline, *J. Am. Ceram. Soc.*, 1962, **45**, 249.
- 37 S. Kume, O. Ohtaka, T. Yamanaka and T. Navrotsky, *Solid State Ionics*, 1989, **32**, 285.

- 38 Fu'Kang Fan, A. K. Kuznetsov and E. K. Keller, *Izv. Akad. Nauk. SSSR Otd. Khim. Nauk.*, 1962, 1141. (Reference from Ref. 45)
- 39 M. Dulcot, J. Vicat and C. Deportes, *J. Solid State Chem.*, 1970, **2**, 236.
- 40 W. W. Barker, *Izv. Akad. Nauk. SSSR Neorg. Mater.*, 1972, **8**, 2051.
- 41 S. P. Ray and V. S. Stubicon, *Mater. Res. Bull.*, 1977, **12**, 549.
- 42 P. Li, I-W. Chen and J. E. Penner-Hahn, *Phys. Rev. B*, 1993, **48**, 10063.
- 43 R. D. Shannon and C. T. Prewitt, *Acta Crystallogr., Sect. B*, 1969, **25**, 925.
- 44 R. D. Shannon, *Acta Crystallogr., Sect. A*, 1976, **32**, 751.
- 45 H. G. Scott, *J. Mater. Sci.*, 1975, **10**, 1527.
- 46 M. Yoshimura, *Ceram. Bull.*, 1988, **67**, 1950.
- 47 F. A. Kröger and H. J. Vink, *Solid State Physics, Vol. 3*, F. Seitz and D. Turnbull (eds.), Academic Press Inc, New York, 1956.
- 48 L. Smart and E. Moore, *Solid State Chemistry: An Introduction*, Stanley Thornes, Cheltenham, 1998.
- 49 C. B. Choudhary, H. S. Maiti and E. C. Subbarao, in *Solid Electrolytes and Their Applications*, ed. E. C. Subbarao, Plenum Press, New York, 1980, p. 1.
- 50 S. García-Martín, M. A. Alario-Franco, D. P. Fagg, A. J. Feighery and J.T.S. Irvine, *Chem. Mater.*, 2000, **12**, 1729.
- 51 T. H. Etsell and S. N. Flengas, *Chem. Rev.*, 1970, **70**, 339.
- 52 F. M. Spiridonov, L. N. Popova and R Ya. Popil'skii, *J. Solid State Chem.*, 1970, **2**, 432.
- 53 F. T. Ciacchi, S. P. S. Badwal and J. Drennan, *J. Eur. Ceram. Soc.*, 1991, **7**, 185.
- 54 F. T. Ciacchi and S. P. S. Badwal, *J. Eur. Ceram. Soc.*, 1991, **7**, 206.

55 R. Stevens, *An Introduction to Zirconia*, Magnesium Elektron, London, 1986.

56 H. Iwahara, *Solid State Ionic*, 1995, **77**, 289.

57 O. Yamamoto, Y. Arati, Y. Takeda, N. Imanishi, Y. Mizuntani, M. Kawai and Y. Nakamura, *Solid State Ionic*, 1995, **79**, 137.

58 M. Mamak, N. Coombs and G. Ozin, *Adv. Mater. (Weinheim, Ger.)*, 200, **12**, 198.

Experimental and Theory

SAMPLE PREPARATION	49
SOLID STATE METHODS	50
SOLUTION METHODS	51
DIFFRACTION METHODS OF SAMPLE CHARACTERISATION	54
DIFFRACTION	54
Bragg's Law	55
Lattice Planes and Miller Indices	59
Systematic Absences	61
Form Factors and the Intensity of Peaks	62
GENERATION OF X - RAYS	63
NEUTRON DIFFRACTION	66
RIETVELD (PROFILE) REFINEMENT	68
EXTENDED X-RAY ABSORPTION FINE STRUCTURE (EXAFS)	70
BASIC CONCEPTS	70
EXAFS INSTRUMENTS	72
EXAFS THEORY	74
Derivation of the EXAFS Equation	76
THE EXAFS EXPERIMENT	78

Normalisation and summing of spectra	78
Background subtraction	78
Errors in EXAFS	80
EXPERIMENTAL METHOD	80
Preparation of samples for EXAFS	80
DATA HANDLING	81
NUCLEAR MAGNETIC RESONANCE SPECTROSCOPY (NMR)	82
A. C. IMPEDANCE SPECTROSCOPY	85
EXPERIMENTAL METHOD	88
REFERENCES	89

Solid state chemistry is now a subject of considerable maturity and, as such, is already the subject of a number of good textbooks that cover the topic in greater detail than is possible in a single chapter.^{1,2,3,4,5} This chapter deals only with the essentials of the topic and is heavily indebted to the textbooks used in the study.

Sample Preparation

The preparation of refractory oxides demands care and control of the process. Due to the high melting points of the reactants, all reactions tend to take place entirely in the solid phase. This requires intimate mixing of the reacting components, as, with very little movement of atoms possible, reactions can only take place through the diffusion of atoms between closely neighbouring grains. As there are almost no means of purification, reactions have to have a 100% yield, as no impurity can be separated.

Two main methods have been used for the preparation of materials; solid state synthesis and solution methods.— Where necessary, non-standard preparation methods or problems with specific preparations will be detailed in the relevant chapters.

Solid State Methods

Samples were prepared from stoichiometric amounts of yttria (Y_2O_3), zirconia (ZrO_2), scandia (Sc_2O_3) and boric acid (H_3BO_3). The ceramic reactants were first dried at elevated temperatures (700-900°C) to remove adsorbed water and carbon dioxide.

The components were then ground together for twenty to thirty minutes in an agate pestle and mortar to ensure intimate mixing. Grinding was performed under acetone to prevent the formation of airborne dust. Alternatively, some samples were prepared with the components being milled in a mechanical ball mill. This is often superior to hand grinding as it is generally more repeatable and produces finer and better-mixed samples.

The samples were then pressed into pellets in a uni-axial pellet press. The pellets were weighed, placed into alumina or platinum crucibles and placed into the furnace at 1000°C. They were then fired at between 1200°C and 1500°C for 24-72 hours, before the temperature was lowered to 1000°C and the samples removed.

Samples were then ground in the agate pestle and mortar for routine phase analysis. If necessary, the pellets were broken in a steel percussion mortar before being ground. If, after the phase analysis had been performed, the sample had been shown not to be fully reacted it was re-pelletised and re-fired to complete the reaction.

Solution Methods

Solution methods can sometimes be more suitable than the standard solid state methods as they allow for the atomic level mixing of the reactants. They usually produce very fine powders, which gives the reactants a much higher surface area and therefore makes them more reactive. The disadvantage is that, in general, solution methods take longer to perform than the standard solid-state methods.

The two main solution methods⁶ of sample preparation are co-precipitation and sol-gel or gel methods. Co-precipitation is the mixture of stoichiometric amounts of soluble metal salts in a solvent. As they are dissolved they become intimately mixed in the solution. The evaporation of the solvent thus leaves a powder that is far better mixed than is possible through hand grinding. This method is only useful when all the reactants are of similar solubility; otherwise they will be deposited sequentially and not be fully mixed.

Gel methods avoid many of the problems of co-precipitation, while retaining the advantage of producing extremely fine powders. The addition of an organic gelling agent binds the dissolved reactants in place while the solvent evaporates. This leaves the reactants in the same intimate mixture as was formed in the solution phase. The gel can then be crushed and burned off at a suitable temperature, leaving a fine mix of reactant powders.

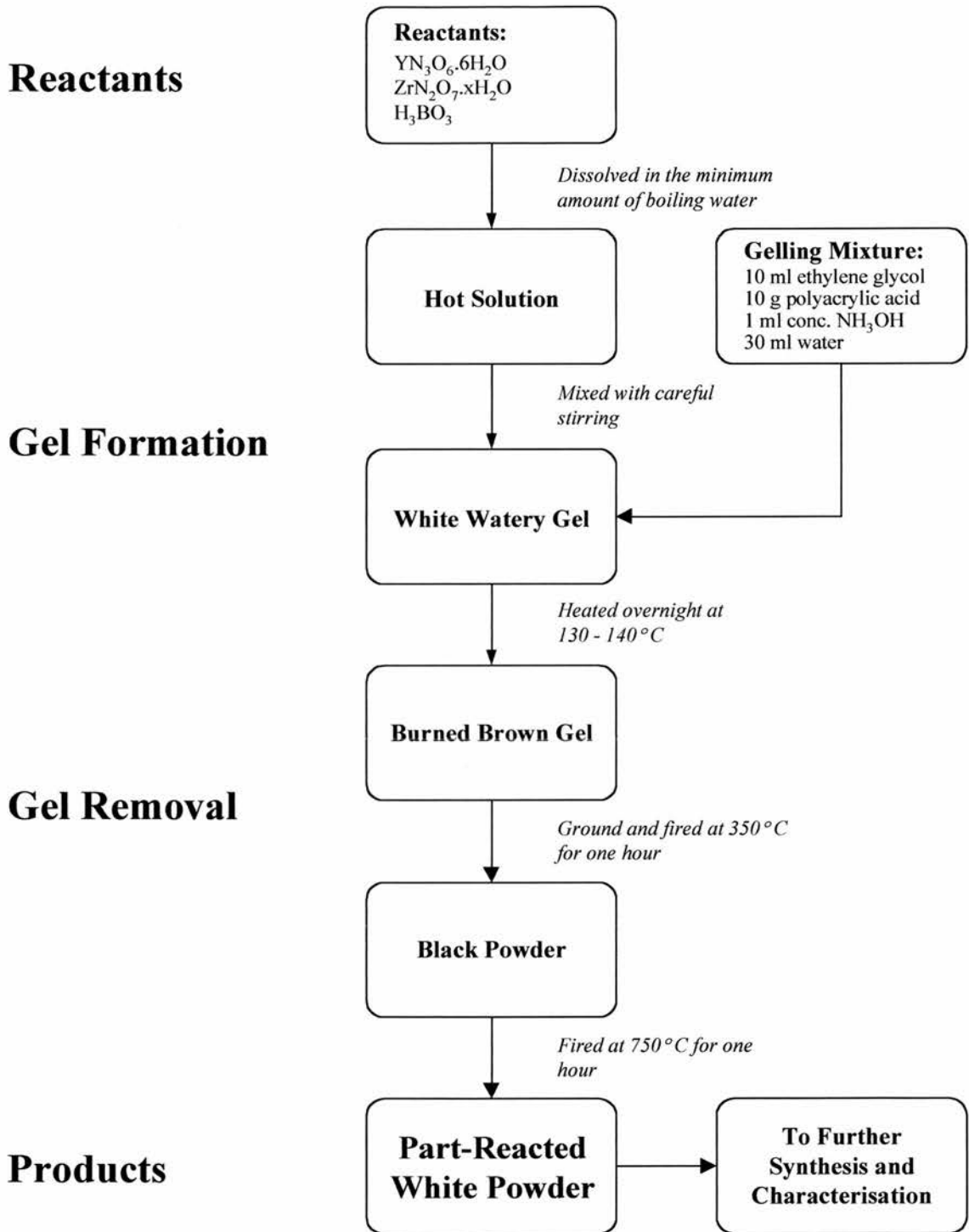


Figure 2.1 – Simple Gel method for the production of approximately five grams of ceramic.

The solution method used in this work was a gel method, which is illustrated in Figure 2.1. This method is based on that used by Brian Mitchell for preparation of lead based superconductors. ⁷

After the intimately mixed powders have been produced via the gel method they are treated in much the same way as those from traditional 'shake and bake' preparations, with one important caveat – they do not need anywhere near the same temperatures for reaction. As an example, complete reaction to YSZ was observed regularly at 1000°C, when much higher temperature is normally required for solid state synthesis.

Diffraction Methods of Sample Characterisation

The main technique used was X-ray diffraction, which is the workhorse characterisation technique for the solid-state chemist. It is generally the first technique used on any sample for routine phase analysis and has been used since early in the 20th century to determine crystal structures and help fingerprint materials.⁸

The other main diffraction method used was neutron diffraction. This excellent technique is useful as it generally produces more information from a given sample than X-ray diffraction. Unfortunately it is far more expensive and cannot, therefore, be used routinely.

Throughout this discussion of diffraction, x-rays are assumed. Neutrons however, through their wave-particle duality, can be treated in a similar manner. The differences will be discussed in a later section.

Diffraction

The diffraction of x-rays by a crystal is similar to the diffraction of light by an optical grating. When a wave train approaches a grating it is considered to be entirely coherent. As it reaches the grating, the wave passes through all the slits simultaneously. Upon passing through the grating each slit acts as a secondary point source for new waves of the same wavelength. This is shown in Figure 2.2. Each wave is still coherent with the other waves, but the waves may now interfere with each other. This

interference is dependent upon the relative wavelength of each wave at a certain point. If the waves are in phase, then there is constructive interference and an amplification of the signal, if they are exactly out of phase the waves are cancelled out due to destructive interference between the waves. This leads to a diffraction pattern being produced on any surface behind the grating.

In the case of an x-ray diffraction experiment, the atoms act as a diffraction grating. The interference pattern produced from this diffraction can be interpreted to give information on the internal structure of the material.

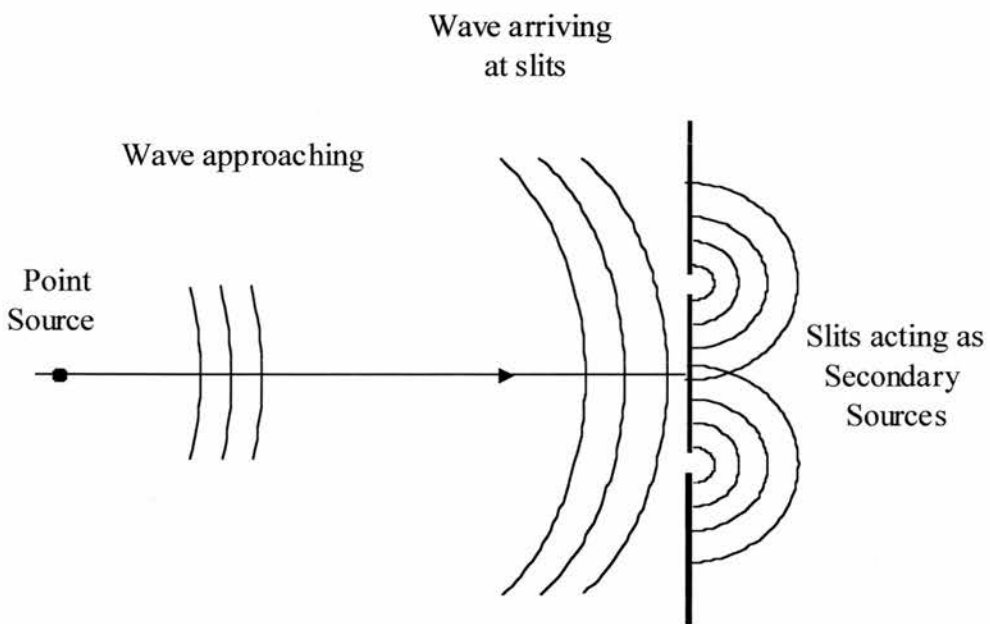


Figure 2.2 – The effect of a diffraction grating on a wave train.

Bragg's Law

The idea that a crystal could act as a diffraction grating to radiation of the right wavelength was first suggested and formulated by Laue⁹ in 1912, but the mathematics

of his approach are not trivial. The full treatment suggested by Laue is fortunately not usually necessary as, a year after Laue's work, Bragg¹⁰ proposed a model that is applicable in almost all cases.

The Bragg model of diffraction is to regard the sample as a series of semi-transparent mirrors. Some x-ray beams will be reflected by the first plane, some go through and will be reflected by the next and so on. A crystal can be modelled as an infinite stack of these layers.

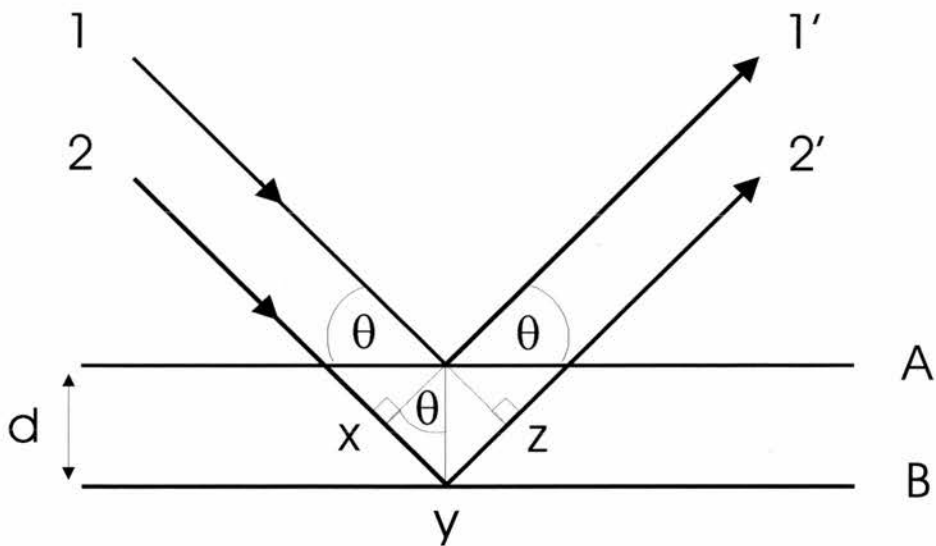


Figure 2.3 – Bragg reflection.

As is shown in Figure 2.3, two x-ray beams come into a crystal and each is reflected from different, but adjacent, planes. As shown in the diagram, the second beam (2') has travelled further than the first beam (1'). Depending on the angle, and the resulting path length difference ($x \rightarrow y \rightarrow z$), it may no longer be in phase with the first beam. If the extra distance it has travelled is an integral number of wavelengths then it

will still be in phase and the two beams will constructively interfere, giving rise to a peak in the diffraction pattern. If, however, the path length difference is not an exact number the two beams will destructively interfere, resulting in no intensity and no peak in the pattern. Thus, peaks are only seen at set 'Bragg' angles, leading to the derivation of Bragg's Law.

The distance between the planes, d , can be related to the Bragg angle, θ ;

$$xy = yz = d\sin\theta$$

Thus: $xyz = 2d\sin\theta$

To get constructive interference, we need a path length equivalent to a whole number of wavelengths:

$$xyz = n\lambda$$

Which leads to Bragg's Law:

$$2d\sin\theta = n\lambda$$

It is important to realise that the law calls for an infinite number of layers. For complete destructive interference, the beams must be in anti-phase, or exactly π out of phase with each other. For beams that are only a small angle away from a Bragg angle, the entirely anti phase reflection will be many thousand layers inside the crystal.

A consequence of this requirement for infinite layers is the broadening of peaks in very small particles. As there are not a large enough number of layers for the incident beam's wavelength to become exactly π out of phase with the radiation reflected from the first layer of the crystal, there is not complete destructive interference between the waves. This causes a broadening of the peaks proportional to the size of the particles. The size of the particles can be calculated using the Scherrer equation, given below;

$$T = \frac{0.9\lambda}{B\cos\theta}$$

Where T = The thickness of the crystal in angstroms.

λ = The x-ray wavelength.

θ_B = The Bragg angle

B = The extra width of the x-ray peak at half height when compared with a standard of the same material. Calculated from:

$$B^2 = B_M^2 - B_S^2$$

Where B_M is the full width half maximum (FWHM) of the sample and B_S is the FWHM of the reference sample.

As a rule of thumb, the broadening of the peaks of a crystallite of over 2000 layers (or roughly 2000 Å) is not noticeable against the general broadening of the peaks caused by other effects, such as the intrinsic breadth of the $K\alpha$ line (from the Heisenberg uncertainty principle) or slight imperfections in monochromation or the geometry of the instrument.

Lattice Planes and Miller Indices

The imaginary mirrors from the Bragg model can be related to atomic level structure by various planes of atoms or lattice points, as shown in the two dimensional lattice depicted in Figure 2.4.

Each set of these planes shows a different inter-planar spacing and thus will meet the conditions of the Bragg Law at a different incident angle. Each plane may lead to a reflection and thus a peak in the resulting diffraction pattern.

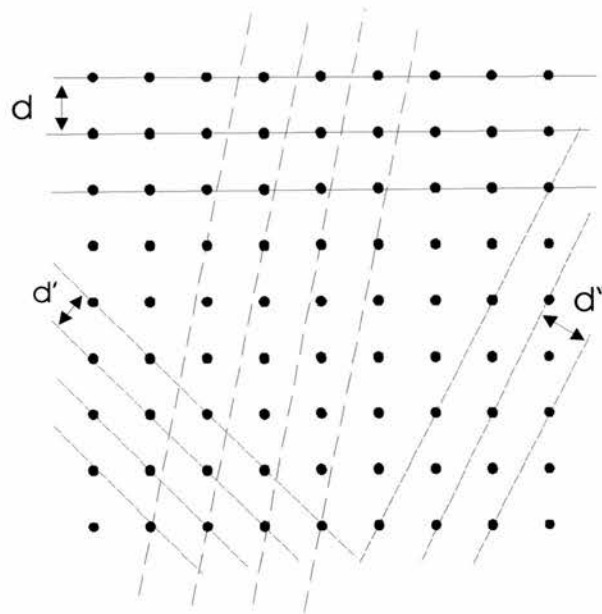


Figure 2.4 – Some possible lattice planes.

Three numbers, known as Miller indices, may be used to describe lattice planes. These three numbers are defined by where a plane cuts through the unit cell of the given structure. The unit cell is, of course, the simplest repeatable unit in the atomic lattice.

Looking at Figure 2.5, the planes drawn cut the axis of the unit cell at:

$$a = \frac{1}{2}$$

$$b = 1$$

$$c = \frac{1}{3}$$

The Miller index for this plane is the reciprocal of these numbers, therefore this plane is the 2 1 3 plane, usually written as (213). The peak resulting from a reflection from this plane will be labelled as the 2 1 3 peak.

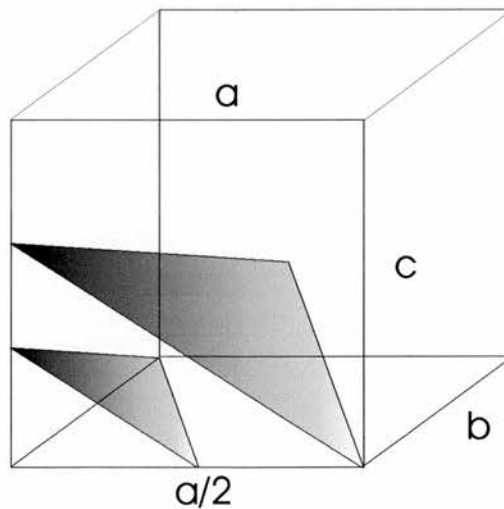


Figure 2.5 – Two adjacent lattice planes.

The Miller Indices of a given peak are thus related to lattice parameters. For example, in an orthorhombic system (where all the unit cell angles are 90°) they can be related to the unit cell edges (a , b and c) and the inter-planar distance (d) as follows:

$$\frac{1}{d_{hkl}^2} = \frac{h^2}{a^2} + \frac{k^2}{b^2} + \frac{l^2}{c^2}$$

Systematic Absences

What has been shown so far would indicate that every lattice plane would cause a reflection and thus a peak. This is not entirely true. While every plane can cause a reflection, some will have an intensity of zero, as they are cancelled out by destructive interference caused by reflections from other planes. This is known as a systematic absence. In Figure 2.6 there is a body centred cubic unit cell. A reflection from the (100) plane could be expected to be seen, but it is absent because the plane between, the (200), also reflects. As the (200) is half way between the (100) planes, the reflection it causes is exactly π out of phase with that of the (100) plane, cancelling it out through destructive interference. Thus there is only a reflection from the (200).

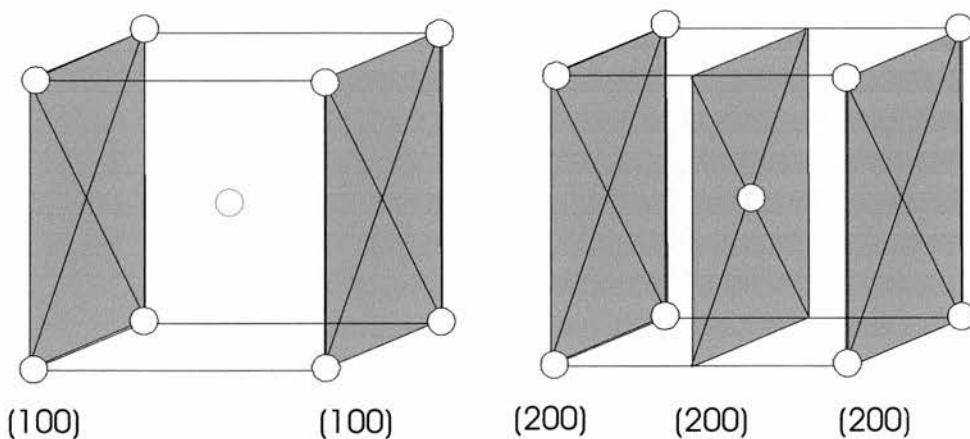


Figure 2.6 – Lattice planes in a bcc structure, with the 100 reflection at twice the length of the 200 reflection.

Absences can also occur due to other symmetry elements such as glide planes and screw axes.

Form Factors and the Intensity of Peaks

X-rays are scattered from the electron clouds around atoms, known as Thompson scattering. As more electrons mean more scattering, large, heavy elements dominate the patterns and small light elements can be almost undetectable.

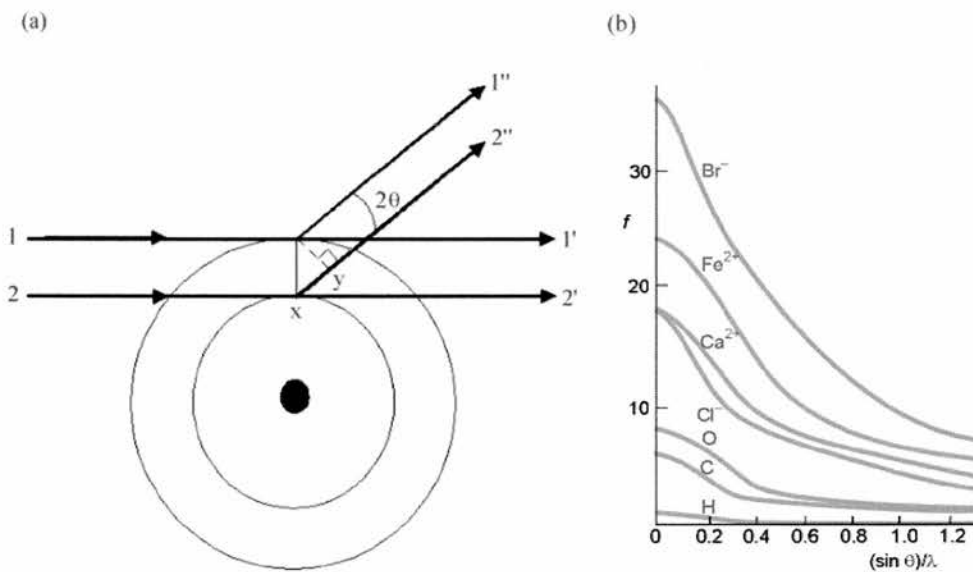


Figure 2.7 - (a) Destructive interference between x-ray beams scattered from different parts of an electron shell. (b) Some typical values of x-ray form factors ¹¹

There is also a relationship between 2θ and the intensity of peaks in an x-ray pattern. Because the atom is not a simple point source it is possible for photons

scattered from different parts of the atom. This affect increases with increasing 2θ as is shown in Figure 2.7 (a).

Other factors may also affect the intensity of peaks :

- Crystals with either needle or plate shaped unit cells will not stack randomly. Thus certain planes will receive a higher flux of x rays than others which will affect the intensity of the resulting peaks. This is called Preferred orientation.
- In high symmetry systems many planes will have the same d spacing. Thus, in a cubic powder sample where the small crystals are arranged randomly, planes such as the (013) and the (130) give a single reflection, having the same d spacing in a cubic system. This would cause their intensities to be summed in the powder spectrum.
- Thermal motion of the atoms can also cause their reflections to decrease in size. It is possible to measure these with high resolution techniques such as neutron diffraction.

Generation of X - Rays

There are two ways generally used for the production of x-rays for diffraction. These are by the bombardment of a metal source or from a synchrotron.

In modern laboratory equipment x-rays are generated by accelerating an electron beam through $\sim 30\text{kV}$ and firing it at a metal target, usually copper. The incident electrons will have high enough energy to eject electrons from the 1s shell. When an electron from a higher shell (2p or 3p) falls to fill this gap, the energy released by the transition is emitted as an x-ray photon. The two possible transitions lead to two different energies for the x-ray. They are K_α for the 2p \rightarrow 1s transition and K_β for the 3p \rightarrow 1s transition. Due to the two possible spin states in the 1s shell that the electron can drop into, the K_α is in fact a doublet. This is denoted by $K_{\alpha 1}$ ($\lambda = 1.5405 \text{ \AA}$) and $K_{\alpha 2}$ ($\lambda = 1.5443 \text{ \AA}$).

Experiments are performed using monochromatic beams of x-rays. As the K_α line has the higher intensity it is preferred for diffraction studies. It is possible to remove the K_β line easily by passing it through a thin sheet of nickel. This absorbs the K_β radiation and much of the background ('white' or Bremsstrahlung) radiation as well, leaving the K_α line.

Most modern diffractometers use single crystal monochromators to remove the unwanted radiation. This method uses a large single crystal, which is oriented so that the desired radiation will reflect from one of its crystal planes. As x-rays are naturally diverging, the crystal is usually slightly bent so that it focuses the diverging beams into a more intense single beam.

The second method of generating x rays, or indeed any electromagnetic radiation, is from a synchrotron. A synchrotron is a large ring in which electrons

circulate. Electrons are produced from a heated cathode in the electron gun and are pulled out into a stream by a powerful electric field. They are then accelerated and chopped into bunches or pulses by high-energy microwaves and radio waves in the linear accelerator (LINAC). These also speed up the electrons to close to the speed of light. The stream then passes into the booster ring where the energy of the electrons is boosted to working levels (anywhere between 1 and 7 GeV, depending on the synchrotron) by radio waves. From here the beam passes into the storage ring.

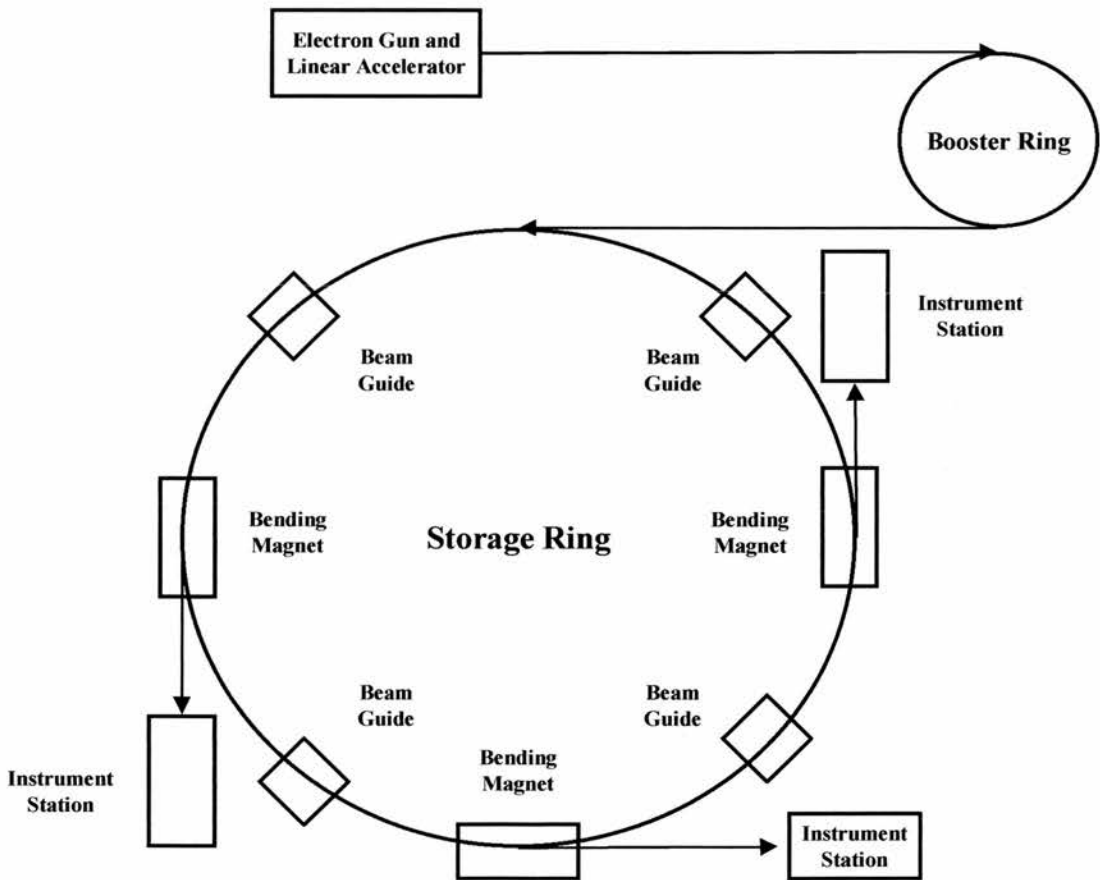


Figure 2.8 – Block guide to a synchrotron

If electrons change angular momentum they emit electromagnetic radiation. In large rings this can be of great intensity. Synchrotrons produce white radiation, but it is now a fairly routine procedure to mono-chromatize it. This can then be used for a wide range of advanced experiments. Another advantage of synchrotrons is that the electrons are synchronous, which has advantages in experiment design and indeed leads to the name 'synchrotron'.

Although usually described as rings, this is a misleading term. Synchrotrons are in fact polygons, with the electro - magnetic radiation extracted at the corners, where the electrons change direction. Originally this change was effected by means of a bending magnetic, but in a modern ("3G") synchrotron it is done through more tuneable "insertion devices" such as wigglers and undulators, which give different energy profiles and beam patterns than simple bending magnets. The extracted radiation is then tuned and focused for use on the various experimental stations.

Neutron Diffraction

As mentioned earlier in the text, it is also possible to use neutrons as a probe for the structure of matter. As neutrons have a wavelength of approximately one angstrom they can also be diffracted by atomic lattices in a similar way to x-rays. Neutron diffraction obeys Bragg's law and behaves in a similar way to x-ray diffraction, with a few important differences.

Firstly, neutrons are scattered by complex interactions with the atomic nuclei rather than by the electron clouds as x-rays are. As the interaction is not dependent on

the mass of the nuclei, this means that neutrons are sensitive to very small atoms in lattices of larger ones. This type of interaction also means that the intensity from neutron sources does not fall off with increased angle, giving more information at high values of 2θ (which relates to small d spacing planes). The relationship between atomic number and scattering is shown in Figure 2.9.

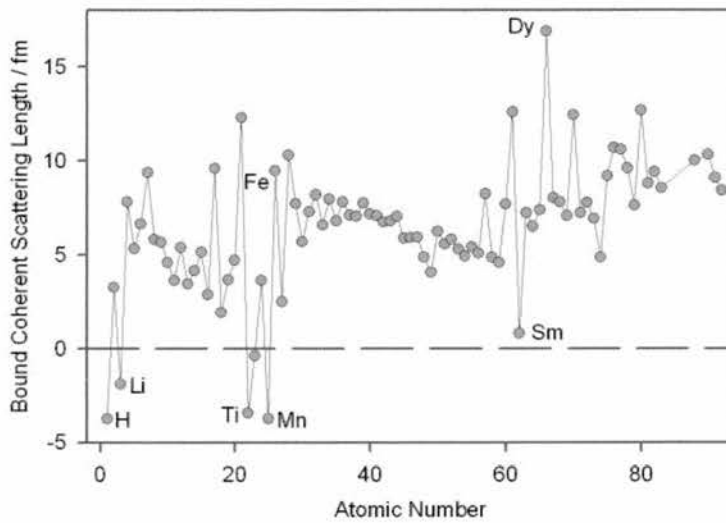


Figure 2.9 – Neutron scattering lengths plotted against atomic number ¹²

Additionally, as neutrons have a magnetic moment they will interact with a magnetic sample and give information on the magnetic structure of the sample. This is obviously beneficial, but can lead to very complex diffraction patterns.

There are two main sources of neutrons for research purposes – reactor and spallation sources. Each has its own benefits, with reactors providing a very high flux of neutrons and spallation sources providing well focused neutrons possessing an inherent time pulse which is useful in some experiments.

In this study, most of the experiments were performed at Studsvik in Sweden on the NPD (Neutron Powder Diffraction) instrument. Limited experiments were performed at the Rutherford Appleton Laboratories (RAL) on the instruments HRPD and POLARIS.

Rietveld (Profile) Refinement

It was realised early on that there was more information in a powder diffraction pattern than simply the position and height of the peaks. Powder patterns still contained most of the information present in single crystal patterns, but it was not possible to see many peaks overlapped each other. With the advent of computers it became possible to use their power to analyse the patterns using statistical methods to attempt to obtain more information from them. The most commonly used method is the Rietveld method.^{13,14,15}

The Rietveld method is a whole spectrum approach and models both the peaks and the noise in between. The experimentally determined pattern is assumed to be the sum of a number of Gaussian shaped Bragg reflections. The computer fits a pattern generated from a model compound to the entire diffraction pattern and then adjustments are made to the model to tune the calculated pattern to the experimental one. It is important to note that this is an entirely statistical method and no account is taken of crystallography or peaks. Thus a good model and great care are needed to ensure the final answer is sensible or even possible.

As the method is based on peak shape analysis, good peak shapes are needed, thus neutron spectra are often preferred as the peak shapes tend to be more Gaussian. In this study, profile refinements were performed using the program FULLProf,¹⁶ on samples obtained from neutron sources.

Extended X-ray Absorption Fine Structure (EXAFS)

EXAFS is an excellent technique for investigating the local environment of materials. It is a useful complement to broad structural characterisation techniques such as neutron and x-ray diffraction, as it focuses on the short range structure of a material rather than the long range, allowing a different, but complimentary, picture of a material to emerge. Another advantage to EXAFS is that it is atom specific, allowing it to differentiate similar atoms, such as yttrium and zirconium, that other, broad band, techniques cannot distinguish. The technique has been widely used for many years and it is beginning to approach the same level of maturity as better-known techniques such as Rietveld refinement of powder diffraction data.

EXAFS phenomenon were probably observed with the earliest experiments with x-ray radiation and were first reported in the 1920's,¹⁷ but the first attempts to explain the phenomenon were by R. de L. Kronig^{18,19} in 1931. After much debate, the first widely accepted theories were put forward by Stern, Sayers and Lytle in the 1970s.^{20,21,22,23}

Basic Concepts

If an x-ray is fired into an atom above a characteristic energy then it will eject a core electron. An electron further out in the atom's electron shell will then fall into the vacated lower energy state, emitting a photon of energy. This is simply ionisation and

the specific ejection events cause the k or l x-ray absorption edges, depending on the electron initially ejected.

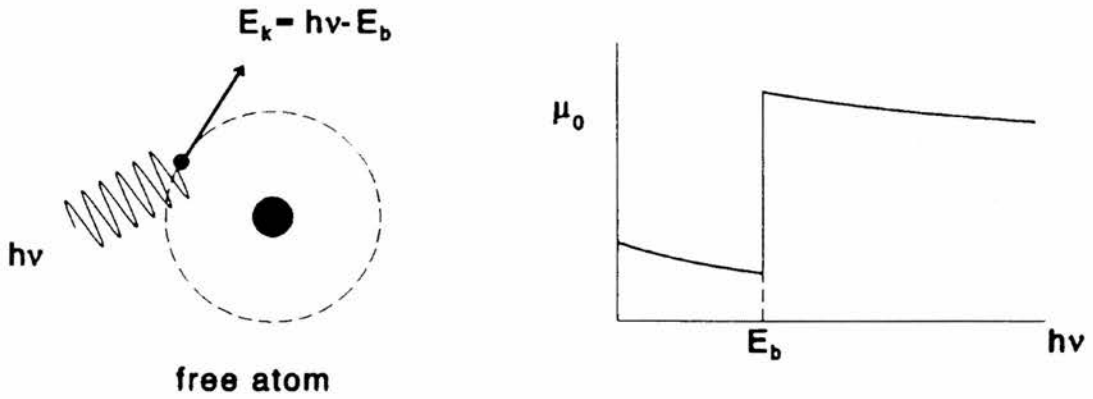


Figure 2.10 – An isolated electron ejection and the corresponding x-ray absorption edge.²⁴

In an isolated atom, such as a noble gas, this is the complete explanation. However, in condensed matter and compounds the atoms surrounding our central atom interfere with the emitted electron, as shown in Figure 2.11, producing modulations in the absorption energy structure.

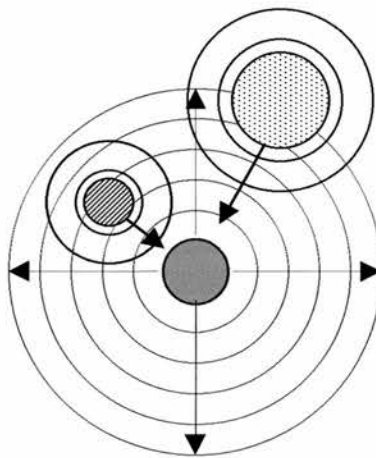


Figure 2.11 – Reflection from the surrounding atoms.

Thus, this modulation is related to the positions and sizes of the surrounding atoms and it is possible to analyse the post edge structure to obtain some of this information. This is the EXAFS effect.

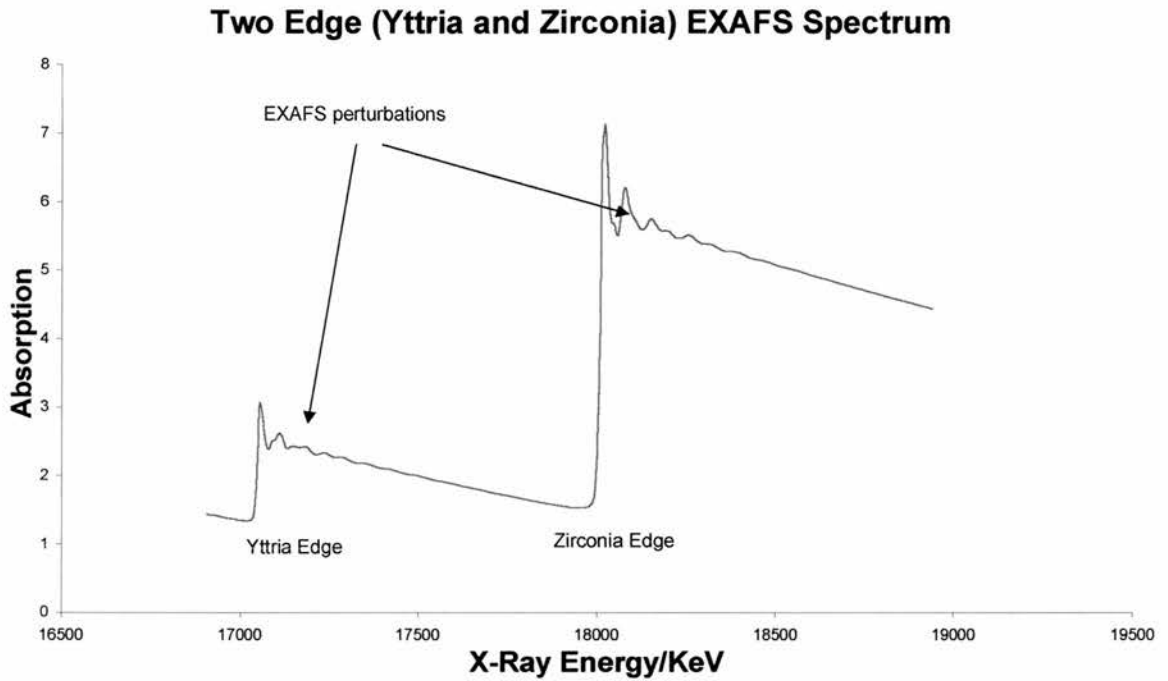


Figure 2.12 – Two edge EXAFS spectrum.

EXAFS Instruments

EXAFS requires a powerful x-ray source which is also tuneable to a particular energy requirement, with the useful energies being in the range 3-30 keV, meaning the majority of EXAFS experiments are done using synchrotron radiation.

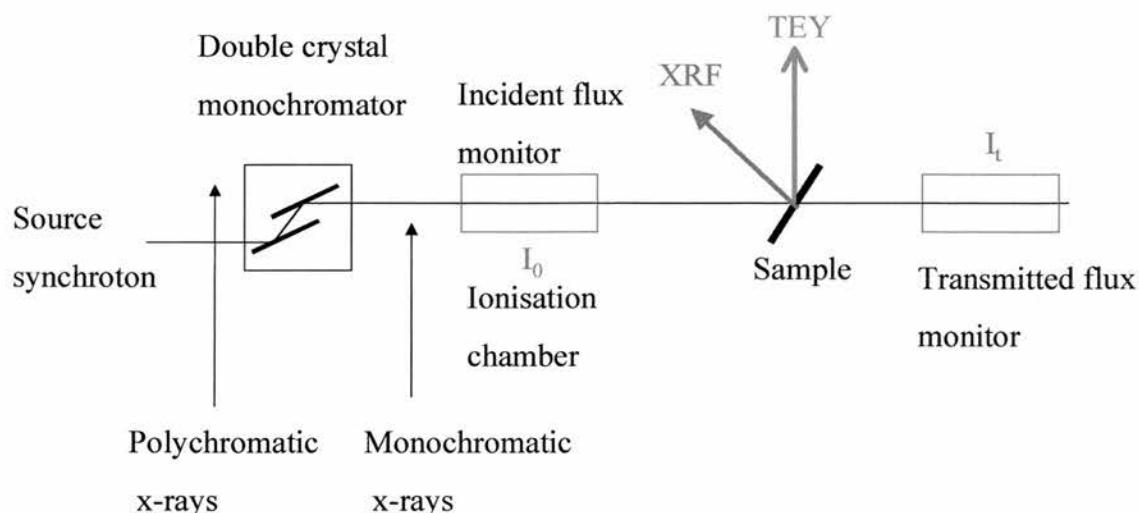


Figure 2.13 – A simplified instrument configuration.²⁵

Basic data in an EXAFS experiment is x-ray absorption data, i.e. measurement in the difference in energy between the incident and final beam (and thus the energy absorbed). There are three main ways in which to measure the final beam – Transmission, Fluorescence (or X-Ray Fluorescence – XRF) and Total Electron Yield²⁶ (TEY). Transmission measures the transmitted beam in the second (I_t) ion chamber. Fluorescence measures the scattered beam at a scintillation detector. TEY measures, as suggested, all the electrons emitted by the excited sample. TEY was tried with samples in this study but the technique was found to be unsuitable, due to the low electronic conductivity of the samples at room temperature

EXAFS Theory

EXAFS is a measurement of the absorption coefficient of a material relative to the energy of the incident beam. The Absorption Coefficient, μ , is derived from the following equation:

$$I = I_0 e^{-\mu t}$$

Where I_0 is the incident intensity and I is the final intensity of the beam, with t being the thickness of the material.

In EXAFS, the area of particular interest is the modulation of this coefficient above an x-ray absorption edge. Thus we can define the EXAFS portion ($\chi(E)$) as:

$$\chi(E) = \frac{\mu(E) - \mu_0(E)}{\Delta\mu_0(E)}$$

This has subtracted the 'bare atom' background, $\mu(E_0)$, and divided out the edge step, $\Delta\mu_0(E_0)$. This is the basis of background subtraction routines such as ECABS, and provides a 'normalised' spectrum, as shown in Figure 2.14.

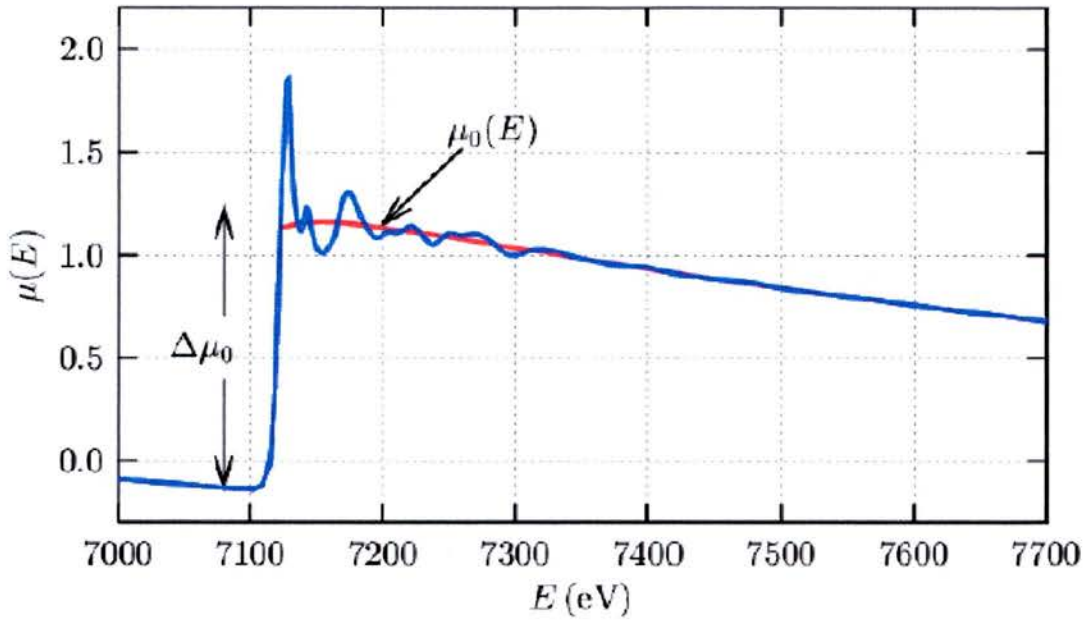


Figure 2.14 – The origin of the EXAFS

EXAFS tends to be given in terms of photo-electron wavenumber (k), rather than x-ray energy as it is more convenient and useful, particularly when working in k^2 or k^3 when the fainter oscillations further on in the spectrum are amplified to give a more meaningful impact on the spectrum. k is given by:

$$k = \sqrt{\frac{2m(E - E_0)}{\hbar^2}}$$

Thus, an EXAFS spectrum can be collected, normalised and presented. However, to gain any structural information, a model must be applied and refined. The EXAFS is modelled using the EXAFS equation:

$$\chi(k) = \sum_j \frac{N_j f_j(k) e^{\frac{-2R_j}{\lambda(k)}} e^{-2k^2 \sigma_j^2}}{kR_j^2} \sin[2kR_j + \delta_j(k)]$$

Where $f(k)$ is the scattering amplitude and $\delta_j(k)$ is the phase shift of the neighbouring atoms. These depend on the atomic number (Z) of said atom. $\lambda(k)$ is the mean free path, which is dependant on inelastic scattering events. If these are known, from the structural model assumed, we can calculate:

- R The distance to the neighbouring atoms and
- N The coordination number of the neighbouring atom, and
- σ^2 The mean-squared disorder of the neighbour distance.

The dependence of $f(k)$ and $\delta_j(k)$ on Z can also allow the type of local scatterer to be determined. Z can usually be distinguished to within about 5. Thus, Y and Sc can be differentiated, but Y and Zr cannot.

Derivation of the EXAFS Equation

Assuming a simple event where an electron leaves the central atom, is scattered and returns, that $\chi \sim \Psi_{(\text{scatterers})}(0)$ and there is no disorder, then a simple model of the EXAFS can be built up.

The spherical wave of the electron is given by e^{ikr}/kr , with the scatterer at $r = R$, giving:

$$\chi(k) = \frac{e^{ikR}}{kR} [2kf(k)e^{i\phi\delta(k)}] \frac{e^{ikR}}{kR} + C.C.$$

Where C.C. is a complex conjugate. As described earlier, the scattering amplitude, $f(k)$, and the phase shift, $\delta(k)$ are imparted by the scattering atom.

The equation simplifies by combining terms, including the complex conjugate, to:

$$\chi(k) = \frac{f(k)}{kR^2} \sin[2kR + \delta(k)]$$

In a case with multiple (N) scattering atoms, all with thermal and static disorder given by σ^2 , the mean square disorder in R, the equation becomes:

$$\chi(k) = \frac{Nf(k)e^{-2k^2\sigma^2}}{kR^2} \sin[2kR + \delta(k)]$$

In a real system with different atoms at varied distances, this leads to the simplified EXAFS equation that is often presented:

$$\chi(k) = \sum_j \frac{N_j f_j e^{-2k^2\sigma_j^2}}{kR_j^2} \sin[2kR_j + \delta_j(k)]$$

This equation assumes elastic scattering from the spherical wave. In a real system, some of the scattering may not return to the original atom. Thus a damped wave function ($e^{ikr} e^{-r/\lambda(k)}/kr$) is used, where $\lambda(k)$ is the mean free path, which tends to be less than 25Å. This leads to the general EXAFS equation:

$$\chi(k) = \sum_j \frac{N_j f_j e^{\frac{-2R_j}{\lambda(k)}} e^{-2\kappa^2 \sigma_j^2}}{k R_j^2} \sin[2k R_j + \delta_j(k)]$$

The EXAFS Experiment

Once data is collected, it is treated using the theories given above. Practically, it is treated as follows.

Normalisation and summing of spectra

To transform an EXAFS spectrum obtained from a beamline into usable data is a process of several steps. The first step is normalisation, where instrumental factors, such as configuration, monochromator and data collection mode are taken out of the data to give a normalised spectrum. It may also be necessary to edit the spectrum to remove glitches. These one point spikes in the spectrum are normally due to small imperfections in the monochromator, so some can be predicted if the condition of the monochromator is known. At this point it is also possible to sum several spectra together to improve the signal to noise ratio of the data.

Background subtraction

Background subtraction involves removing the slope of the normal energy profile and the absorption edge from the EXAFS spectrum to leave the EXAFS data only. The parts of the collected data that are removed are shown by red lines in Figure

2.14. This can be done in one of two ways. The first way is to fit the slope by hand before and after the absorption jump and subtract it from the spectrum. This is the method used by Exbrook and also can be used with spreadsheet software for spectra with complex backgrounds. The second method is to fit several polynomials to the background and then subtract the polynomials from the data. This is the method used in Exback and is often considered to be more repeatable as it is less subjective.

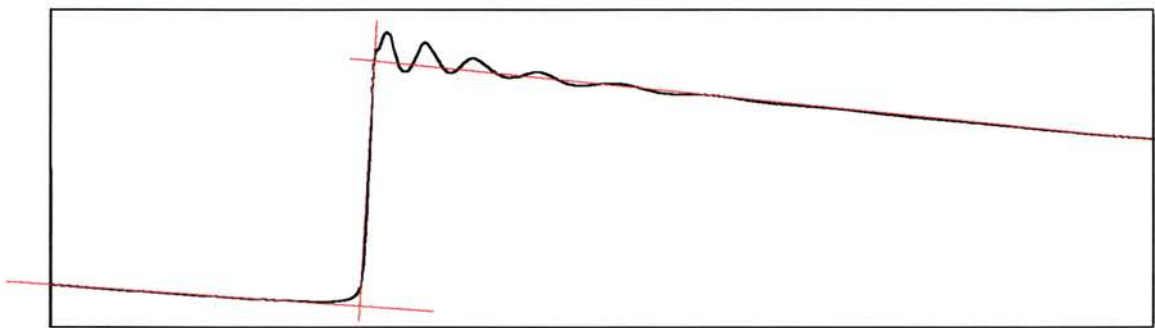


Figure 2.15 – Background subtraction on an EXAFS spectrum. Red lines indicate the part subtracted.

Background subtraction is unfortunately something of a black art and is the least scientific part of the EXAFS analysis. For no obvious reasons, some spectra subtract easily whereas others are considerably more difficult. However, as the data is subsequently fitted, background subtraction does not seem to have a great effect on the quality of the fit - as long as the subtraction is of a certain minimum standard, it is 'good enough'. Having said that, a poor subtraction will distort the data, so the minimum standard is important.

Errors in EXAFS

In many areas of the scientific community EXAFS has a bad reputation, partly through a misunderstanding of the technique and partly because of poorly presented data and, unfortunately, partly because of poorly analysed data in the past.²⁷ Thus, presentation of EXAFS data must be done with care and the conclusions drawn from the data must also be thoroughly explained.

Most errors in EXAFS come from poor sample preparation.²⁸ The ideal EXAFS sample is made up of small (~1 micron) particles of the substrate evenly distributed in a thin disc of a pure, spectroscopically invisible, binder (usually boron nitride or graphite).

This is going to have some effect on our results, due to sample preparation problems explained earlier. Errors in EXAFS usually drive the co-ordination number down; none increase them.²⁹

Experimental Method

In these studies, EXAFS experiments were conducted at Daresbury laboratories, using the instruments 9.3, 8.1 and 7.1.

Preparation of samples for EXAFS

All samples were ground as finely as possible using a steel percussion mortar and an agate pestle and mortar. Unfortunately, due to the extreme hardness of the doped

zirconia samples, it was not possible to grind the samples to the optimum particle size of roughly one micron and so typical particle sizes were up to 10 microns. This will cause a drop in the perceived co-ordination number.²⁸

For transmission experiments on instrument 9.3 the samples were intimately mixed in a ratio of 10:1 with a spectroscopically pure graphite binder and pressed into 13mm discs using a uniaxial pellet press.

For experiments on the instruments 7.1 and 8.1 samples were held as loose powder in metal holders using Kapton tape. For transmission experiments the samples were cut 10:1 with graphite but undiluted samples were used for reflectance geometry experiments.

Data Handling

Data handling was performed using the Daresbury suite of software, namely Ecabs or Excalib for normalising and summing data, Exback and Exbrook (within Ecabs) for background subtraction. Refinements were performed using the Excurv98³⁰ software running on the Daresbury computer *xrsserv1*. Particular refinement strategies will be discussed in Chapter Four along with the results they produced.

Nuclear Magnetic Resonance Spectroscopy (NMR)

NMR spectroscopy is a technique that probes the magnetic spin energy of atomic nuclei. For elements that have a non-zero spin, such as ^1H , ^6Li , ^{11}B and ^{13}C , an applied magnetic field will influence the energy of the nuclei. The applied field will split the spins into two different states, corresponding to the spins being parallel or anti-parallel to the applied field. The difference in energy between these two states is very small, about 0.01 J mol^{-1} , comparable with radio frequency for the usually applied field. The magnitude of the energy change is dependent on both the element and the chemical environment; thus NMR can be used to distinguish atoms in different positions in a structure.³¹

NMR of solutions is a much more tractable technique. Large amounts of information are routinely gathered from solution-phase NMR studies. Until recently, little information could be obtained from solid-state NMR, however recent advances, such as Magic Angle Spinning NMR, have begun to provide more information from the solid state.

^{11}B is a NMR susceptible nucleus, having spin $3/2$. It is quite a 'good' NMR nucleus as it is about half as responsive as ^1H , far higher than other regularly used nuclei such as ^{13}C , and it has a natural abundance of about 80%.

There are two main forms of experiments with solid state NMR. These are simple static probes, which gives quantitative, but little qualitative or structural, information and Magic Angle Spinning (MAS), where the sample is spun at the so-

called Magic Angle of $54^{\circ} 44'$ to minimise crystal splitting of the NMR signals. This allows higher resolution NMR data to be collected.

Magic Angle Spinning NMR is becoming the standard technique for solid state NMR. The problem with measurements on static samples is that the many dipole-dipole interactions cause extreme line broadening in the resulting spectra, meaning spectra for many solids appear flat and without any peaks. By spinning the sample at the 'Magic Angle' of $54^{\circ} 44'$, these interactions disappear and sharp peaks are produced in the spectra, allowing for much more information to be gleaned about the system.

These dipole – dipole interactions give a broadening that is related to the following equation:

$$H_i(\text{CSA}) = (3\cos^2\theta - 1)(\text{other terms}) + (3\cos^2\theta - 1)\sigma IB_0$$

Where:

θ = The spinning angle, wrt the magnetic field.

σ = The isotropic chemical shielding.

I = The spin angular momentum.

B_0 = The magnetic field.

Thus, if $\theta = 54^{\circ} 44'$, then $(3\cos^2\theta - 1)$ becomes zero, thus eliminating all anisotropic chemical shifts, such as dipole-dipole interactions, leaving only the isotropic chemical shifts. This works provided that the spinning frequency is close to the

frequency spreads of the signal. If the spinning frequency is smaller than this then so-called 'spinning sidebands' are seen in the spectra.

The initial experiments conducted were simple probes to determine the 'amount' of borate in a particular sample. Further experiments were conducted using Magic Angle spinning. The MAS spectra were obtained at 160.47 MHz for ^{11}B and single pulse experiments were employed. The spectra were obtained in 2K data points, a 90° pulse of 1.75 μs , 30,000 Hz sweep and a pulse repetition rate of 15 seconds, with 16 scans required. No interference from spinning sidebands was observed, hence all experiments were spun at 4.5 kHz. Blanks were run of the rotors to ensure there would be no artefacts in the spectrum.

As ^{11}B is a spin $3/2$ nucleus, it leads to broader peaks than would be present with a spin $1/2$ nucleus, making it harder to obtain good structural information.

A. C. Impedance Spectroscopy

When making samples for possible fuel cell or other electrochemical devices, the d. c. conductivity is one of the most important factors in a given sample's testing. Conductivity can be measured in several ways. Ideally, the aim would be to measure the d. c. conductivity, however, this can be difficult. Problems, such as the build up of charge carriers at one electrode, tend to arise and so the equilibrium state is difficult to maintain under d. c conditions.

The alternative is a. c. impedance spectroscopy. It is possible to extract d. c. conductivity values from the a. c. data. It is also possible to use a. c. impedance to probe the different factors affecting conductance, such as electrode capacitance and bulk versus grain boundary conductivity. Measurements were traditionally taken using a Wheatstone bridge circuit where trial and error substitution of resistors and capacitors in the Wheatstone bridge led to an equivalent circuit for the sample. In modern day measurements the use of a frequency response analyser allows the a. c. impedance of a sample to be obtained directly and subsequent computer fitting of the equivalent circuit gives the circuit elements.

The technique generally involves driving an a. c. current of varying frequency through the sample:

$$\mathbf{I} = I_0 \sin \omega t$$

The impedance (Z) is given by:

$$\mathbf{Z} = \mathbf{V}/\mathbf{I}$$

If the circuit has no reactive component (i.e. no inductance or capacitance) then the voltage follows the current:

$$V = V_0 \sin \omega t$$

And the impedance is equal to the resistance.

$$R = V/I$$

In most cases there will be a reactive component and the impedance is given by:

$$Z^* = Z' - jZ''$$

The real term is related to the resistive component and the imaginary term is related to the capacitance and inductance. Impedance can be plotted as a Cartesian (Z' vs. Z'') or Polar ($|Z|$ vs. ϕ) plot, as shown in Figure 2.16.

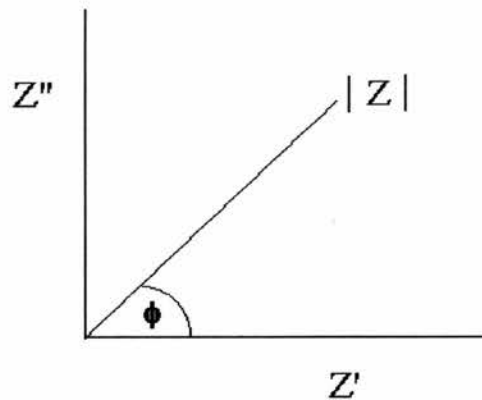


Figure 2.16 – Complex impedance Cartesian plot (Nyquist Plot)

Where $|Z|$, the magnitude and ϕ , phase lag, of the voltage. By convention, the current (I) leads the voltage, this is known as the phase shift and has the symbol ϕ , giving:

$$V = V_0 \sin (\omega t - \phi)$$

From this, it can be shown that:

$$Z' = |Z|\cos\phi$$

and

$$Z'' = |Z|\sin\phi$$

Measuring the impedance over a range of frequencies can give a complex impedance plot, with its equivalent circuit, as shown in Figure 2.17.

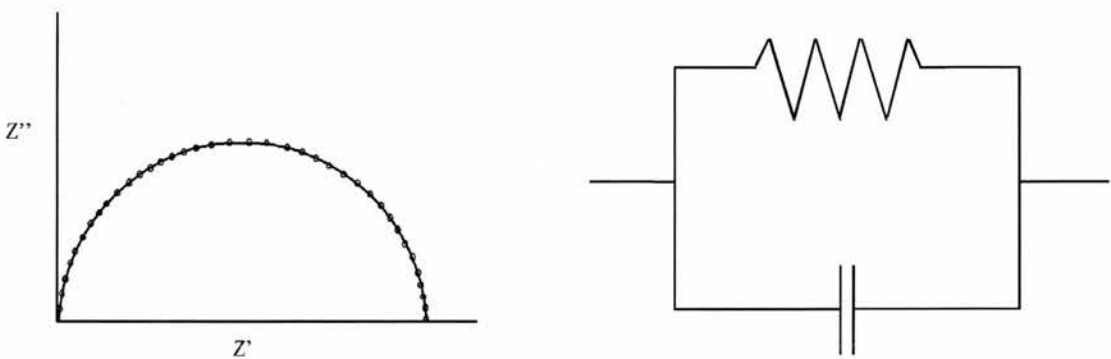


Figure 2.17 – An example frequency response and the equivalent circuit that it can be fitted to.

The semicircle in the impedance plane corresponds to an ideal response of a single element and can be represented by a RC parallel element with R relating to the electrical resistance and C (capacitance) relating to the dielectric response of that element. More than one semicircle is typically observed for a ceramic oxide ion conductor, with responses for grain boundary, surface layers, etc. also being present. The likely capacitance responses are shown for a 1 x 1 x 1 centimetre cube in Table 2.1 below. This allows parts of the spectra to be attributed to features in the sample.

In addition to the electrical response of the ceramic, the electrochemical response of the electrode is also often observed. Such responses are typically associated with a diffusion element distorting the semicircle giving an inclined slope on the high frequency side. Such features are indicative of oxide ion conductivity but otherwise not that significant.

Table 2.1 – Typical capacitance response in ceramic samples

Capacitance / F	Phenomenon responsible
10^{-12}	Bulk
10^{-11}	Second Phase
10^{-11} to 10^{-9}	Grain Boundary
10^{-7} to 10^{-5}	Surface layer or sample electrode interface
10^{-4}	Electrochemical interaction

Experimental Method

Samples were prepared for a. c. studies as sintered pellets. Once the sample had been shown phase pure by XRD then it was sintered at 1300°C overnight to form a good, dense pellet. The faces of the pellet were coated with platinum paste, which was sintered on to the pellet at 900°C. Measurements were taken at intervals of roughly 75°C from 300°C to 1000°C (the operating temperature for a fuel cell). Data was analysed using the commercial software Zplot.

References

- 1 A. R. West, *Basic Solid State Chemistry*, John Wiley and Sons, Chichester, 1984.
- 2 S. E. Dann, *Reactions and Characterisation of Solids*, Royal Society of Chemistry, Cambridge, 2000.
- 3 M. T. Weller, *Inorganic Materials Chemistry*, Oxford University Press, Oxford, 1994.
- 4 A. R. West, *Solid State Chemistry*, John Wiley and Sons, Chichester, 1984.
- 5 *Solid State Chemistry: Techniques*, A. K. Cheetham and P. Day (Editors), Clarendon Press, Oxford, 1988.
- 6 C. J. Brinker, G. W. Scherer, *Sol-gel Science*, Academic Press, London, 1990.
- 7 B. J. Mitchell, *PhD Thesis*, University of St. Andrews, 1998.
- 8 C. Hammond, *The Basics of Crystallography and Diffraction*, Oxford Science Publications, Oxford, 1997.
- 9 M. von Laue. *Ann Physik*, 1912, **41**, 989.
- 10 W.L. Bragg. *Proc Cambridge Phil. Soc.*, 1913, **17**, 43.
- 11 P. W. Atkins, *Physical Chemistry, 3rd Ed.*, Oxford Press, Oxford, 1990.
- 12 Courtesy of Ron Smith at RAL.
- ¹³ H.M, Rietveld, *Acta Cryst.*, 1966, **21**, A228.
- ¹⁴ H.M, Rietveld. *J. Appl. Crystallogr.*, 1969, **2**, 65.
- ¹⁵ *The Rietveld Method*, R. A. Young (Editor), Oxford University Press, Oxford, 1993.
- ¹⁶ J. Rodriguez-Carvajal. *15th C.Int.Un.Cryst.*, 1990, 127.
- 17 W. Kossel, *Z. Phys.*, 1920, **1**, 119.
- 18 R. de L. Kronig, *Z. Phys.*, 1931, **70**, 317.
- 19 R. de L. Kronig, *Z. Phys.*, 1932, **75**, 191.

- 20 D. E. Sayers, E. A. Stern and F. W. Lytle, *Phys. Rev. Lett.*, 1971, **27**, 1204.
- 21 E. A. Stern, *Phys. Rev. B.*, 1974, **10**, 3027.
- 22 F. W. Lytle, D. Sayers and E. A. Stern, *Phys. Rev. B*, 1975, **11**, 4825.
- 23 E. A. Stern, D. Sayers and F. W. Lytle, *Phys. Rev. B*, 1975, **11**, 4836.
- 24 J. W. Niemantsverdriet, *Spectroscopy in Catalysis*, VCH, Weinheim, 1993.
- 25 F. Belliard, *PhD Thesis*, University of St. Andrews, 2001.
- 26 S. L. M. Schroeder, *PhD Thesis*, University of Cambridge, 1996.
- 27 D. Huff, *How to Lie with Statistics*, Penguin Books, London, 1991.
- 28 Taken from Daresbury EXAFS course 2000, notes from which are available at <http://srs.dl.ac.uk/xrs/courses/errors/errors00.htm>
- 29 G. Bunker Lecture Notes – Available at <http://gbxafs.iit.edu/training/tutorials.html>
- 30 Binsted N. (1998) EXCURV98: CCLRC Daresbury Laboratory computer program.
- 31 *Encyclopædia of Nuclear Magnetic Resonance, Volume 2 (A – Com)*, D. M. Grant and R. K. Harris (Editors in Chief), John Wiley and Sons, Chichester, 1990.

Boron Doping of Yttria Stabilised Zirconia

INITIAL WORK	95
SETBACKS	97
A CLOSER LOOK AT THE PREPARATION METHOD	99
ALTERNATE PREPARATIONS	102
WEIGHT LOSS STUDIES	104
METHOD OF BORATE LOSS	106
PROBLEMS WITH THE ANALYSIS OF BORON IN CERAMICS	107
INFRA RED SPECTROSCOPY STUDIES	108
¹¹B NMR STUDIES	111
DISCUSSION	114
REFERENCES	118

Given the importance of the high oxide ion conduction of yttria stabilised zirconia, as discussed in Chapter One, a considerable effort has been made to try to tailor the properties of this material. The bulk of this work has involved the substitution of other metal oxides.¹ Unlike the lanthanum gallate system, where double doping of the metal lattice improves conductivity,² additional doping of the fluorite zirconia does not generally lead to a higher conductivity. This is due to the high level of original dopant needed to stabilise the cubic phase. Thus, in almost all cases where double doping has been tried, while many interesting phenomena have been observed, and interesting materials made, three metal systems have had lower basic oxide ion conductivity than YSZ. The exception to this are the Y-Sc-Zr oxides where scandium stabilises the cubic zirconia and results in a stabilisation of the cubic phase with less yttrium. These compounds are discussed at greater length in Chapters Four and Five.

There has been only limited work on systems in which the doping mechanism was not cationic. Reasons for this include a limited number of suitable dopants and difficulties with preparation and characterisation relative to the ease with which new metal dopants can be prepared. Despite this, given the importance of YSZ and the desire to improve its performance, the doping of the oxygen sub-lattice is a worthwhile research target. Given that the limit of maximum conductivity is reached with a

relatively small number of vacancies, due to the clustering of the vacancies,³ a tailored oxygen sub-lattice might give a considerable increase in conductivity if the effect of clustering can be reduced or mitigated in some way.

In 1996 Lin *et. al.*⁴ described the structure of $\text{La}_{26}(\text{BO}_3)_8\text{O}_{27}$, which is monoclinic but can be described as a distorted fluorite structure. In this structure the BO_3 trigonal planes 'cap' the empty cubes in the pseudo-fluorite structure. This structure is illustrated in Figures 3.1 and 3.2.

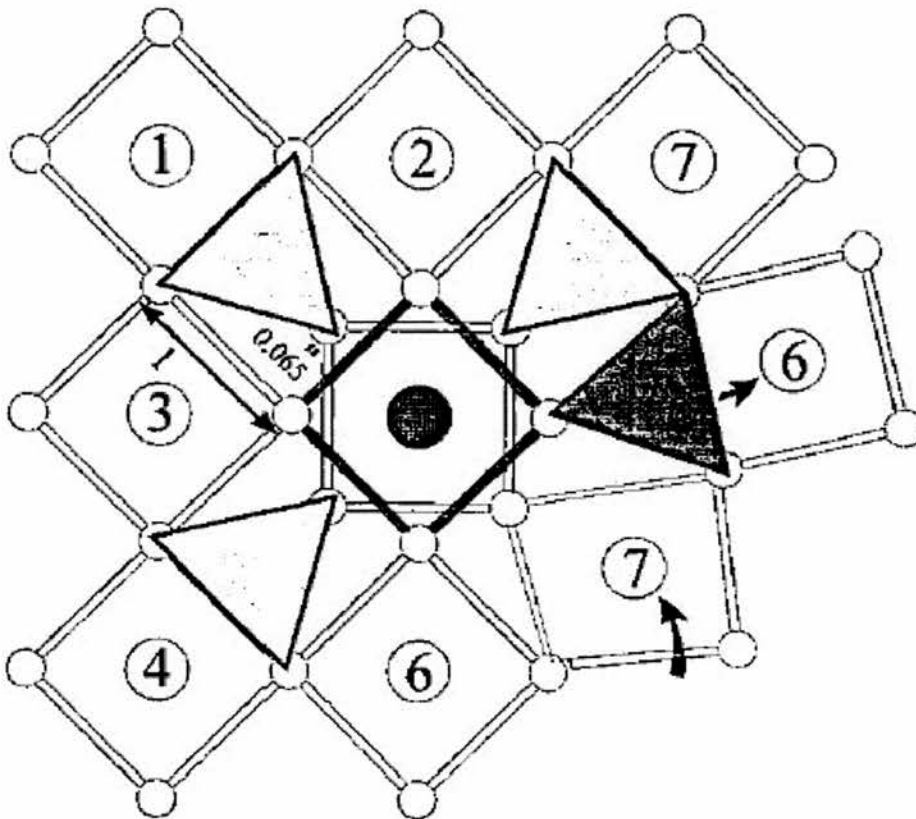


Figure 3.1 – The Distorted Fluorite Structure of $\text{La}_{26}(\text{BO}_3)_8\text{O}_{27}$. Triangles indicate the triangular BO_3^{3-} groups that cover the faces of the empty cubes

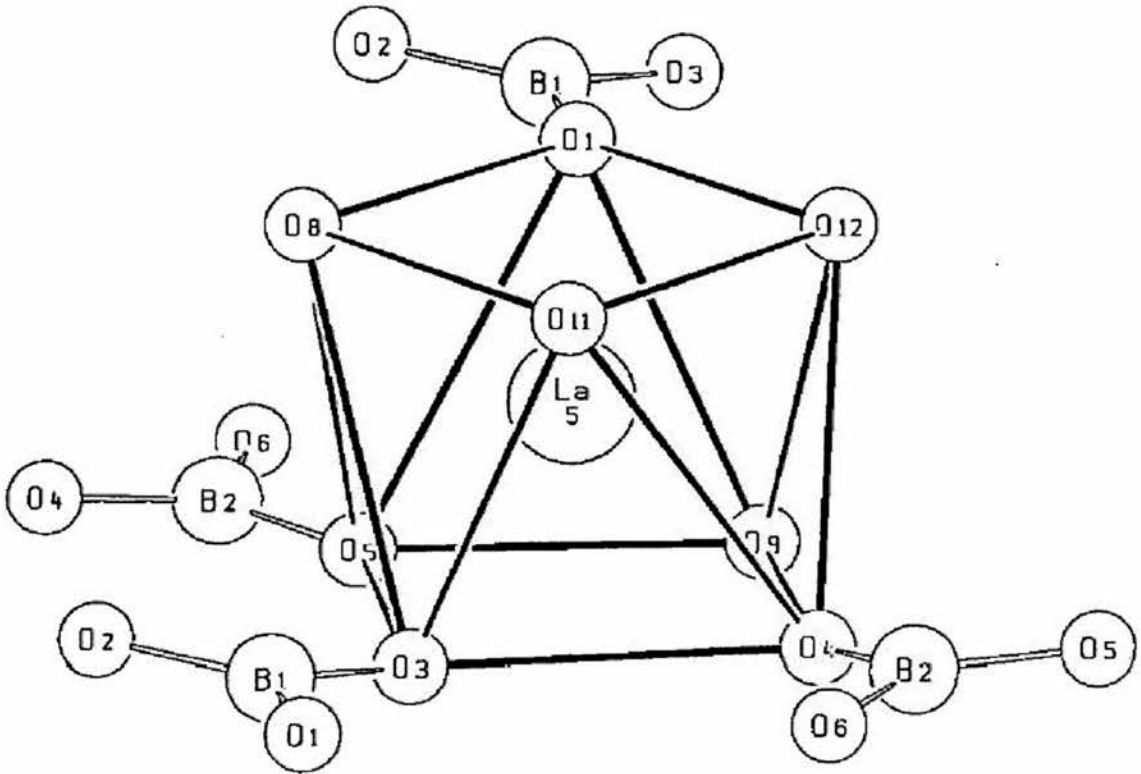


Figure 3.2 – The distorted fluorite structure of $\text{La}_{26}(\text{BO}_3)_8\text{O}_{27}$ with the lanthanum ion central.

With this as a proposed model structure, it was thought that borate (BO_3^{3-}) might be doped into the fluorite structure of YSZ. This would have several effects on the structure.

Firstly and most simply, the introduction of a negatively charged species into the structure would require some form of charge compensation. This would most likely be achieved by an increase in the number of oxygen vacancies.

Secondly, there could be an effect on the stabilisation of the cubic structure. As mentioned in the introduction, the stabilisation of the cubic phase is not trivial and is not

entirely understood (although theories abound on the subject). If the current highest performing YSZ (8 mole % YSZ, which is only meta-stable) could be fully stabilised it would have a potent effect on the lifetime of fuel cells as the performance of 8YSZ degrades over time. Having said this, the absence of any great structural change is quite possible as the boron-oxygen bond is tolerant of a great deal of variety in the bond length.⁵ Complex boron – oxygen chains and structures are known by geologists to form in some minerals and they often have little effect on the overall structure,⁶ which tends to be driven by the larger atoms.

Thirdly and finally, if the borate is introduced in some regular way then we have the possibility of some form of supercell structure being created. This would be of great theoretical interest as no new fluorite supercell has been discovered in many years.

Initial work

Initial experiments were performed to dope YSZ with borate and seemed to be quite successful. The first samples were prepared by the conventional solid state mixing method and characterised using x-ray diffraction. A wide range of samples, as detailed in Figure 3.3, were thus prepared.

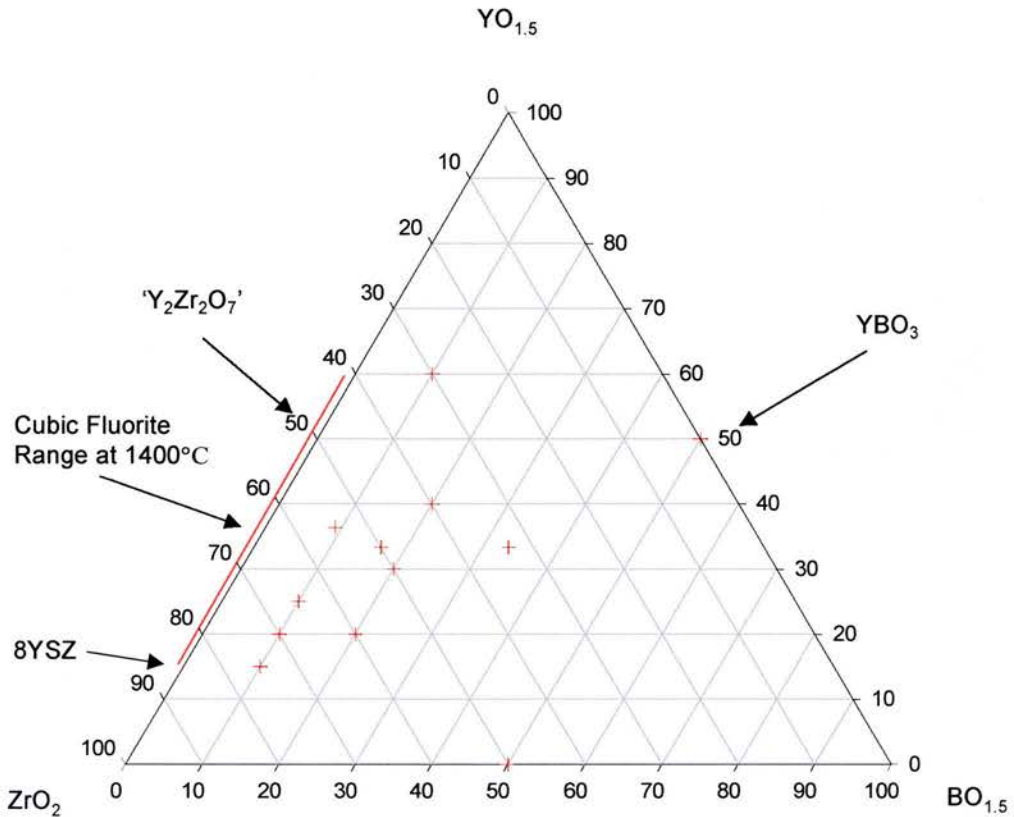


Figure 3.3 – Ternary Plot of the System $\text{ZrO}_2 - \text{YO}_{1.5} - \text{BO}_{1.5}$

This initially seemed to be both a simple and effective method for making pure samples, as they were routinely phase pure by x-ray diffraction. All the samples depicted in the centre of Figure 3.3 produced characteristic cubic (Fm-3m) patterns when analysed using x-ray diffraction, with unit cell parameters close to, but not identical to, those expected from the given yttrium-zirconium ratio.

Two samples were not cubic. These were the hexagonal yttrium borate⁷ (space group $\text{P6}_3/\text{m}$) which had been made as a standard as it was a possible impurity phase and the monoclinic Zr-B-O composition, which appeared to be simple mixture of pure

ZrO₂ (P2₁/c) with a small amount of residual B₂O₃. This appeared not to have reacted at all.

Setbacks

While these results were certainly very encouraging, further work to characterise these samples using ¹¹B NMR and infra red spectroscopy showed considerably less signal from the boron than was expected from the original composition. It appeared that the samples had virtually no boron in them at all. This is shown in the unspun NMR patterns in Figures 3.4 and 3.5.

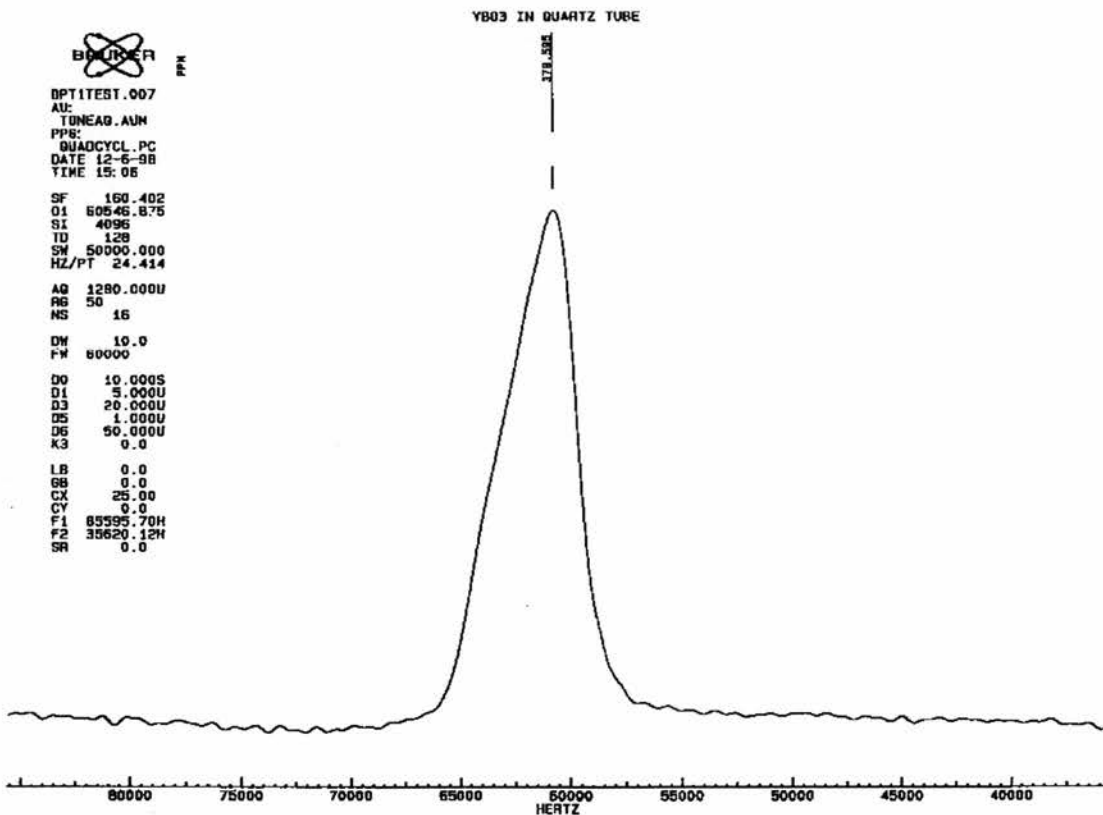


Figure 3.4 – NMR of YBO₃ in a quartz tube. 16 cycles.

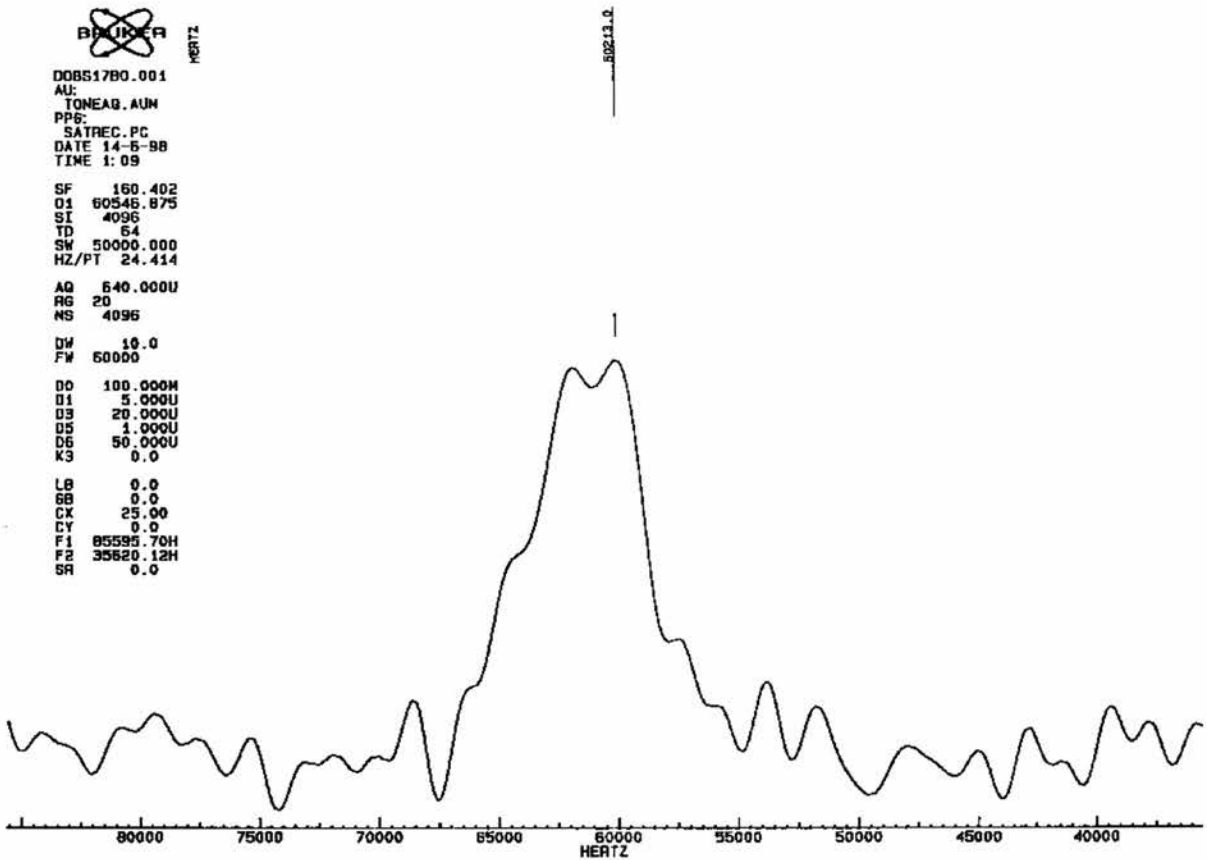


Figure 3.5 – NMR spectrum of 16B 34Y 50Zr. 4096 cycles.

As can be seen from the signal to noise ratio and the large number of cycles, this sample has very little borate in it. A ‘back of the envelope’ style calculation from the signal to noise ratio gave the nominal 16B 34Y 50Zr sample a borate content of about 1%.

This caused considerable confusion to start with, as none of the papers this work was based on had reported any difficulty with the loss of borate in the synthesis of similar compounds in temperatures up to 1350°C.^{4,8} The work of Chadeyron *et. al.*⁹

detailed a YBO_3 preparation at elevated temperatures with only a slight borate excess, indicating that it was seen as relatively stable in conjunction with yttrium.

A further series of samples was prepared with regular analysis of the weight of the samples. These revealed a substantial loss of weight, equivalent to the removal of almost all the initial borate added. The limit of solubility in open firing is estimated at somewhere between 1-2 atom %. These results are discussed more fully later in this chapter.

A closer look at the preparation method

With the problems of borate loss established, it is worth examining the solid state processes involved in the reaction of yttria and zirconia with the borate. Both yttria and zirconia are refractory oxides with melting points well over 2000°C . It requires high temperatures to improve the sluggish reaction dynamics of the metal ions (the oxygen is already highly mobile, facilitating oxide ion conductivity). By contrast, B_2O_3 melts at 450°C and YBO_3 at 1373°C .¹⁰ YBO_3 is formed at temperatures of 1150°C so the melting of the B_2O_3 is not problematic. Due to these factors reactions were performed at 1300°C or 1350°C to try to get complete reaction.

Because of the low firing temperatures, relative to the normal preparation of YSZ, the x-ray diffraction patterns were not always cubic at the end of a single firing, indicating incomplete reaction of the yttria and zirconia. Example x-ray diffraction patterns are shown in Figures 3.6 – 3.8, below. The main impurities seem to be YBO_3

and trace amounts of monoclinic zirconia. This would seem to indicate that the melting of the B_2O_3 is not a problem as it can still react with the yttrium to produce the YBO_3 seen in the patterns.

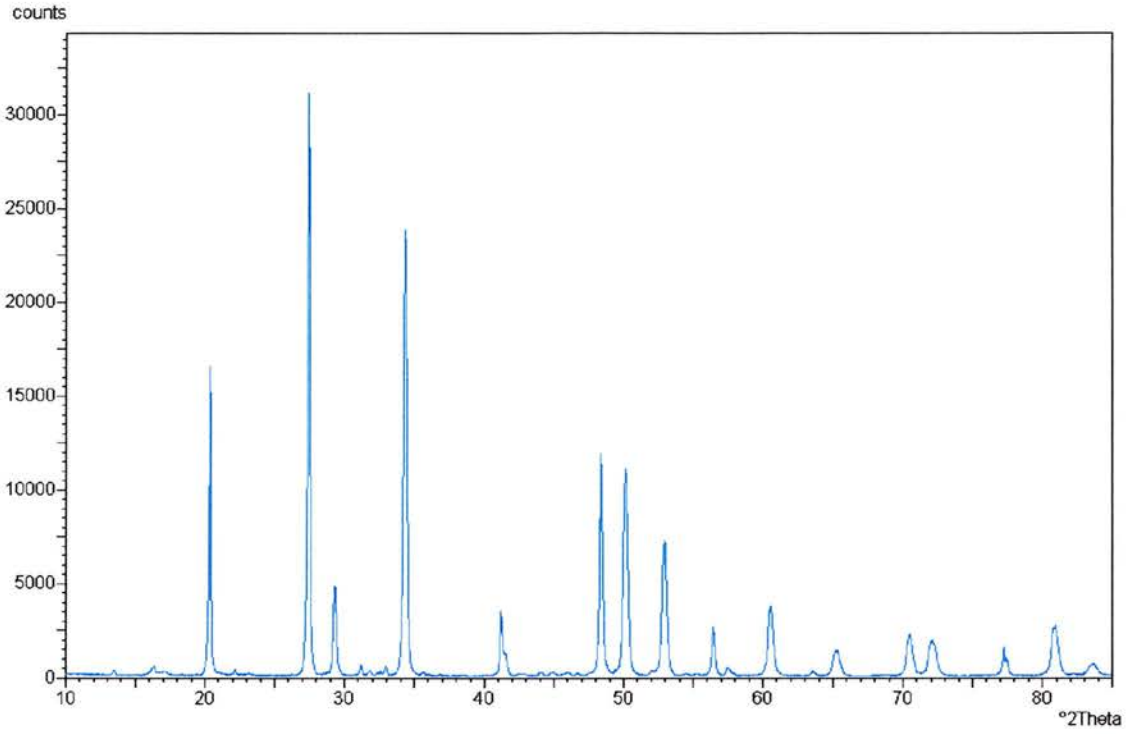


Figure 3.6 – X-Ray Diffraction Pattern of YBO_3

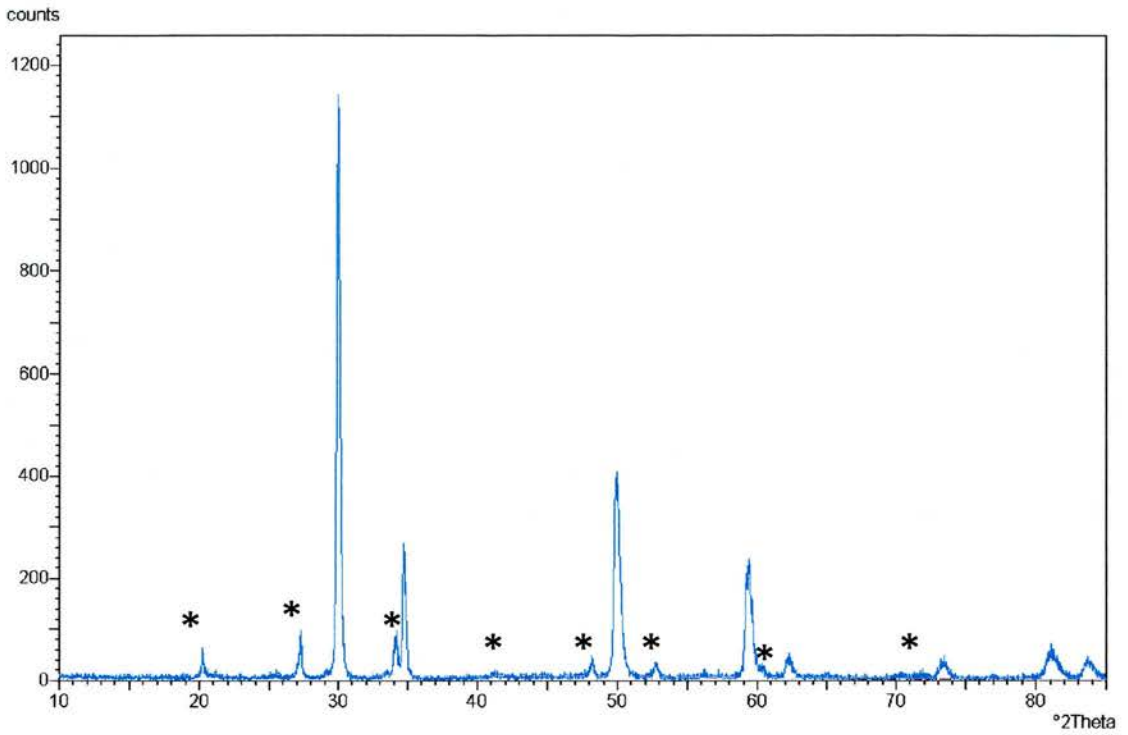


Figure 3.7 – X-Ray diffraction pattern of a partially reacted sample. The YBO_3 impurity phase peaks are starred.

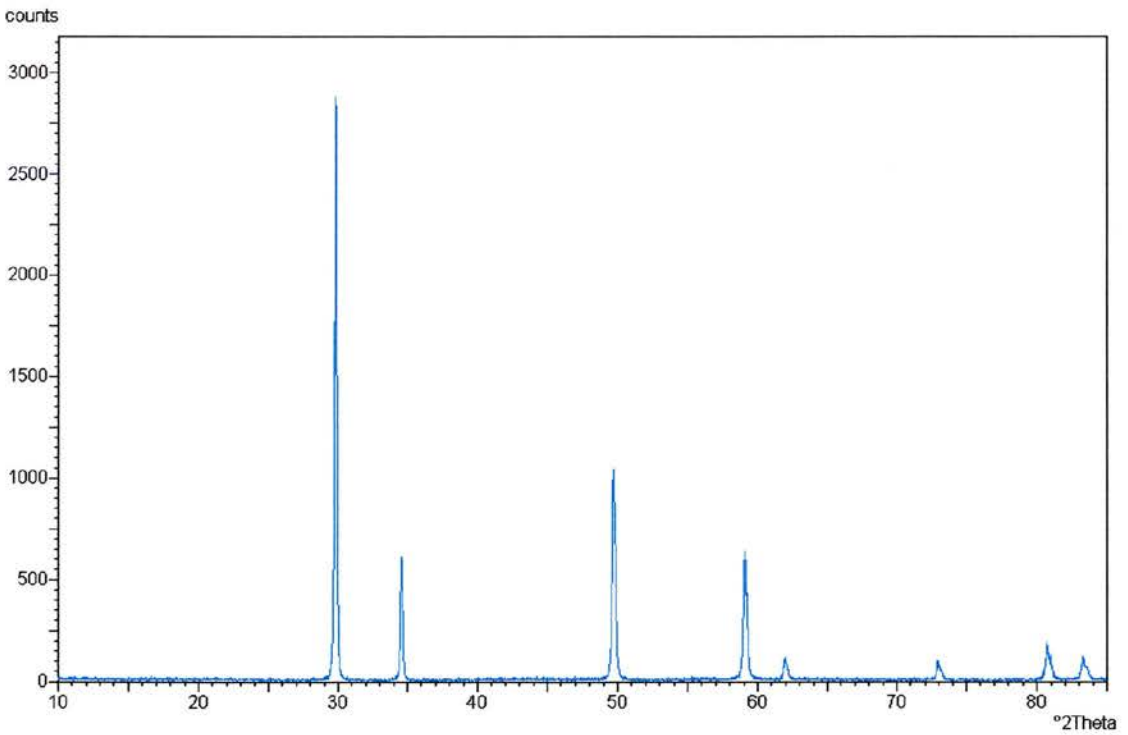


Figure 3.8 – X-Ray Diffraction Pattern of fully reacted YSZ doped with borate.

The samples that showed impurities would then be re-ground and re-fired at similar temperatures to achieve the complete reaction. This second firing is obviously problematic, as it is a second chance for the borate to be removed from the samples.

Alternate Preparations

As the initial preparation method was obviously not ideal, alternative methods were assessed in an attempt to increase the level of borate doping. Two different approaches minimising the borate loss were tried – lowering the temperature of reaction and direct prevention of the loss.

The first method was to use a gel method, as described in Chapter Two. This was chosen as it tends to produce extremely fine powders after the gel has been burned off. These are inherently more reactive than hand ground or ball-milled powders as they have a much greater surface area for reaction and thus shorter reaction paths for the inter-diffusion of the reactants. This allows reactions to proceed at lower temperatures which it was hoped would reduce the extent of borate loss. These lower temperatures are problematic however as, although reaction to cubic YSZ is completed at low temperature, the pellets are soft and unsintered and thus unsuited to further electrical testing. Sintering for densification is a shorter process than solid state reaction, so periods of elevated temperature, where the borate is lost, can be reduced.

Partial reaction was even seen at the temperatures required to remove the last of the gel. X-ray diffraction patterns of the pre-fired mixture were almost all cubic when

the gel had been removed at 800°C, which is normally only possible at temperatures approaching 1500°C for mechanically mixed samples. This is illustrated in Figure 3.9.

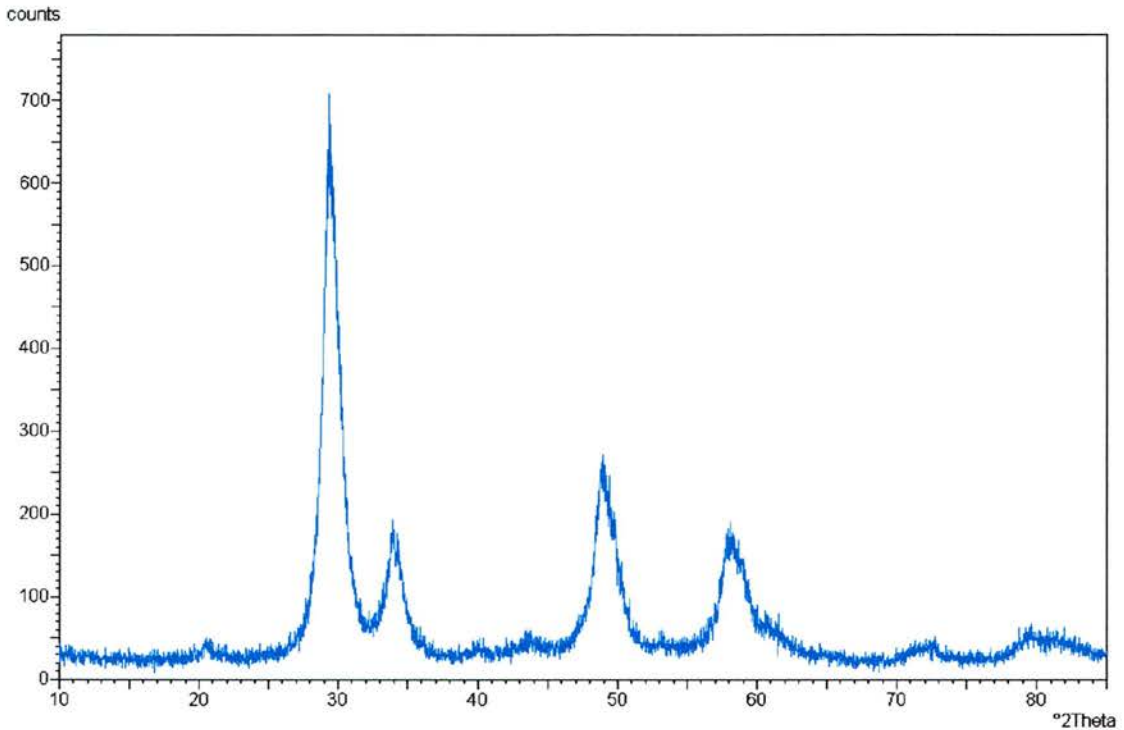


Figure 3.9 – X-Ray Diffraction pattern of a sample made by the gel method. The broad peaks are due to the small particle size.

The second method was to use sealed systems with sacrificial powders. This assumes that the borate is initially being lost from the outside of the reaction mass. By wrapping the sample in a sacrificial powder, the central pellets will be cushioned from the loss and therefore will have longer to react completely. The crucibles were sealed to provide for the possibility that the mechanism might be via a gas phase. If this is the case, once a certain vapour pressure of borate has built up (hopefully from the sacrificial powder) no more should be lost. This method is illustrated in Figure 3.10

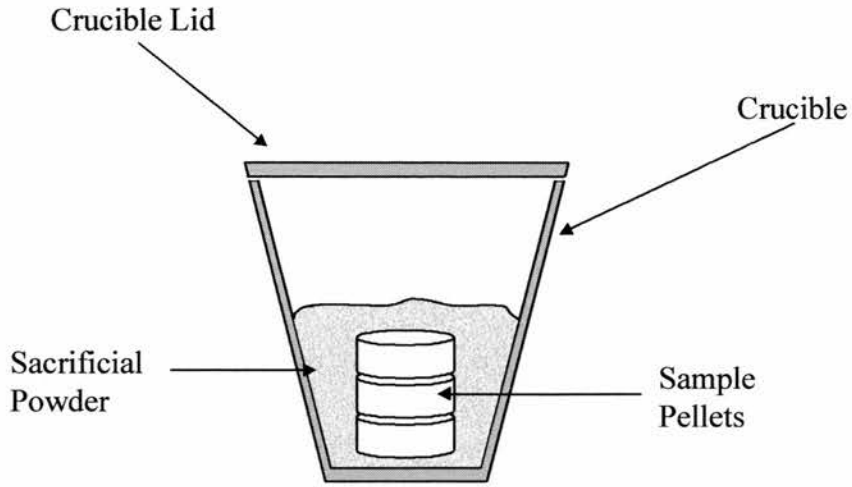


Figure 3.10 – Schematic of protective measures used.

Weight Loss Studies

All these methods were assessed using careful weighing of the samples. The results of these weight loss studies are presented in Figure 3.11.

As can be seen, the most successful approach was the use of sealed environments and sacrificial powders. The loss in “a” on the diagram accounts for almost all the initial borate, whereas the protected method, “d”, has lost only a small fraction of the initial amount.

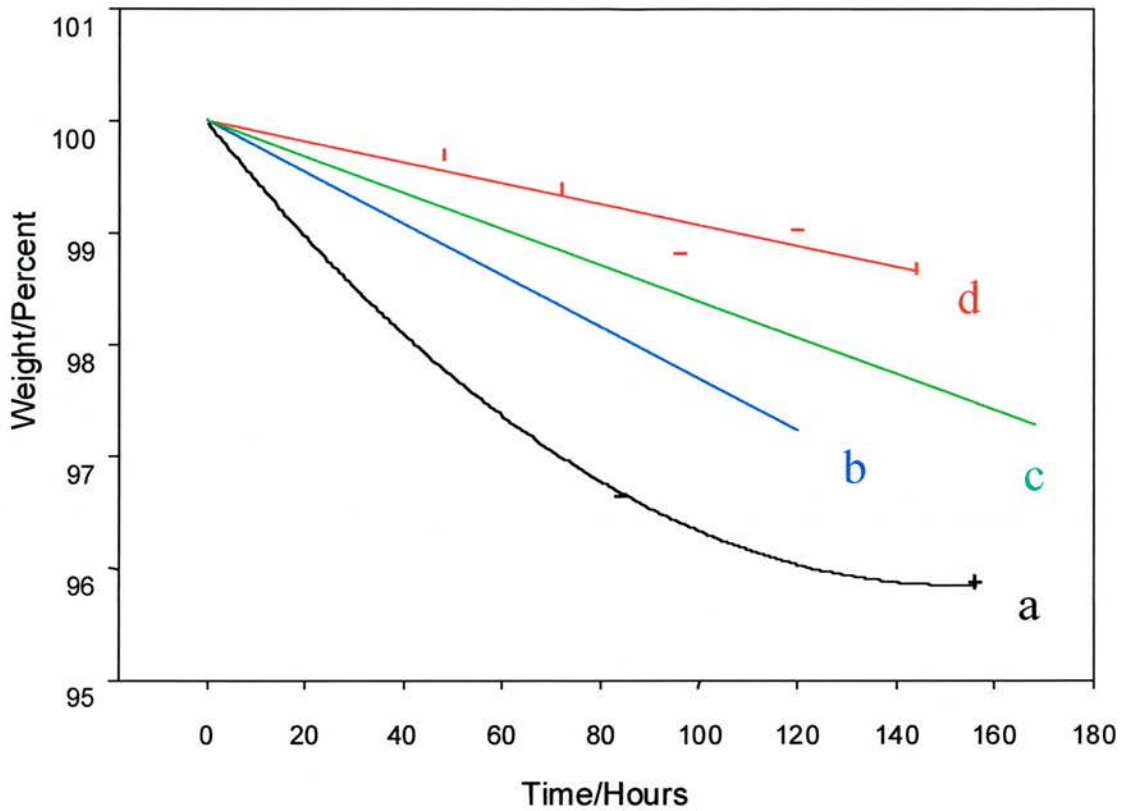


Figure 3.11 – Weight loss in various YSZ-Borate compounds.

a - " $B_{0.2}Y_{0.3}Zr_{0.5}O_x$ " – “Shake and bake”, unprotected and fired at 1300°C.

b - " $B_{0.2}Y_{0.2}Zr_{0.6}O_x$ " - prepared by a gel method and fired at 1000°C.

c - " $B_{0.1}Y_{0.225}Zr_{0.675}O_x$ " - prepared by a gel method and fired at 1000°C.

d - " $B_{0.2}Y_{0.2}Zr_{0.6}O_x$ " - Prepared with protective methods and fired at 1300°C.

As can be seen, the most successful approach was the use of sealed environments and sacrificial powders. The loss in “a” on the diagram accounts for almost all the initial borate, whereas the protected method, “d”, has lost only a small fraction of the initial amount.

From this, it appears that the second, preventative, method is the most suitable as the minimum of weight is lost, indicating at least partial incorporation of borate into the

samples. Additionally, pellets are almost fully dense after this treatment without the need for the additional sintering required for the gel methods.

Method of borate loss

An interesting side result is that the weight loss of a sample prepared with a sacrificial powder but an ill-fitting lid to the crucible lost almost all of the mass of the initial borate from the product, as badly as if no measures had been taken. This would seem to indicate that the borate is being lost via a gas phase mechanism. B_2O_3 has a very high projected melting point of 2250°C ¹⁰, so this had initially seemed unlikely. However $(BO)_x$, a reduced borate chain system, is known to volatilise between 1000°C and 1300°C , the temperatures we are using for firing. From this it is suggested that the boron is being reduced at these temperatures and then lost via the gas phase. Thus the mechanism in Figure 3.12 is proposed as a possible means for this loss.

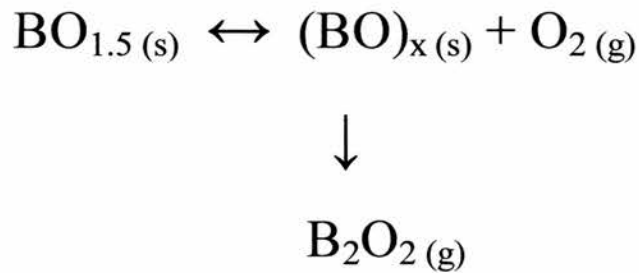


Figure 3.12 – Possible reaction schematic for the loss of borate.

Problems with the analysis of boron in ceramics

In the weight loss studies we have shown that it is possible to incorporate borate into the fluorite structure in some manner. These weight loss studies are intriguing but give little information on the structure and siting of any borate remaining in the ceramic or any mechanism for doping. It would therefore be useful to have a second test for the amount of borate doped in to the system.

However, characterisation of boron in these systems is difficult. There are numerous chemical tests for boron that have been developed over the years,¹¹ but they almost all require the boron to be in solution. As the YSZ matrix is almost entirely insoluble in anything this makes these techniques virtually unusable.

The workhorse of solid state chemistry, x-ray diffraction, can indicate when the sample is and is not fully reacted but cannot be used as a probe for boron in these circumstances. The small size of the boron ion relative to the much heavier yttrium and zirconium ions in the samples means that the boron is practically invisible to x-ray diffraction. However, x-ray diffraction can be used to monitor the unit cell edge for any changes which can be associated with the slight changes in structure caused by the incorporation of boron.

Neutron diffraction is similarly unhelpful as, of the two isotopes of boron, ^{11}B is practically invisible to neutrons with an absorption cross section of 0.0055 barns and ^{10}B is used as a neutron moderator with an absorption cross section of 3835 barns.¹² Neutron Absorption has been used as a probe for boron in biological samples but this

would probably be an expensive and unhelpful approach, as it only reports the presence or absence of boron, not any structural information. This information has been mostly seen from the weight loss studies and NMR studies already performed.

Two techniques did provide some useful information, Infra Red spectroscopy and ^{11}B Solid State NMR. These are discussed below.

Infra Red Spectroscopy Studies

Infra red is a useful technique as it requires little sample and can be used to quickly establish the presence of boron to oxygen bonds. This is shown in the infra red spectra of yttrium borate, our reference compound, in Figure 3.13, below.

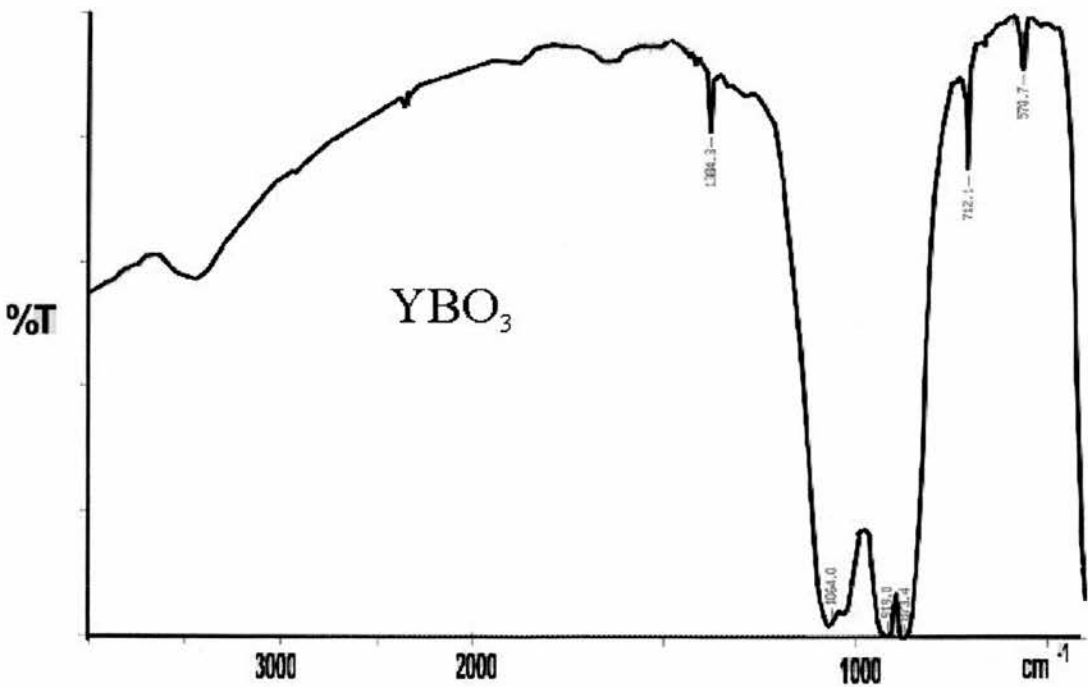


Figure 3.13 – IR spectrum of Yttrium Borate

By contrast, simple YSZ shows no signals at all in the infra red spectrum. The powders used did give rise to a characteristic shape in the spectrum as is shown in Figure 3.14, below. The large sweep at high wave numbers so characteristic in the spectra is due to the size of the particles. This is difficult to reduce as the YSZ can be very hard and even extended grinding does not always reduce the particle size sufficiently.

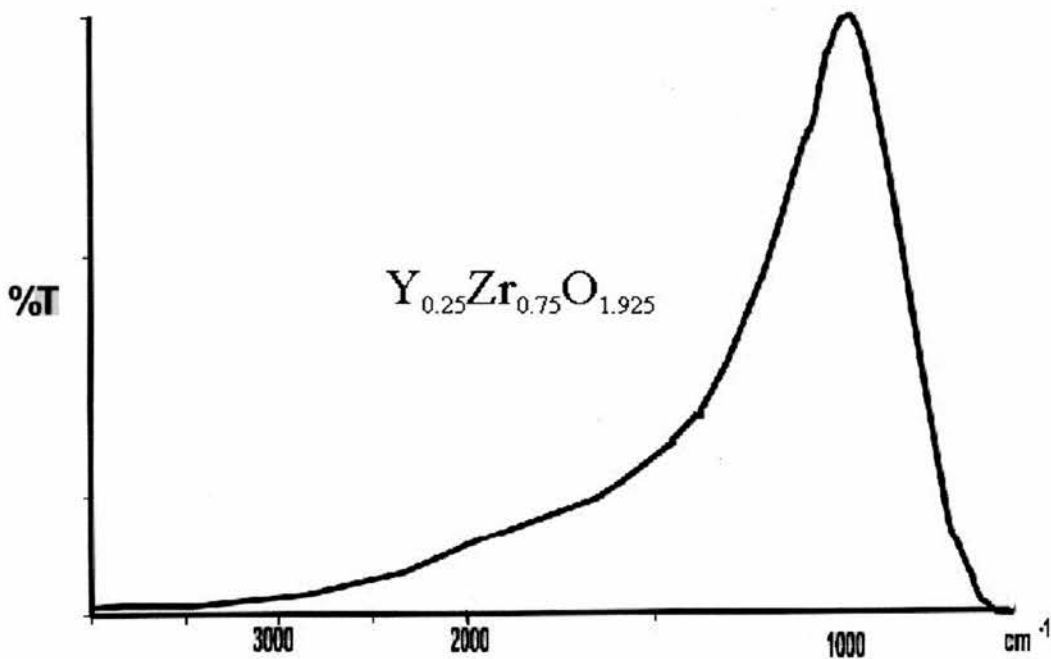


Figure 3.14 – The IR spectra for YSZ.

When YSZ is doped with the borate, the infra red spectra shows signals around the 1000 cm⁻¹ mark, similarly to YBO₃. This makes IR useful as a diagnostic tool to show the presence of borate. A sample pattern is shown in Figure 3.15, below.

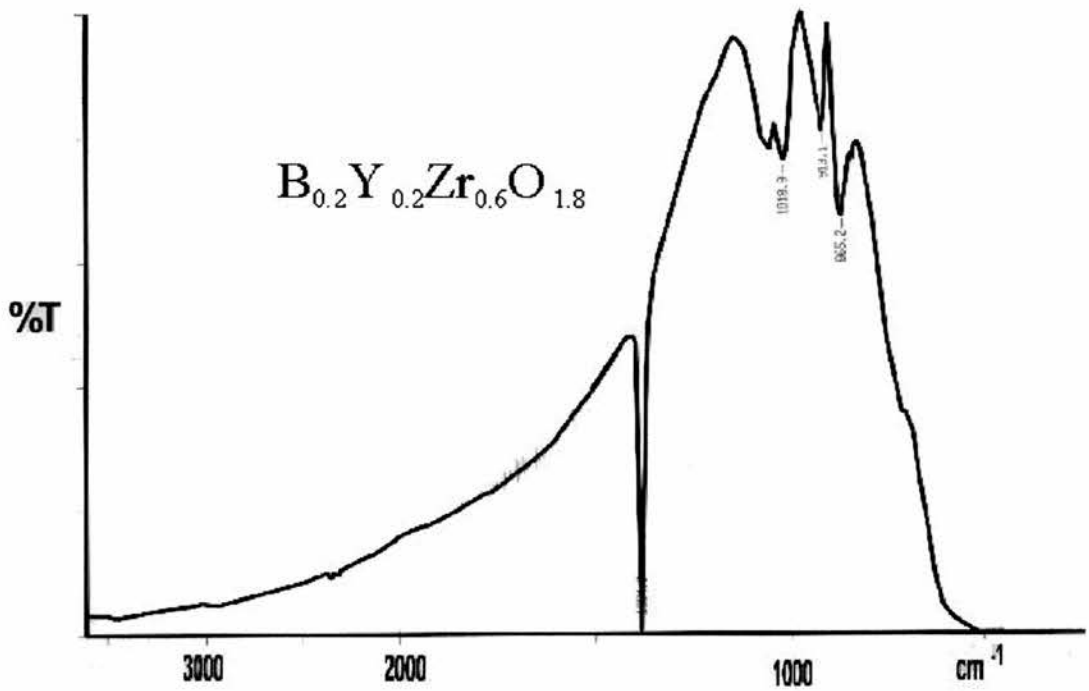


Figure 3.15 – IR spectrum of Borate doped YSZ

As can be seen from the spectra, collated in Table 3.1, Infra Red is useful as a quick test for the presence of borate in the YSZ. However, it is not immediately quantitative or structurally specific and it can be difficult to calibrate to be so.

The band structure is similar between the two systems, but is not identical. All the same peaks are present above 800 wave numbers, but their relative intensities are not the same. For YBO_3 the 1384 peak is minor, yet it is the largest peak in the BYSZ pattern. All the major peaks from the YBO_3 pattern (the set of four from 1064 to 870) are minor in the BYSZ case, with the 873 YBO_3 peak shifted slightly to 865 in BYSZ. This would seem to indicate that the structures of the borate are related, but not identical in these two systems.

Table 3.1 – Infra Red peaks in BYSZ and YBO₃

Sample	IR peaks in V/cm ⁻¹
Y _{0.16} Zr _{0.64} B _{0.2} O _{1.9+x}	1384 (strong)
	~1064 (medium – not picked by machine)
	1018 (medium)
	913 (weak)
	865 (medium)
YBO ₃	1384 (weak)
	1064 (strong doublet)
	~1018 (strong – not picked by machine)
	919 (strong)
	873 (strong)
	712 (weak)
	570 (weak)

¹¹B NMR studies

¹¹B NMR is probably the most useful technique for boron characterisation and was also the technique that originally highlighted the loss of borate during the initial doping reactions. Magic angle spinning NMR experiments have shown some similarities between the environment of boron in a doped YSZ sample to that in the YBO₃ system. The peaks in both the YBO₃ and the BYSZ spectra are at the same chemical shift - indicating that the boron is probably in the same environment in each sample. This is not the same as saying there is YBO₃ in the BYSZ. The boron is simply in the same environment. As it is surrounded by oxygens and almost certainly in a BO₃ cluster, this is not proof either way. It does show there is no chain formation e.g. B₂O₅. These spectra are shown in Figures 3.16 – 3.17.

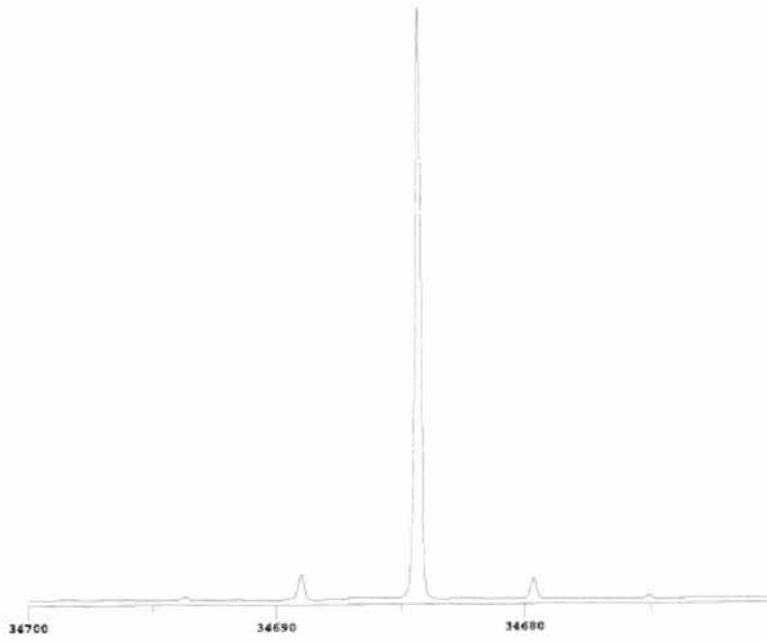


Figure 3.16 – YBO_3 spun at 4.5 kHz

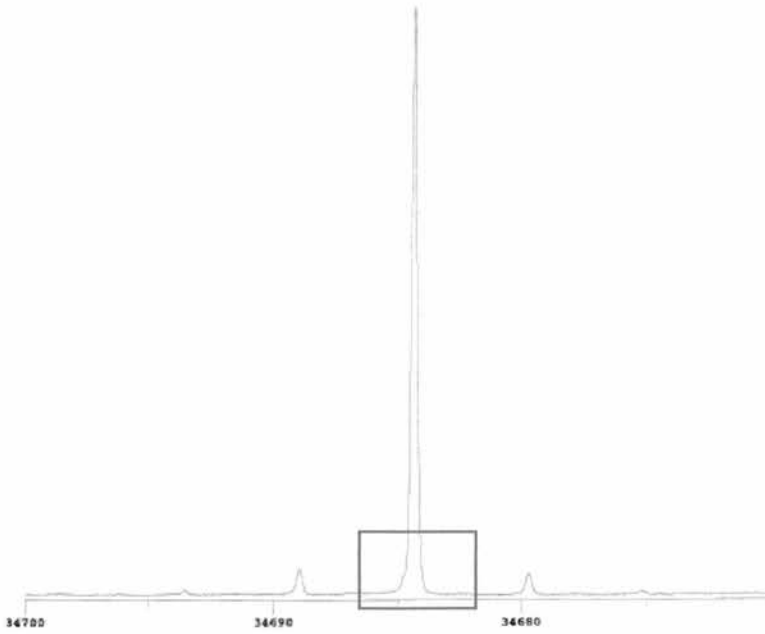


Figure 3.17 – “ $\text{Y}_{0.16}\text{Zr}_{0.64}\text{B}_{0.20}\text{O}_{1.82}$ ” spun at 4.5 kHz

Of these two spectra, the YBO_3 peak is the more intense, but that is not surprising, as there is a higher level of boron in this sample. This can be used as a guide to the amount of boron in the sample.

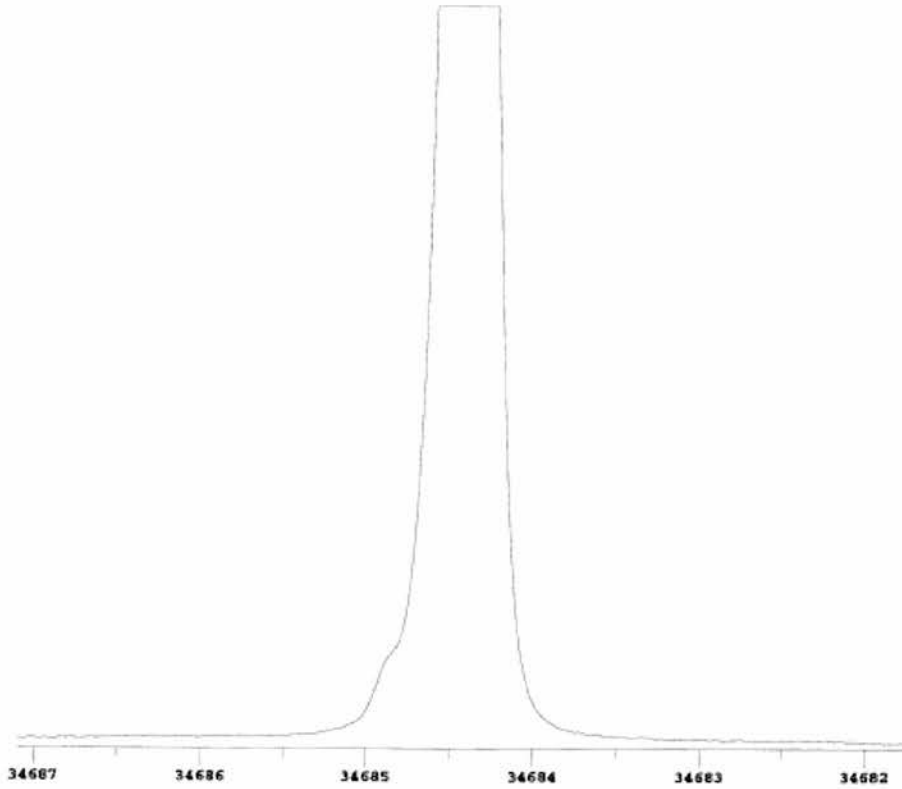


Figure 3.18 – Expansion of side peak on “ $\text{Y}_{0.16}\text{Zr}_{0.64}\text{B}_{0.20}\text{O}_{1.82}$ ” - spun at 4.5 kHz

Figure 3.18 shows an expansion of the base BYSZ peak, illustrating the presence of a shoulder which is absent in the YBO_3 spectrum. This could indicate the presence of a second related ^{11}B environment in BYSZ, at close to the same chemical shift of the main environment. The low intensity shows it is not the main phase.

Discussion

This work comes down to the simple question of whether boron can be incorporated into the matrix of yttria stabilised zirconia and, if so, in what form. As shown in the literature, there are several ways in which it could be incorporated, either into the fluorite structure, similarly to $\text{La}_{26}(\text{BO}_3)_8\text{O}_{27}$, as some form of long borate chain, in a similar way to many minerals, or as a separate phase, probably of YBO_3 .

While the initial results were obviously discouraging, further work has shown that it is possible to insert borate into the fluorite zirconia system. The evidence for this statement is collated in Table 3.2.

The results of the weight-loss studies show clearly that not all of the added mass of borate is lost, even after a considerable amount of time, therefore it may be concluded by this evidence that boron is incorporated into the structure in some way.

It remains to be discovered how the boron is incorporated. There are several reported oxides of yttrium and boron, but none of zirconia and boron. Attempts to mix borate and zirconia alone in this study were totally unsuccessful, leaving monoclinic zirconia and a second glassy borate phase, as evidenced by an early amorphous peak in the XRD. In the doped YSZ samples, there was no glassy second phase. All x-ray diffraction traces were completely cubic with exceptionally low backgrounds, indicating that the compounds were single phase. As some of the samples contained significant (roughly ten percent) amounts of borate yet were still single phase fluorite to x-rays, this

is a strong indicator that the borate is incorporated into the structure as part of the fluorite phase.

Table 3.2 – Collated evidence for the doping of borate into cubic YSZ

Sample	Fluorite Unit Cell Edge / Angstroms	Differences in the Infra Red Spectrum	Static ¹¹ B NMR Integrated Intensity
Y _{0.2} Zr _{0.8} O _{1.9}	5.151 (5)	N/A	N/A
“Y _{0.16} Zr _{0.64} B _{0.20} O _{1.82} ”	5.148 (5)	1384 – strong 1070 to 870 – weak	25.3
YBO ₃	N/A	1384 – weak 1070 to 870 – strong Extra peaks at 712 & 570	53.5

Infrared studies have shown some differences between YBO₃ and doped YSZ, with the differences being highlighted in Table 3.2. The band structure is very similar, yet the relative peak strength is very different, indicating, two related structures, probably with different strength bonds.

Impedance measurements on a sample of composition Y_{0.18}B_{0.08}Zr_{0.64}O_{1.87} indicate that the bulk conductivity is 1x10⁻⁵ Scm⁻¹ at 500°C. This is a factor of 50 less than the value expected for a sample with a Y : Zr ratio of 1 : 4. Although not encouraging in terms of conductivity, the magnitude of this change does show a significant change in the bulk of the material, possibly indicating that boron is incorporated into the lattice.

The NMR results are more puzzling, indicating that the boron “sees” both YBO_3 and the borate doped YSZ samples as the same structure. This could indicate the presence of YBO_3 in the samples, or could merely be pointing to some form of yttrium borate – such as a structure being formed within the fluorite. This could be complex, given that the model compound has three co-ordinate boron where the yttrium borate structure has corner sharing borate tetrahedra, as shown in Figure 3.19. Problems with the ^{11}B NMR arise because ^{11}B is a quadrupolar nucleus and, as such, has broad peaks even in MAS NMR. This means that species environment identification is still difficult, if not impossible, in this system and only co-ordination type is identifiable.

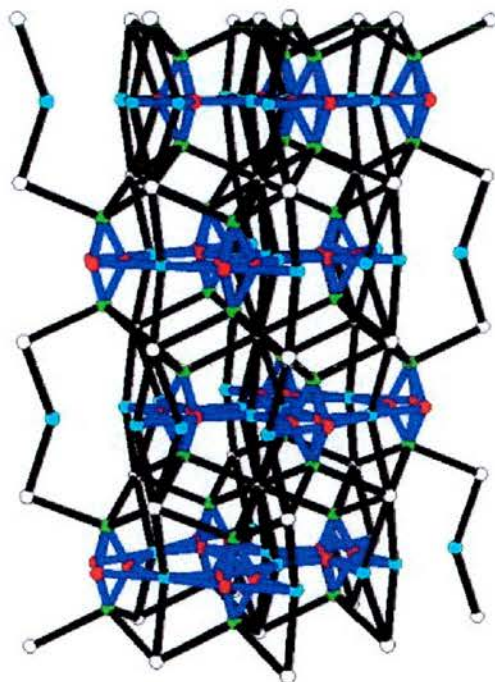


Figure 3.19 – The structure of YBO_3 . The red boron occupies one of the three possible positions, in a BO_4 tetrahedron between layers of yttrium.

One possible way to solve this problem is by using yttrium NMR. Yttrium is spin 1/2 and a very good NMR nucleus. If there is only one type of yttrium nucleus present, then we have a homogenous doped sample and a new solid solution. If there are two types of yttrium, then we have YBO_3 in YSZ. Due to technical problems with the NMR instruments, these experiments have not yet proved practicable.

To conclude, work on boron doping of YSZ has shown that the possibilities in more unorthodox methods of doping the structure, and other forms of anion doping could still prove very interesting.

References

- 1 E. C. Subbarao and H. S. Maiti, *Solid State Ionics*, 1984, **11**, 317 and papers within.
- 2 .T. Ishihara, H. Matsuda and Y. Takita, *J. Am. Chem. Soc.*, 1994, **116**, 3801.
- 3 C. B. Choudhary, H. S. Maiti and E. C. Subbarao, in *Solid Electrolytes and Their Applications*, ed. E. C. Subbarao, Plenum Press, New York, 1980, p. 1.
- 4 J. H. Lin, M. Z. Su, K. Wurst and K. Schweda, *J. Solid State Chem.*, 1996, **126**, 287.
- 5 N. N. Greenwood and A. Earnshaw, *Chemistry of the Elements, Second Edition*, Butterworth-Heinemann, Oxford, 1998.
- 6 *Reviews in Mineralogy 33 – Boron Mineralogy, Petrology and Geochemistry*, E. S. Grew and L. M. Anovitz (Eds.), Mineralogical Society of America, Washington, 1996.
- 7 R. E. Newnham, M. J. Redman and R. P. Santoro, *J. Am. Ceram. Soc.*, 1963, **46**, 253.
- 8 J. H. Lin, S. Zhou, L. Q. Yang, G. Q. Yao, M. Z. Su and L. P. You, *J. Solid State Chem.*, 1997, **134**, 158.
- 9 G. Chadeyron, M. El-Ghozzi, R. Mahiou, A. Arbus and J. C. Cousseins, *J. Solid State Chem.*, 1997, **128**, 261.
- 10 *Comprehensive Inorganic Chemistry*, Vol. 1, A. F. Trotman – Dickenson (Exec. Ed.), Pergamon Press, Oxford, 1973
- 11 . N. Sah and P. H. Brown, *Microchem. J.*, 1997, **56**, 285.
- 12 *Neutron News*, 1992, **3**, 29.

EXAFS Studies on Doped Zirconia

EXAFS IN THE LITERATURE	122
THIS STUDY	124
REFINEMENT METHODOLOGY	124
QUALITY OF DATA	125
ANOMALOUS PEAKS AND BACKGROUND SUBTRACTION	129
MULTIPLE SCATTERING IN THESE SAMPLES	133
RESULTS	135
YTTRIA STABILISED ZIRCONIA	136
Single Cluster Yttrium Work	136
Single Cluster Zirconium Work	138
Multi Cluster Yttrium Work	139
Multi Cluster Zirconium Work	141
YSZ Dual-Edge Work	142
YSZ Discussion	145
SCANDIA STABILISED ZIRCONIA	146
Single Cluster Zirconium Work	146
Single Cluster Scandium Work	150
Multi Cluster Zirconium Work	152
ScSZ Discussion	155

CO-DOPED YTTRIA SCANDIA STABILISED ZIRCONIA	157
Single Cluster Yttrium Work	158
Single Cluster Zirconium Work	159
Single Cluster Scandium Work	161
Multi Cluster Yttrium Work	162
Multi Cluster Zirconium Work	163
YScSZ Discussion	165
DISCUSSION AND CONCLUSIONS	165
REFERENCES	167

As described in the introduction, fluorite structured zirconia can be stabilised at room temperature by the addition of dopants. This gives rise to technologically important materials, such as yttria stabilised zirconia, which are useful oxide ion conductors. Whilst the bulk structure of these materials is described as a *defect fluorite structure*, there is a great interest in the precise short-range microstructure, particularly in the exact location of the oxygen vacancies and the possible occurrence of microdomain structures.

If all the oxygen vacancies were to move freely in these materials, the electrical conductivity might be expected to increase in proportion to the concentration of such vacancies and hence to extant dopant levels. The observed decrease in electrical conductivity at higher dopant concentrations has generally been attributed to some form of order among, or clustering of, these vacancies.¹

EXAFS is a useful technique with which to investigate short-range order and local microstructure in materials. It has already been applied in several studies of yttria stabilised zirconia, however conflicting results and conclusions have been drawn from these studies, as discussed below. To date, scandia stabilised zirconia or co-doped yttria

and scandia stabilised zirconia have not been studied using this technique. Presented here are EXAFS results from all three systems.

EXAFS in the Literature

Early EXAFS work on the YSZ system by Catlow *et. al.*² had indicated that the oxygen vacancies were located preferentially next to the zirconium ions at room temperature, with size effects being dominant. This appeared to be counterintuitive with respect to previous assumptions that the vacancies, [with an effective positive charge ($V_{O^{\cdot\cdot}}$)], would be preferentially sited adjacent to the Y^{3+} rather than the Zr^{4+} , in order to minimise charge density variations. Further work on the subject by Tuilier *et. al.*³ cautiously contradicted this result, claiming the vacancies *were* preferentially located next to the dopants. This work also pointed to considerable disorder in the anion sublattice, describing a “glass of anions” to account for oxygen displacements.

Other work has also produced similarly conflicting results. Goldman *et. al.*,⁴ Morikawa *et. al.*⁵ and Shan *et. al.*⁶ all considered the vacancies to be located next to the dopant species, whereas Komyoji *et. al.*⁷ and Veal *et. al.*⁸ reported the vacancies to be associated with the zirconium ion.

The matter appears to have been settled with the extensive works of Li *et. al.*^{9,10,11,12} They concluded that size was the most important factor determining the siting of vacancies, with vacancies being located next to the zirconium ions when large dopants such as yttrium or gadolinium were employed, but adjacent to the dopant ion for small dopant species such as iron or gallium. This latter point was also made in the

computer simulations of Zacate *et. al.*¹³ whose results indicated that oxygen lattice relaxation was the principal consideration.

All these results are only true for room temperatures. At elevated temperatures the anion mobility increases considerably (as shown by conductivity data) and this makes the yttrium and zirconium sites indistinguishable.²

More recently, EXAFS in zirconia systems has focused more on nanocrystalline zirconia,^{14,15} with little new work on bulk zirconia EXAFS except as standards. The view of Chadwick *et. al.* was that the EXAFS of the nanocrystalline phase was similar to that in normal bulk YSZ, even though previous workers had suggested it was highly disordered.

Studies on the related system of yttria doped ceria has shown that this too behaves in a similar manner, with vacancies clustering around the cerium and not the larger dopant. Several complex defect structures were proposed by Yamazaki *et. al.*¹⁶ for the location of vacancies in doped ceria, which may have analogues in zirconia systems.

This Study

In this study, we were interested in a comparison between the better understood YSZ system and the higher conducting but less studied ScSZ and YScSZ systems. Several YSZ samples were made as standards before experiments were done on the other systems. The YScSZ system was considered particularly interesting as it has a mixture of dopant sizes.

Refinement Methodology

All samples were initially refined using standard single scattering models. Multiple scattering was tried but found to be both slow and not especially effective. This is discussed in more depth in a later section.

The refinements were performed using a standardised method. A suitable model was applied, with bond lengths from earlier x-ray studies and co-ordination numbers as determined by stoichiometry, assuming a true defect fluorite structure and thus average distribution of vacancies. Debye Waller factors are left as set by the program. Initially the Energy Offset (or Fermi Energy - E_f) was refined, then the bond lengths (R1, R2, etc) and the Debye Waller factors (A1, A2, etc). Finally, once the model had settled into an energy minimum the co-ordination numbers (N1, N2, etc) were allowed to vary. The co-ordination number was never allowed to refine at the same time as the Debye Waller factors as this would almost certainly have led to correlations between the two. In this study only N1, the number of oxygens in the first shell, was varied at this stage as

yttrium and zirconium are virtually indistinguishable to EXAFS. The co-ordination numbers of shells corresponding to metal atoms were left as indicated by the stoichiometry of the samples.

The quality and accuracy of the refinements were checked using both the R-factors and the Fit Index. The R-factor is a indication of the fit of the EXAFS data in k-space and the Fit Index is a purely statistical guide. ¹⁷

Quality of data

As the yttrium and zirconium edges are next to each other they were collected simultaneously, using transmission spectroscopy on Instrument 9.3 at Daresbury Laboratories. The quality of data was universally good, as shown in Figures 4.1 and 4.2. As can be seen, there is better amplitude on the yttrium edge than on the zirconium edge, perhaps surprisingly given that this sample is $(Y_2O_3)_{0.1}(ZrO_2)_{0.9}$, which has a 15:85 Y : Zr ratio, and they were collected simultaneously.

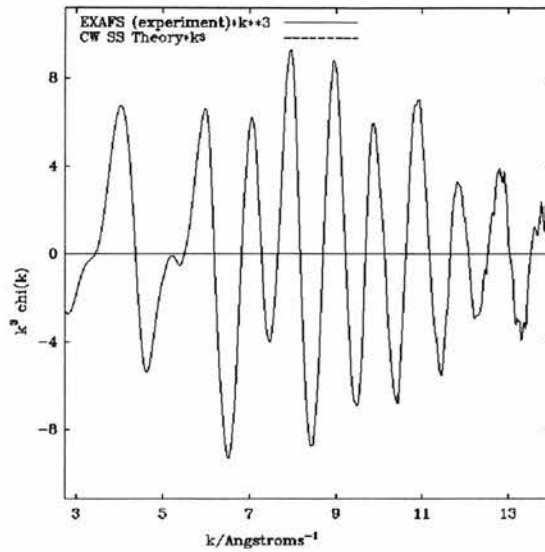


Figure 4.1 – Quality of data - Yttrium Edge

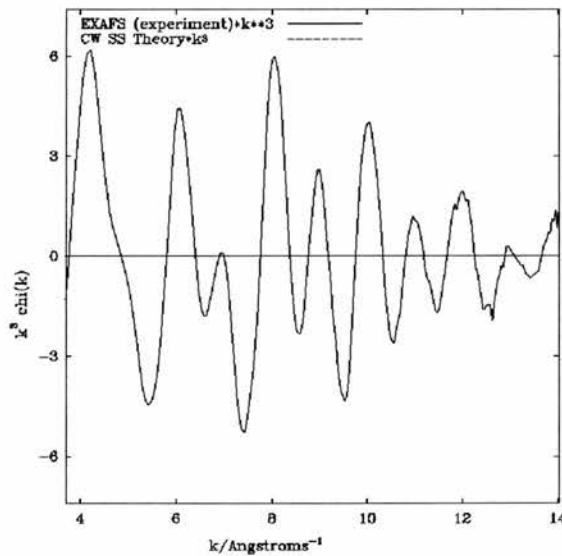


Figure 4.2 – Quality of data - Zirconium Edge

In contrast to this, the scandium edge data was much more difficult to investigate. Scandium scatters very weakly compared to zirconium and yttrium. As all the samples were mainly zirconium, it proved impossible to collect the data in

transmission mode. It was not possible to put enough sample into the beam to get a signal without blocking the beam entirely. Thus, most of the data was collected in fluorescence mode on Instrument 8.2. Data collection runs were therefore considerably longer, meaning fewer samples could be investigated and still much of the data was noisier than that collected in the YSZ system, as shown in Figure 4.3. This is in fact the best of the scandium edge data, with some being even noisier.

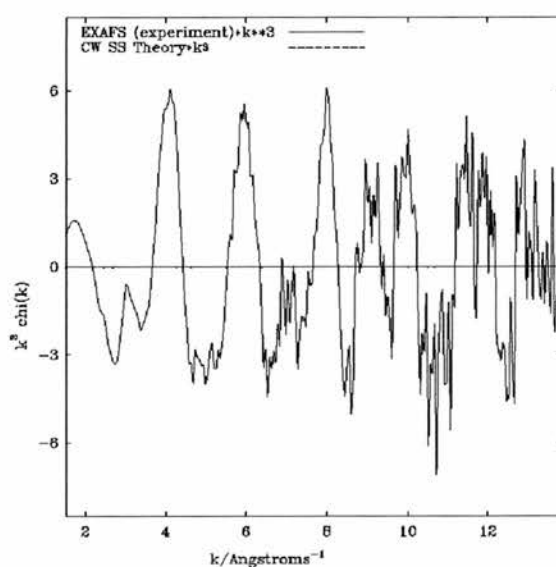


Figure 4.3 – Quality of data – Scandium edge.

Interestingly, the quality of the zirconium edge data in scandia stabilised zirconia was also noisier than that obtained for YSZ, as shown in Figure 4.4, although all of the data was collected in transmission mode on Instrument 9.3 on the same visit to Daresbury. This possibly points to greater disorder on the cation sub-lattice in these systems.

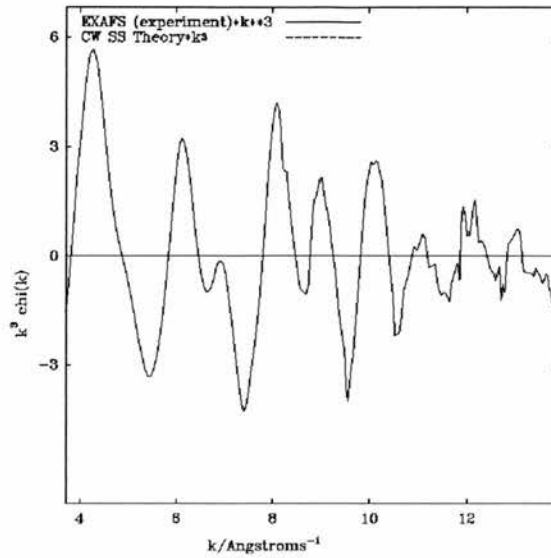


Figure 4.4 – Quality of data – Zirconium edge in scandium doped system.

Background subtractions of the scandium data were also complicated by the fact that the pre-edge tended to be curved due to the energy profile of the incident beam not being linear, as shown in Figure 4.5.

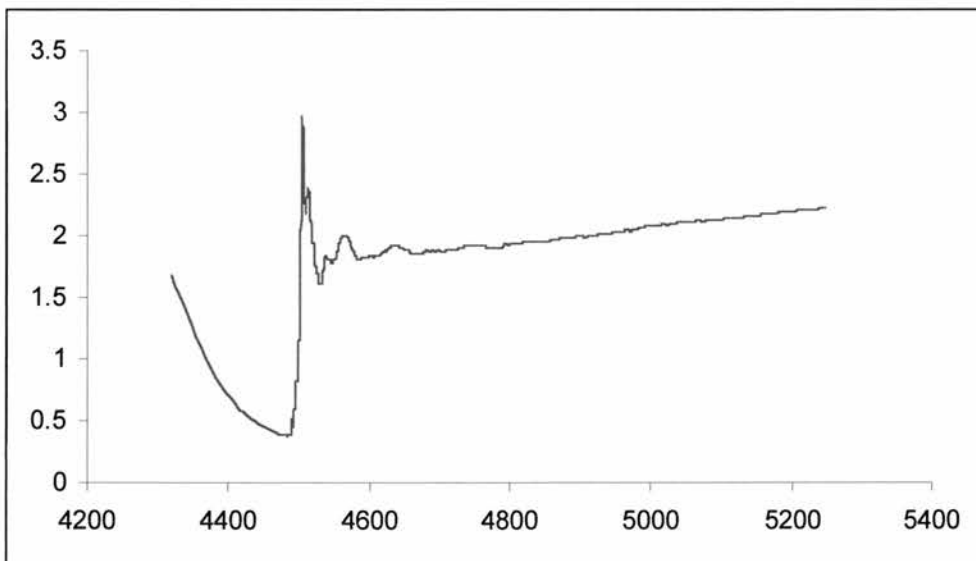


Figure 4.5 – Non-linear pre-edge on the scandium edge of $(\text{Sc}_2\text{O}_3)_{0.1}(\text{ZrO}_2)_{0.9}$

Anomalous Peaks and Background Subtraction

One feature of all the EXAFS spectra analysed in the various zirconia systems in this study has been a small peak at small distance (R) in the Fourier transformed data. This is shown in Figures 4.6 – 4.8.

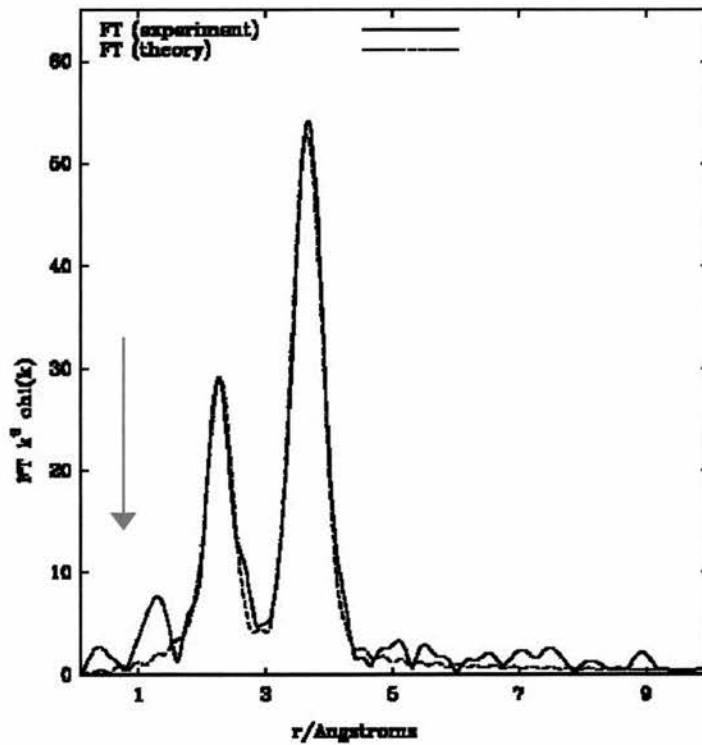


Figure 4.6 – Anomalous peaks in Yttrium edge Fourier transformed data

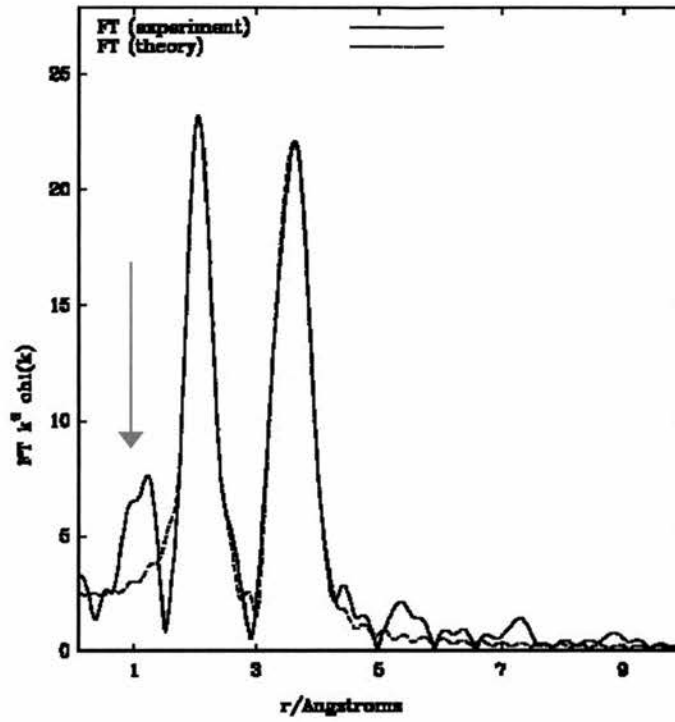


Figure 4.7 – Anomalous peak in Zirconium edge Fourier transformed data

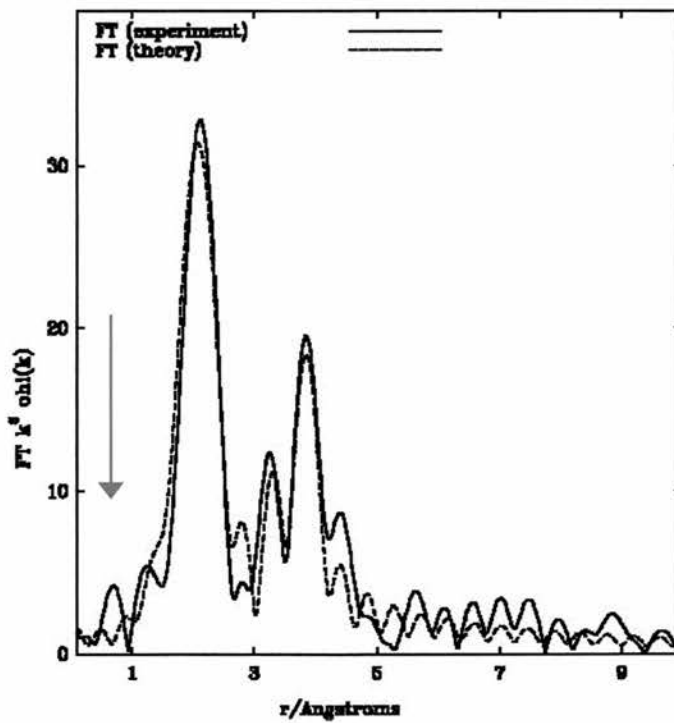


Figure 4.8 – Anomalous peak in Scandium edge Fourier transformed data

The exact cause of this is unknown, as it is too close to the central atom to be the electron cloud of another atom. Causes of this feature have been variously suggested as scattering from the outer shell of electrons of the central atom, Ramseur - Townsend scattering,¹⁸ noise at high k in the spectrum,¹⁹ double electron excitation on the central atom²⁰ or simply poor background subtraction.²¹

With the last option in mind, data for 10YSZ was examined using several separate background subtractions, including both a deliberately poor subtraction and a subtraction from the automated background subtraction routine “Autoback”,²² for which the Fourier transform is shown in Figure 4.9. The full results are presented in Table 4.1.

Table 4.1 – Differences due to background subtraction in the fit of $Y_{0.18}Zr_{0.82}O_{1.91}$

Attempt	Refined C/N (N1)	Y-O bond length (R1)	Debye Waller Factor (A1)	R Factor	Fit Index
1	7.801	2.314	0.017	18.28	0.00017
2	7.476	2.311	0.017	18.53	0.00016
3	7.5	2.310	0.017	18.52	0.00016
4	7.5	2.307	0.016	18.82	0.00017
Autoback	7.9	2.318	0.074	31.34	0.00017
Poorly Done	7.324	2.306	0.017	19.14	0.00022

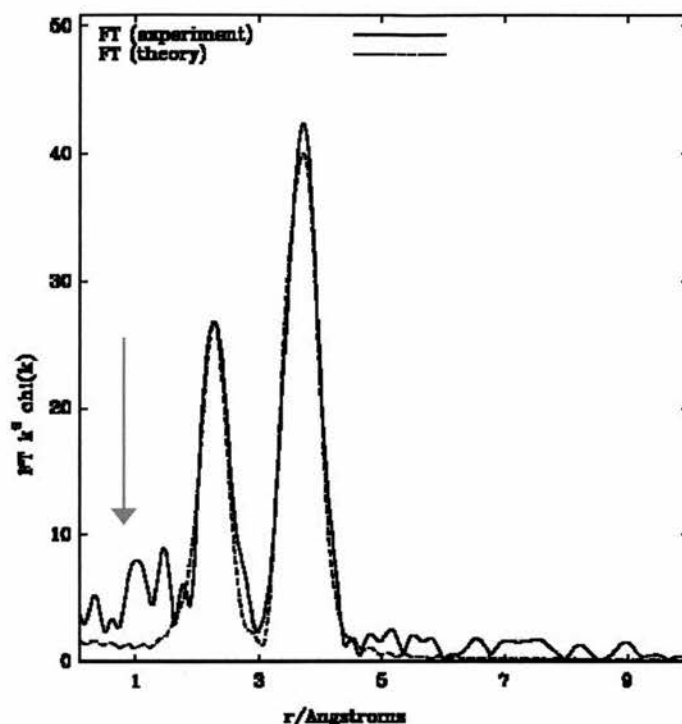


Figure 4.9 - Autoback Subtraction – Note worse early peak fitting

This reveals some interesting points. Firstly, while the background subtractions differ and do cause some variance in the fitted data, the final solutions are all obviously in the same energy minimum, even if some fits are obviously better than others. The bond distance on the first shell is also a lot more stable than the initial co-ordination number is, meaning it is possibly a better guide to the behaviour of the system.

Secondly, the early peaks appear to be real. Although it is possible to shift the peak slightly with differing background subtractions, it is not possible to remove them entirely. In the final analysis, it is the belief of the author that the peak is due to some form of double excitation similar to that described by Chaboy *et. al.*²³ This has not been proven, and remains conjecture only.

While the cause is still unknown, the effect has been observed by other workers in the field – density is present in the spectra published by Catlow *et. al.*² and Li *et. al.*¹⁰ The peak is also present in the EXAFS of nanocrystalline zirconia as reported by Rush *et. al.*¹⁵ Any errors due to this were assumed to be systematic and thus more attention was paid to trends and relative levels than to the absolute numbers.

Multiple Scattering in these samples

On the available evidence, it appeared that defect fluorite zirconia was an obvious candidate to show multiple scattering. The metals are regularly distributed and are strong scatterers, giving several possible multiple scattering pathways.

Multiple scattering occurs in all systems to varying degrees. It manifests itself in the Fourier transform of the EXAFS as extra peaks, which cannot be attributed to a shell of atoms. These peaks may overlay the peak from a shell of scattering, distorting the non-multiple scattering refinements.

The doped zirconia samples in this study do not show any large peaks in the Fourier transform besides the ones due to the first two shells of atoms (oxygen and zirconia/dopant shells). However, there are several smaller shells at integer and fractional multiples of the d spacing of the main peaks. As this could possibly indicate the presence of some secondary scattering contribution to the spectrum, the multiple scattering approach to refinement was tried with these samples.

For multiple scattering, the maximum path length of a scattering event (PLMAX in Excurv98) was set to 15 Å and the maximum number of scattering events (OMAX in Excurv98) was set to three. With the initial factors being so broad the computing overheads are considerable, but the vast majority of multiple scatterings are modelled.

This was tried with several samples. Reasonable fits were obtained using multiple scattering, with R values of 40 or so and a Fit Index of about .00130. However, these are not as good as those obtained by single scattering. The fits are ‘acceptable’ mathematically but they do not look good by eye, as shown in Figure 4.10. As a result of these experiments, all further zirconia data were fitted using the single scattering (standard) model.

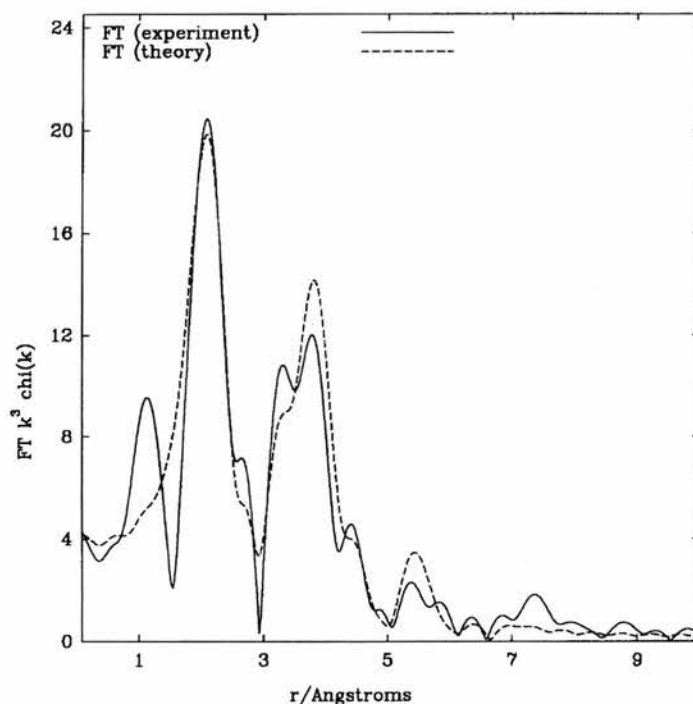


Figure 4.10 – Typical Fourier Transform of the multiple scattering fit of a doped zirconia. Note the poor match on the second fitted shell.

Results

Results from these studies follow. In each case, the analysis started with a simple single cluster model and then refined using more advanced options. They are reported sequentially by data series. A key is presented below to allow the reader to follow the numerous tables which follow.

Table 4.2 – Key to Tables

Title	Meaning
R Factor	Measurement of the quality of fit
Fit Index	Alternate measurement of fit
N1	Co-ordination number of Oxygen shell
R1	Radius of Oxygen shell
A1	Debye Waller (disorder) factor of Oxygen shell
R2	Radius of Zirconium shell
A2	Debye Waller factor of Zirconium shell
R3	Radius of Dopant shell
A3	Debye Waller factor of Dopant shell

Yttria Stabilised Zirconia

These samples were run initially as standards, however, closer examination of some of the data using multi cluster and dual edge refinement methods proved very interesting and so they are reported in detail.

Single Cluster Yttrium Work

As can be seen in Table 4.3, the data has refined easily to good fits. All the data is internally consistent, with good refinements easily possible. The main cause for the R factor being as high as it is is the presence of the initial early peak in the Fourier transform, which is not being modelled as was discussed earlier. This is a possible cause of errors on both co-ordination numbers and bond lengths²³ if, as believed by the author, it is due to double excitation events. Any errors due to this are assumed to be systematic and thus more attention is paid to trends and relative levels than to the absolute numbers.

The co-ordination number of the oxygen shell remains high, which is consistent with much of the work mentioned earlier. The fact that it falls considerably on the last sample is expected as there are now an equal number of yttrium and zirconium ions in the system, so it is statistically very difficult not to have some vacancies Nearest Neighbour (NN) to yttrium ions. Nevertheless, the case for preferential oxygen vacancy location next to the host zirconium rather than the dopant yttrium remains very solid.

Table 4.3 – Single Cluster Yttrium Data

	$Y_{0.15}Zr_{0.85}O_{1.925}$	$Y_{0.18}Zr_{0.82}O_{1.91}$	$Y_{0.4}Zr_{0.6}O_{1.8}$	$Y_2Zr_2O_7$
R Factor	22.14	18.50	19.07	26.01
Fit Index	0.00026	0.00016	0.00019	0.00035
N1 (O)	7.6	7.5	7.5	6.5
R1 (O)	2.315	2.310	2.308	2.294
A1 (O)	0.017	0.017	0.019	0.019
R2 (Zr)	3.644	3.637	3.663	3.667
A2 (Zr)	0.008	0.012	0.008	0.010
R3 (Y)	3.531	3.543	3.557	3.547
A3 (Y)	0.001	0.005	0.006	0.010

The dopant shell Debye Waller Factor (A3) is very low in some of these refinement, this is not considered to be greatly significant, as it occurs in samples with very low levels of the dopant, so a low A3 could be expected.

The fact that the fit for $Y_2Zr_2O_7$ is not as good as the others is not considered significant, as the data was considerably noisier.

Single Cluster Zirconium Work

As with the data from the yttrium edge, these are also very ‘good’ refinements, with low R factors and Fit Indices. Again, most of the difference between theoretical and experimental patterns is due to the presence of early electron density in the Fourier Transform. However, the fits are not quite as good as those from the yttrium edge. This is probably due to the same cause as the smaller amplitude of the EXAFS that was noted earlier. The cause of this is still not known.

Table 4.4 – Single Cluster Zirconium Data

	$\text{Y}_{0.15}\text{Zr}_{0.85}\text{O}_{1.925}$	$\text{Y}_{0.18}\text{Zr}_{0.82}\text{O}_{1.91}$	$\text{Y}_{0.4}\text{Zr}_{0.6}\text{O}_{1.8}$	$\text{Y}_2\text{Zr}_2\text{O}_7$
R Factor	23.00	22.06	27.03	33.79
Fit Index	0.00040	0.00042	0.00069	0.00109
N1 (O)	6.5	6.3	6.5	7.0
R1 (O)	2.141	2.142	2.154	2.132
A1 (O)	0.021	0.018	0.018	0.019
R2 (Zr)	3.584	3.565	3.650	3.635
A2 (Zr)	0.021	0.022	0.019	0.033
R3 (Y)	3.307	3.317	3.536	3.536
A3 (Y)	0.024	0.028	0.012	0.020

On the subject of the location of the vacancies, in this case the oxygen co-ordination numbers are considerably lower than those for the corresponding yttrium edge. The exception to this is $\text{Y}_2\text{Zr}_2\text{O}_7$ where the co-ordination number is actually higher on the zirconium edge. As mentioned, due to the equal mixing of yttrium and

zirconium by this stage of the phase diagram, this is expected and probably indicates a system where the vacancies are in fact evenly distributed between the two ions.

There are a few peculiarities in the data. Firstly, the Y–Zr distance from the yttrium edge refinement does not even closely match the Zr–Y distance from this one. There is also a discontinuity in the metal shell distances, with two distinct regions appearing to form.

Owing to the peculiarities in this data, further refinements on the data were performed, using multi cluster and dual edge techniques to get better consistency between the different fits.

Multi Cluster Yttrium Work

The co-ordination numbers from the single edge work are obviously merely representative. A real site must have an integer co-ordination number, and a non integer co-ordination number is an indication that at least two different sites are present in the system. Thus, this data was refined using two different clusters, one of six-fold and one of an eight-fold oxygen co-ordination. These were scaled as indicated in the Table 4.5. The scale factors were based on the high N1 in the single cluster refinements, which fell for $Y_2Zr_2O_7$.

Table 4.5 – Multi Cluster Yttrium Data

	$Y_{0.15}Zr_{0.85}O_{1.925}$		$Y_{0.18}Zr_{0.82}O_{1.91}$		$Y_{0.4}Zr_{0.6}O_{1.8}$		$Y_2Zr_2O_7$	
R Factor	22.42		19.11		18.87		29.29	
Fit Index	0.00029		0.00018		0.00020		0.00041	
N1 (O)	8	6	8	6	8	6	8	6
Scale Factor	75%	25%	75%	25%	75%	25%	50%	50%
R1 (O)	2.319	2.229	2.310	2.217	2.342	2.259	2.326	2.205
A1 (O)	0.013	0.016	0.013	0.010	0.015	0.008	0.011	0.012
R2 (Zr)	3.640	3.533	3.635	3.532	3.674	3.547	3.684	3.555
A2 (Zr)	0.009	0.005	0.009	0.006	0.008	0.004	0.019	0.006
R3 (Y)	3.620	3.622	3.593	3.587	3.591	3.626	3.503	3.583
A3 (Y)	0.016	0.016	0.019	0.020	0.010	0.015	0.013	0.005

The refinements on the first two samples, low yttria, are no better than those in the single cluster work presented earlier. Some small improvement in the fit index could have been expected if only from the number of new parameters in the system, but it is not apparent. However, the refinements for the second two samples is improved considerably.

There are some oddities in the third shell in the two low yttrium samples, with both the R3s and the A3s appearing to be correlated in some way. This is possibly due to the small number of atoms refined on each shell.

Multi Cluster Zirconium Work

Scale Factors in this data were reversed from the yttrium edge, as shown in Table 4.6, due to the generally low N1 in the single edge data, which rose for $Y_2Zr_2O_7$.

Table 4.6 – Multi Cluster Zirconium Data

	$Y_{0.15}Zr_{0.85}O_{1.925}$		$Y_{0.18}Zr_{0.82}O_{1.91}$		$Y_{0.4}Zr_{0.6}O_{1.8}$		$Y_2Zr_2O_7$	
R Factor	21.79		19.78		26.69		32.24	
Fit Index	0.00034		0.00033		0.00053		0.00083	
N1 (O)	8	6	8	6	8	6	8	6
Scale Factor	25%	75%	25%	75%	25%	75%	50%	50%
R1 (O)	2.239	2.111	2.259	2.122	2.275	2.130	2.222	2.092
A1 (O)	0.021	0.010	0.011	0.010	0.009	0.009	0.016	0.007
R2 (Zr)	3.678	3.557	3.701	3.561	3.683	3.588	3.721	3.607
A2 (Zr)	0.022	0.015	0.020	0.015	0.007	0.019	0.014	0.014
R3 (Y)	3.652	3.296	3.686	3.381	3.5539	3.522	3.584	3.488
A3 (Y)	0.006	0.014	0.003	0.032	0.003	0.033	0.011	0.011

In this case all the fits are significantly better than in the single cluster work. There is also good differentiation between the two clusters in all the samples. This would indicate that the model of two different sites for zirconium is true throughout the system.

When taken together with the fact that the fit indexes do not improve for the yttrium data in the low yttrium samples, and in fact are possibly slightly worse, this

indicates that the vacancies are preferentially located around the zirconium. However, as the yttrium to zirconium ratio increases, some vacancies are forced to go NN to the dopant.

YSZ Dual-Edge Work

To further increase the reliability of the data it is possible to simultaneously refine both edges. The results from this are presented below.

Table 4.7 – Dual edge YSZ Data

	$\text{Y}_{0.15}\text{Zr}_{0.85}\text{O}_{1.925}$		$\text{Y}_{0.18}\text{Zr}_{0.82}\text{O}_{1.91}$		$\text{Y}_{0.4}\text{Zr}_{0.6}\text{O}_{1.8}$		$\text{Y}_2\text{Zr}_2\text{O}_7$	
R Factor	22.25		20.74		23.59		31.85	
Fit Index	0.00017		0.00011		0.00019		0.00027	
Edge	Y	Zr	Y	Zr	Y	Zr	Y	Zr
N1 (O)	8.0	6.6	8.0	6.5	7.6	6.0	7.4	7.2
R1 (O)	2.314	2.150	2.315	2.147	2.312	2.158	2.307	2.174
A1 (O)	0.018	0.022	0.018	0.018	0.018	0.018	0.022	0.021
R2 (Zr)	3.641	3.584	3.643	3.571	3.666	3.568	3.682	3.601
A2 (Zr)	0.009	0.021	0.011	0.023	0.010	0.017	0.013	0.026
R3 (Y)	3.585	3.641	3.548	3.643	3.535	3.666	3.567	3.682
A3 (Y)	0.001	0.022	0.004	0.027	0.008	0.019	0.011	0.027

Note – The rule $\text{Zr}(\text{R3}) = \text{Y}(\text{R2})$ is set for the whole table.

The first point to be made is an oddity in the program. In all cases the refinement of the second edge is not as good as is possible in a single edge refinement. The

program never seems to properly model the gap between the two fitted shells, leading to some loss in refinement quality. The first shell fits very well, and appears to be of the same ‘goodness’ as single edge fits. This is shown in Figure 4.11.

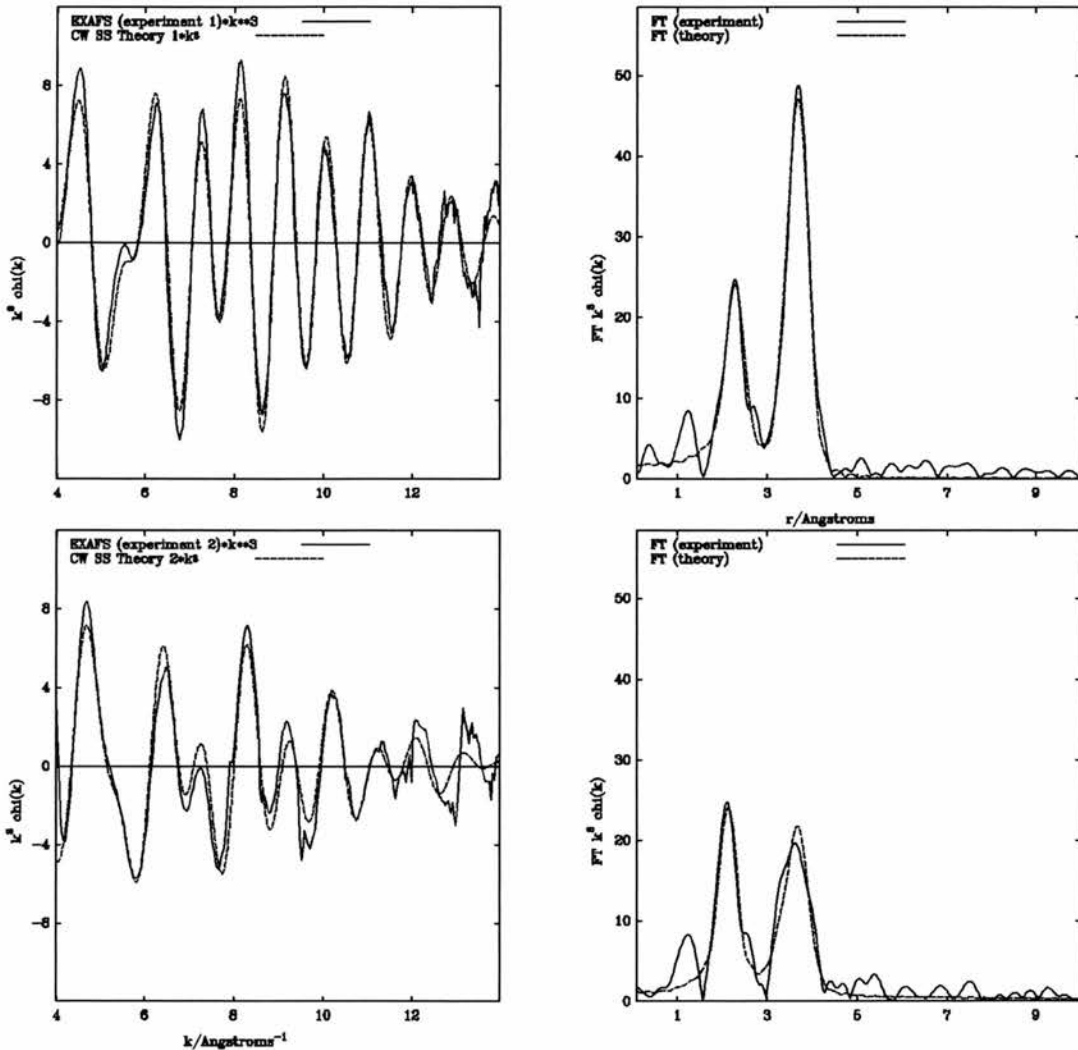


Figure 4.11 - Two edge refinement, with Zr data lower. Note the mismatch between the peaks on the second edge data.

To prevent the difference between the Y–Zr distance from the yttrium edge and the Zr–Y distance from the zirconium edge the two values were ruled to be the same.

All the fits are of a very high quality, with the Fit Indexes in particular being excellent. This is due to the increase in the ratio of data points to refined parameters, which improves the statistical fit.

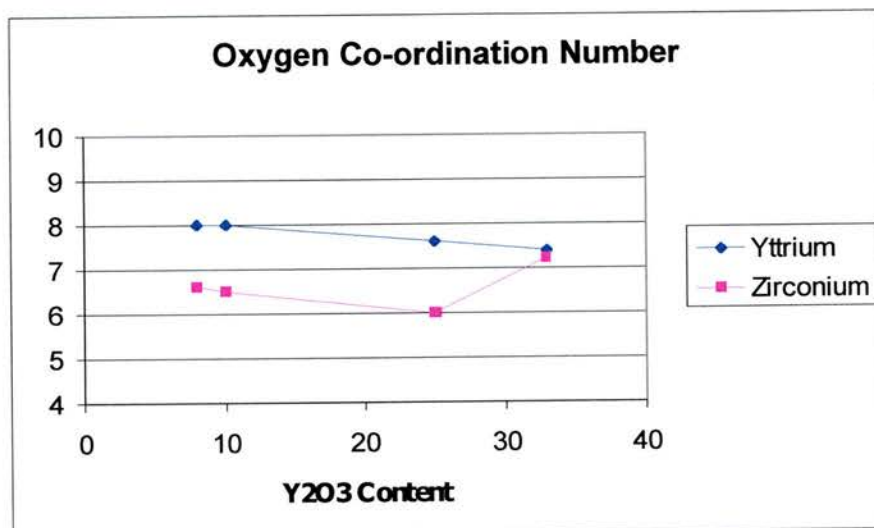


Figure 4.12 – Variation in Oxygen N for the two edges

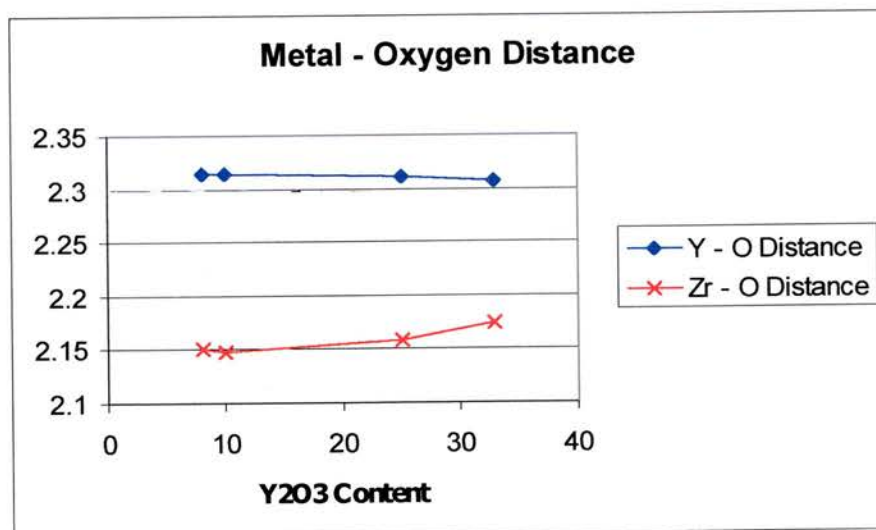


Figure 4.13 – Variation in R1 for the two edges

The main point to be drawn from the data is the behaviour of the oxygen shell, as shown in Figures 4.12 and 4.13. In low yttrium samples the co-ordination numbers are high on the yttrium edge and low on the zirconium edge, and they converge as the yttrium content increases and the vacancies become more metal independent. This is confirmed by the oxygen shell radii, which also converge.

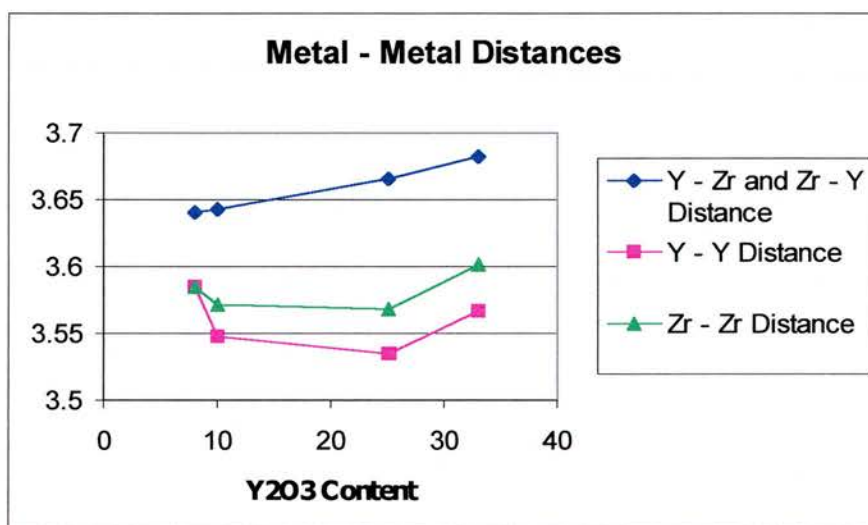


Figure 4.14 – Variation in the metal shells for the two edges

The metal shell behaviour is more peculiar, but is not considered greatly significant as there are not enough data points to extrapolate from..

While academically interesting, this model does not add in much that was not already seen earlier in the single cluster work. The metal radii are better fitted, but no new information is really presented.

YSZ Discussion

It seems clear that the vacancies are located preferentially NN to the zirconium ions. Vacancies are located NN to yttrium ions when in the higher yttrium samples, but this is due to statistical effects – it is difficult to get a site which is not NN to a yttrium when the sample is half yttrium.

The most interesting fits are the multi-cluster work. The improvement in the fits of all the zirconium edge samples and the two high yttria yttrium edge samples is marked, which shows there are at least two separate sites in these samples.

It is possible that this is due to the clustering of the vacancies into microdomains of an ordered subsystem. This would allow for the very different metal – metal radii seen in the refinements on the two different clusters.

Scandia Stabilised Zirconia

Single Cluster Zirconium Work

This data was analysed in the same manner as the YSZ data and is presented in Table 4.8 below.

These refinements were all stable and could be relied to converge to the same point. However, the data was all noisier than that presented earlier for YSZ. This has led to the lower quality of fits presented. Having said that, all the numbers are chemically reasonable and are considered valid. The fit from Sc7 is a lot worse than the others due to a spike in the data that was not easily removable.

Table 4.8 – Single Cluster Zirconium Data

	Sc7	Sc8	Sc9	Sc10	Sc11	Sc12	Sc13	Sc14
R Factor	38.64	30.01	33.02	32.53	30.85	30.57	29.25	28.09
Fit Index	0.00130	0.00077	0.00089	0.00088	0.00088	0.00079	0.00073	0.00073
N1 (O)	6.5	5.2	5.7	5.8	5.4	6	6.1	5.5
R1 (O)	2.119	2.121	2.127	2.128	2.126	2.128	2.133	2.142
A1 (O)	0.023	0.021	0.020	0.021	0.019	0.019	0.018	0.019
R2 (Zr)	3.567	3.554	3.545	3.545	3.455	3.460	3.473	3.499
A2 (Zr)	0.021	0.024	0.025	0.024	0.029	0.030	0.031	0.027
R3 (Sc)	3.579	3.540	3.526	3.528	3.418	3.415	3.423	3.470
A3 (SC)	0.008	0.012	0.012	0.016	0.006	0.007	0.008	0.014

Notes – Samples are labelled by the percentage of Sc₂O₃, thus Sc7 is (Sc₂O₃).07(ZrO₂).93.

The oxygen co-ordination numbers are highly volatile across the system, as shown in Figure 4.15, but are generally quite low, indicating that vacancies can be found NN to the zirconium in this system. The scatter is possibly beyond the errors, although errors on the co-ordination number are very difficult to evaluate, as mentioned in the experimental. The errors in this case are estimated as about +/- 1.

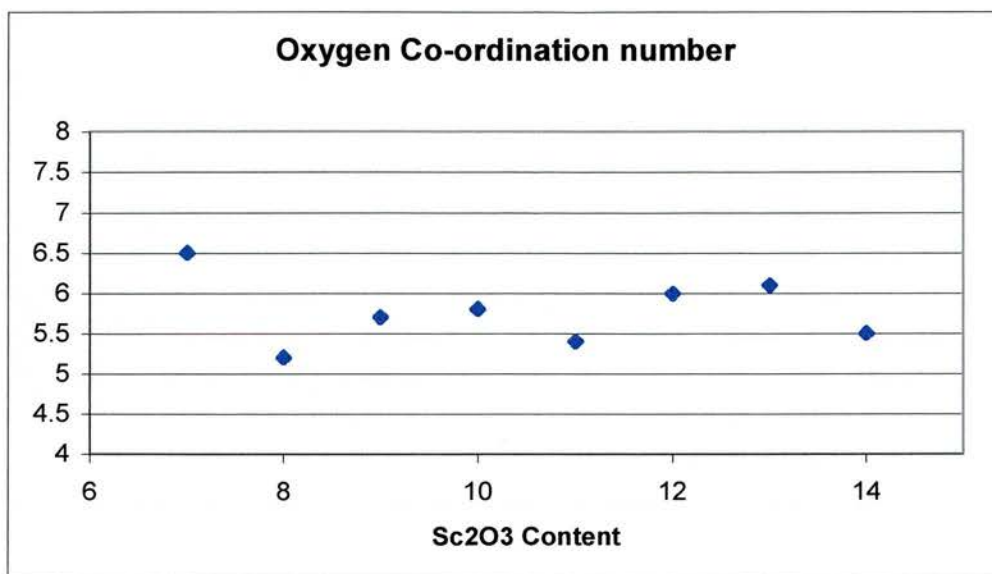


Figure 4.15 – Graph of the number of oxygens around each zirconium in ScSZ

As with the oxygen co-ordination number, the ZR-O distance shown in Figure 4.16 is very short, indicating that many of the zirconium sites are in six fold rather than eight fold sites. Interestingly, the radius of this shell actually increases across the composition range, even though it might have been expected to fall, as the decrease in oxygen would allow the ions closer to the central atom, due to a reduction in packing effects.

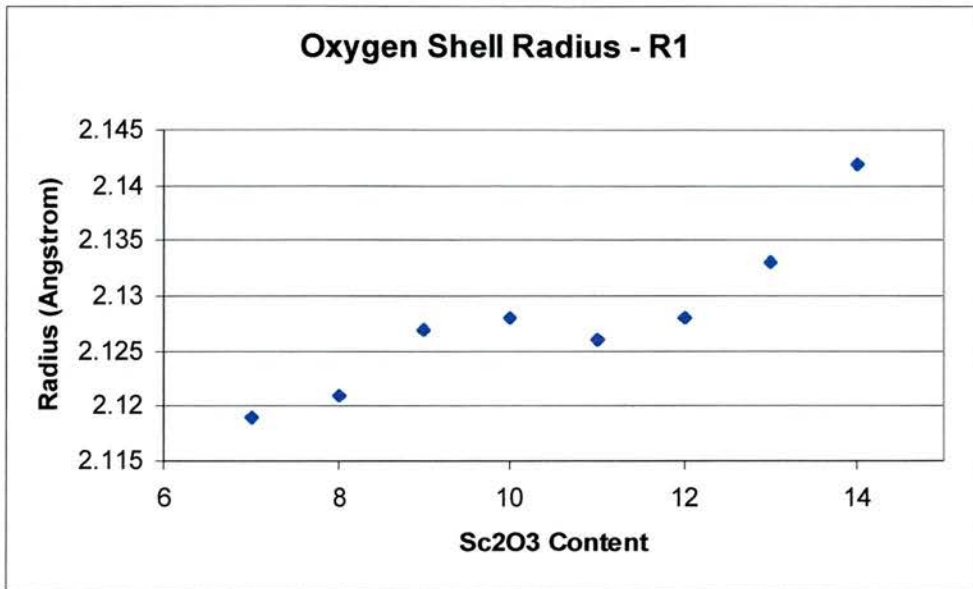


Figure 4.16 – Graph of the oxygen shell radii across the solid solution

Most interesting is the behaviour of the metal shell which shows an extremely sharp discontinuity between Sc10 and Sc11. This could indicate a phase change where none has previously been reported.

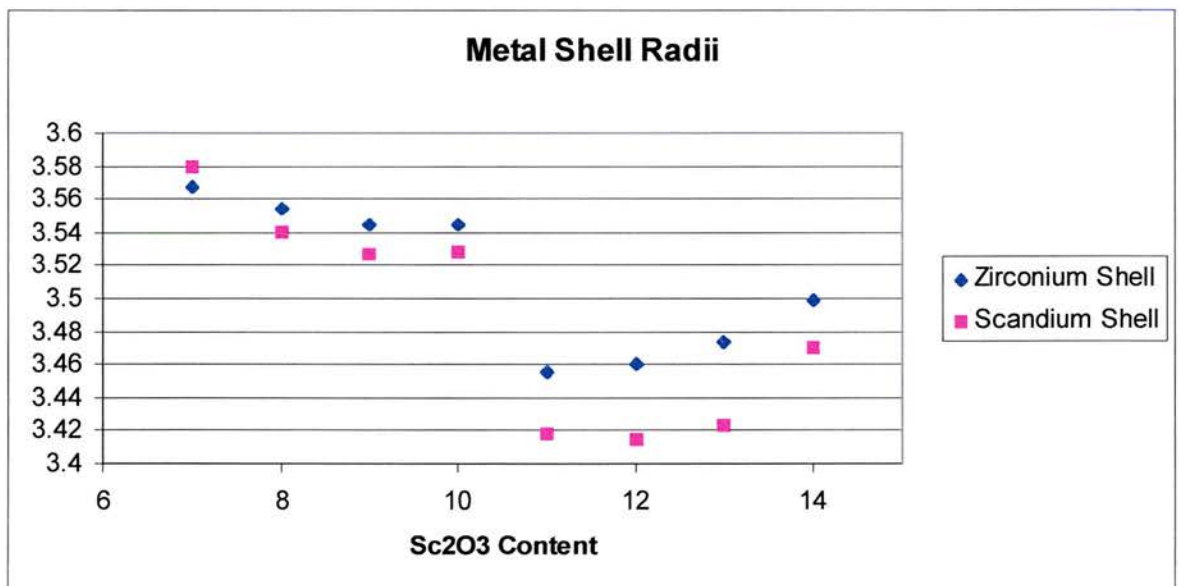


Figure 4.17 – Graph of the metal shell radii

Single Cluster Scandium Work

This data was far harder to refine than any presented before. Problems were caused by the noise on the data, which made it difficult to subtract the background accurately. With background subtractions of dubious quality, refinement can be very difficult. All the background subtractions for this data were considered reasonable, although several false starts were encountered on the way.

Table 4.9 – Single Cluster Scandium Data

	Sc9	Sc11	Sc12.5 (cu-Sc₂Zr₇O₁₇)	Sc14
K_{max}	10	9	8	8
R Factor	26.25	45.84	48.11	32.31
Fit Index	0.00067	0.00272	0.00388	0.00146
N1 (O)	4.8	5.1	4.6	5.4
R1 (O)	2.131	2.129	2.128	2.117
A1 (O)	0.015	0.017	0.033	0.020
R2 (Zr)	3.504	3.476	3.583	3.461
A2 (Zr)	0.024	0.022	0.031	0.028
R3 (Sc)	3.524	3.444	3.616	3.437
A3 (SC)	0.015	0.013	0.011	0.024

As can be seen, the quality of the data does vary greatly. This is all due to noise in the system. Having said that, there is still good data to be had, as all refinements are considered to be reasonable. This is shown in Figure 4.18.

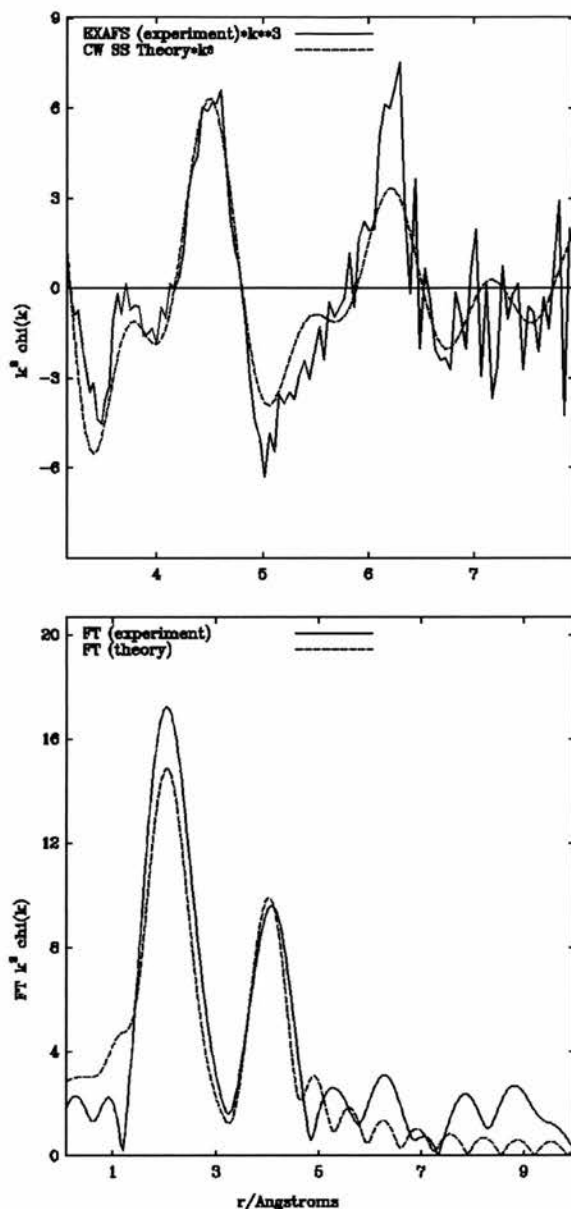


Figure 4.18 – Very noisy data on $\text{Sc}_2\text{Zr}_7\text{O}_{17}$

In all cases the oxygen co-ordination number has fallen to very low levels. This, along with the data from the zirconium edge would seem to indicate that the vacancies are metal independent. If there is a preference, it is probably for the scandium, as that is where the lower oxygen co-ordination numbers are seen.

The $\text{Sc}_2\text{Zr}_{17}\text{O}_{17}$ sample presented was from the high temperature cubic phase, as were the others, yet it still does not seem to be from the same series as the others. This could be due to some residual low temperature structure present, although none was apparent by XRD.

Multi Cluster Zirconium Work

For the fitting of two clusters, the refinement was scaled to be 75% the central zirconium ions being in six fold co-ordination sites and 25% to be in eight fold co-ordination sites. This was chosen due to the generally low N1 from the single cluster work.

Table 4.10a – Multi Cluster Zirconium Data

	Sc7		Sc8		Sc9		Sc10	
R Factor	31.27		23.77		25.85		25.45	
Fit Index	0.00098		0.00065		0.00068		0.00067	
N1 (O)	6	8	6	8	6	8	6	8
R1 (O)	2.116	2.298	2.128	2.315	2.124	2.294	2.125	2.296
A1 (O)	0.009	0.005	0.014	0.013	0.011	0.007	0.011	0.007
R2 (Zr)	3.602	3.773	3.598	3.780	3.590	3.768	3.590	3.767
A2 (Zr)	0.016	0.013	0.019	0.018	0.016	0.012	0.016	0.012
R3 (Sc)	3.648	3.721	3.615	3.736	3.617	3.711	3.616	3.711
A3 (SC)	0.021	0.013	0.029	0.032	0.023	0.014	0.022	0.014

The quality of the refinements has improved considerably, as was the case for multi cluster refinement on the zirconium edge in YSZ. This is shown in Tables 4.10a and b, split for ease of reading. Thus, similar conclusions are drawn. The improvement is due to the fact that this is a better model, that there are at least two different co-ordination environments seen in Zr in this system.

Table 4.10b – Multi Cluster Zirconium Data

	Sc11		Sc12		Sc13		Sc14	
R Factor	25.37		24.90		24.1		20.17	
Fit Index	0.00069		0.00064		0.00059		0.0004	
N1 (O)	6	8	6	8	6	8	6	8
R1 (O)	2.128	2.290	2.123	2.284	2.128	2.283	2.138	2.308
A1 (O)	0.014	0.016	0.010	0.007	0.009	0.007	0.009	0.006
R2 (Zr)	3.547	3.746	3.545	3.741	3.563	3.763	3.553	3.747
A2 (Zr)	0.019	0.017	0.020	0.017	0.020	0.016	0.021	0.018
R3 (Sc)	3.578	3.579	3.565	3.651	3.616	3.610	3.555	3.659
A3 (SC)	0.019	0.020	0.024	0.023	0.030	0.030	0.027	0.027

The data is still split into two definite regimes. The first four samples were all refined on a model from the refinement of Sc10 (simply the first performed). However, the last four could not be refined on this model at all. The refinement would go haywire if this were tried, with spiralling Debye Waller factors or ridiculous radii if they were tried. However, all of these were refined easily on a model based on Sc11.

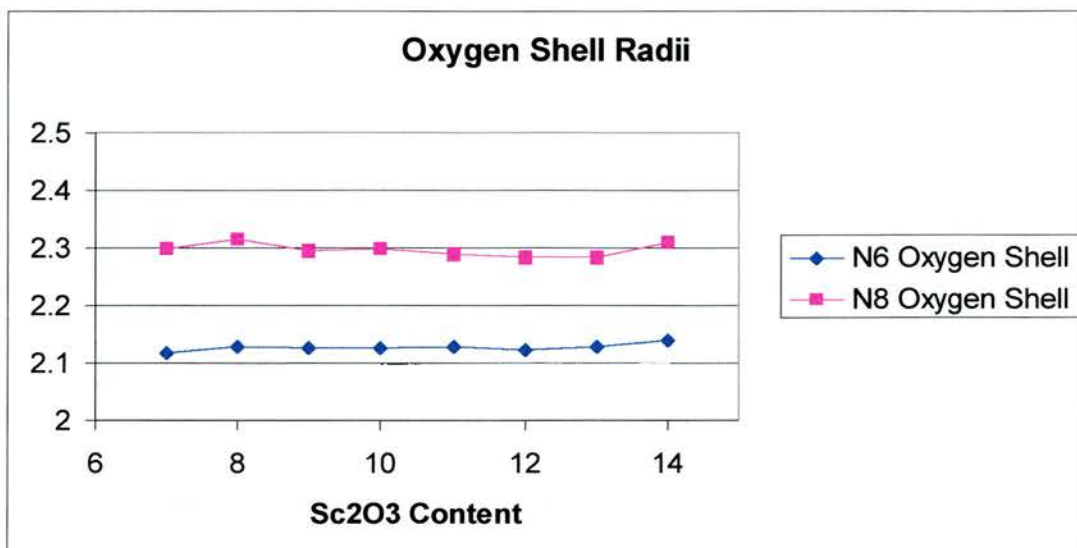


Figure 4.19 – Graph of the oxygen shell radii in each cluster

As shown in Figure 4.19, the oxygen shell radii are generally stable across the system in both shells.

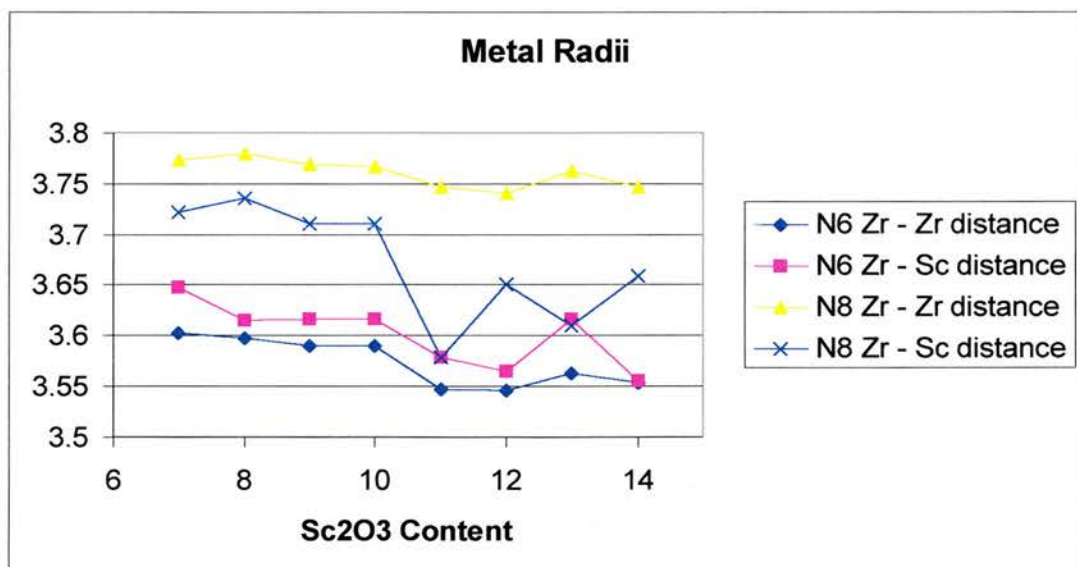


Figure 4.20 – Graph of the various metal shell radii in each cluster

Most interesting is the behaviour of the metal shells, as shown in Figure 4.20. The radii are stable in the first four (Sc7 – Sc10) refinements, after which there are significant changes. This was also observed phenomenologically in the refinement process, where the first four refinements were all easily performed on the same model, whereas the next four were much more difficult and required a different starting model. This would seem to point to some sort of phase change in the system.

Unfortunately, the scandium edge data was not considered to be of sufficient quality to perform a similar set of refinements on, so there is no second data set to compare this to.

ScSZ Discussion

This work provides an interesting counterpoint to the YSZ work. Both the metals appear have oxygen shells with co-ordination numbers of less than eight. This is confirmed in the graph of the Zr-O distance in YSZ and ScSZ, shown in Figure 4.21, which show it to be lower in ScSZ.

This cannot be so in the fluorite structure as there are only a limited number of vacancies to go round. So, if both metals are heading towards lower co-ordination environments then it must be due to a shift towards a six fold structure, possibly rutile, on the short range, while the long range remains cubic.

Structures in solids can be predicted using the radius ratio rules,²⁴ which can predict the energetically favourable packing of cations and anions. These rules have

predicted that the fluorite structure will be adopted in MX_2 compounds with a R_M / R_X ratio of greater than 0.732, and less than this the structure will be rutile. As described in the introduction, zirconia actually breaches these rules, so a move towards some kind of rutile structure on the short range, particularly with a similarly sized dopant like scandium, is not unreasonable to suggest. It is interesting to note that PbO_2 , which has a larger R_M / R_X than zirconia, adopts the rutile structure.²⁵

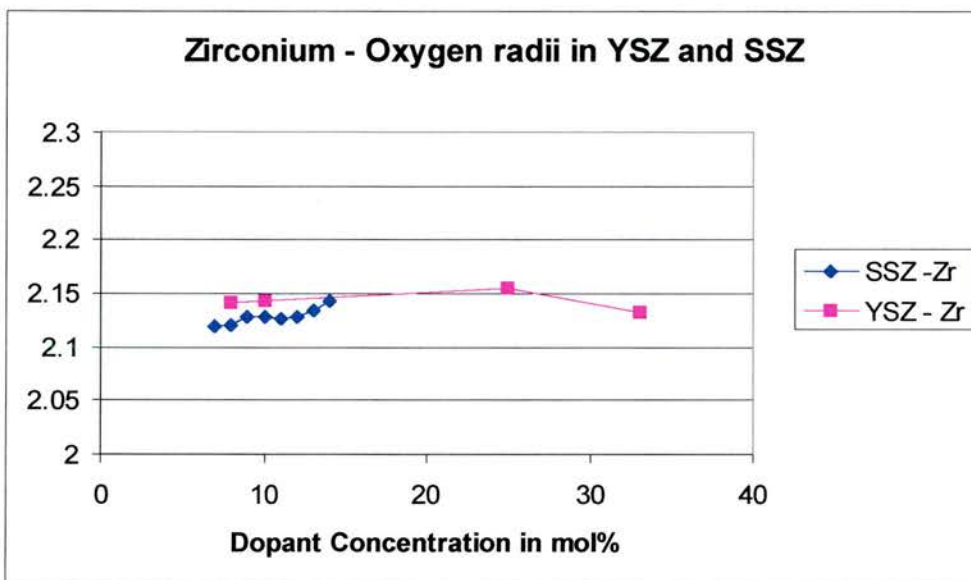


Figure 4.21 – Comparison graph of the zirconium – oxygen distances in YSZ and ScSZ

The change in the metal-metal radii seen half way through the series is interesting. The cause of this is not known with any certainty. Both sets of refinements are stable, returning to the presented data if initially set the other way. The only definite conclusion is that there is a change of some form in the metal shells between these two compositions. As no change is seen by diffraction methods here, a tentative suggestion of the cause is a phase change within the previously postulated microdomains. A consultation of the phase diagram, Figure 4.22, shows that the low temperature phase

changes from a mixture of monoclinic and fluorite to rhombohedral at a similar point, and the microdomains may behave similarly, while the bulk remains cubic.

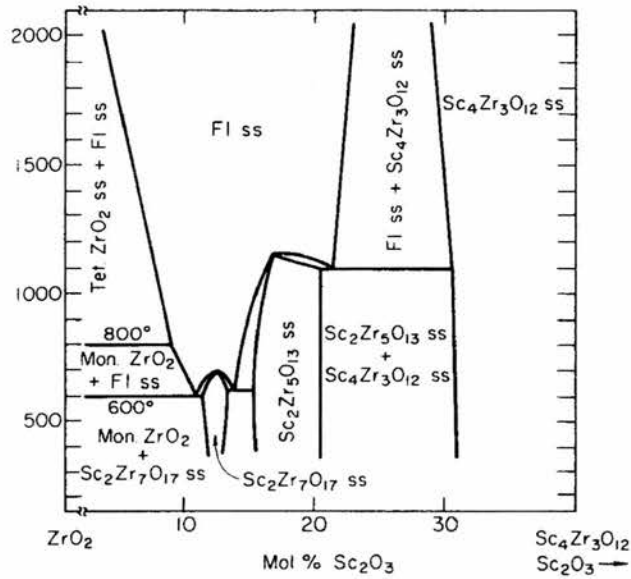


Figure 4.22 – Scandia-Zirconia phase diagram

Co-Doped Yttria Scandia Stabilised Zirconia

All compounds in this series were on the tie line $(\text{Sc}_2\text{O}_3)_x(\text{Y}_2\text{O}_3)_y(\text{ZrO}_2)_{0.9}$. Thus the overall dopant level was always ten mole percent.

In all cases, and on all metal edges, this data proved difficult to refine using three different shells for the metals. The problem of three overlapping shells always caused the program to try to assign some shells to electron density further out in the Fourier transform, too far to be chemically feasible. If this was prevented, other errors would creep in, such as spiralling Debye Waller factors. Due to this, all refinements were performed using only two shells, a first of oxygen and a second of a mixed site,

which was made of all three metals in their correct ratios. This is obviously not ideal, but was deemed to be necessary.

Single Cluster Yttrium Work

Again, all refinements of this data are solid and reproducible. The data is also internally consistent and broadly similar across the entire range. Some of the fits are obviously better than others, this is due to noisy data. Given that the data was collected on the same beam time allocation for a similar period, this is a little strange, but is not considered too significant.

Table 4.11 – Single Cluster Yttrium Data

	10YSZ	S2Y8	S5Y5	S8Y2	10ScSZ
R Factor	19.22	30.50	18.20	28.33	Contains no
Fit Index	0.00018	0.00056	0.00023	0.00062	Yttrium
N1 (O)	7.4	7.8	7.8	7.7	-
R1 (O)	2.307	2.310	2.303	2.312	-
A1 (O)	0.017	0.020	0.018	0.017	-
R2 (m)	3.616	3.616	3.606	3.605	-
A2 (m)	0.015	0.015	0.015	0.014	-

On the specifics, the oxygen co-ordination number is relatively high across the entire series, indicating that, as in YSZ, vacancies do not favour the yttrium NN sites. The first shell radii are equivalent with the value from the single shell 10YSZ fit (2.310 angstroms), further indication that yttrium is fully co-ordinated.

The slight contraction in the metal shell radius is as expected for the exchange of a smaller scandium for a larger yttrium ion.

The fact that the 10YSZ fit is different to the one in the single edge YSZ section can be attributed to the differences in the metal shell. Interestingly, the S5Y5 fit is excellent, something which is not matched on the zirconium edge data that was collected on the same scan.

Single Cluster Zirconium Work

Table 4.12 – Single Cluster Zirconium Data

	10YSZ	S2Y8	S5Y5	S8Y2	10ScSZ
R Factor	25.08	30.72	29.07	28.70	32.04
Fit Index	0.00053	0.00094	0.00078	0.00066	0.00098
N1 (O)	6.4	6.5	6.4	6.2	6.2
R1 (O)	2.147	2.143	2.145	2.140	2.135
A1 (O)	0.018	0.020	0.020	0.020	0.022
R2 (m)	3.567	3.561	3.560	3.547	3.548
A2 (m)	0.024	0.024	0.024	0.025	0.025

As in the data from the YSZ samples, the oxygen co-ordination numbers are much lower than those in the yttrium edge data, indicating that the vacancies are preferentially located here.

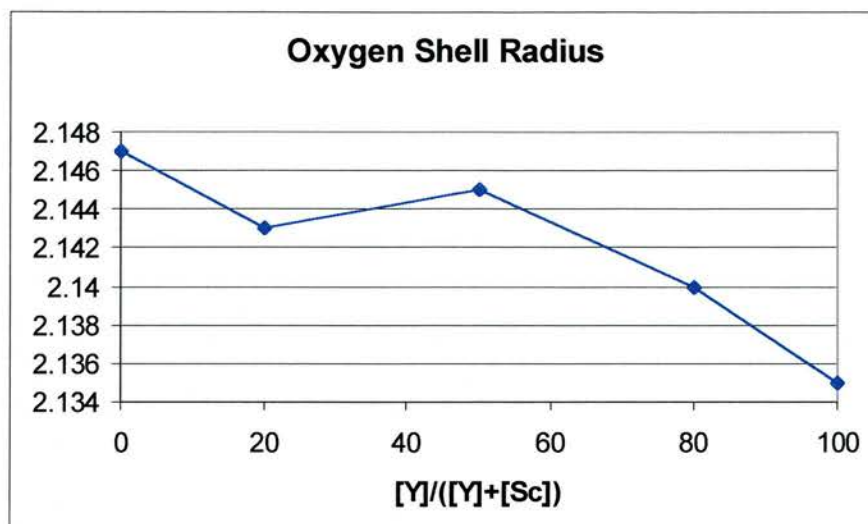


Figure 4.23 – R1 for the Zirconium edge

As opposed to the other two edges in the system, R1 contracts across the series for the zirconium edge, as the amount of scandium increases, as shown in Figure 4.23. This, along with the general trend in N1 indicates a movement towards a lower coordinated site for the zirconium as the amount of scandium increases and the amount of yttrium decreases. This could mirror the postulated change to a six fold co-ordination environment in ScSZ.

The data are all internally consistent, with the only obvious change being a contraction of the Zr–O distance on the last, yttrium free, sample. This matches data presented in the next chapter from Neutron diffraction work and the published work of Badwal,²⁶ who stated that only a small amount (ca 2%) of yttrium was required in the YScSZ to stabilise it into a YSZ-like phase. Again, the contraction in metal shell radii is as expected.

Single Cluster Scandium Work

Unfortunately, S8Y2 and Sc10 were not collected due to time constraints on the experiments at Daresbury. Sc9 has been substituted as a comparison, although it is obviously not a perfect situation.

All the data were extremely noisy and very difficult to background subtract. Surprisingly, once subtracted, the refinement was relatively well behaved and produced consistent results, within the limitations of the noisy data.

Table 4.13 – Single Cluster Scandium Data

	10YSZ	S2Y8	S5Y5	Sc9
R Factor	Contains no	46.57	39.00	28.09
Fit Index	Scandium	0.00341	0.00168	0.00093
N1 (O)	-	5.4	5.4	5.0
R1 (O)	-	2.149	2.136	2.145
A1 (O)	-	0.020	0.017	0.016
R2 (m)	-	3.533	3.513	3.515
A2 (m)	-	0.032	0.030	0.027

The oxygen co-ordination numbers are the lowest of all three metals, considerably below even those on the zirconium ion, possibly indicating that all scandium ions are in six fold sites. This is feasible even with N1 of roughly 5, as the numbers are probably being slightly depressed by sample effects, as discussed earlier,

and the fact that six is the lowest generally available co-ordination number in scandium systems.

Multi Cluster Yttrium Work

For the fitting of two clusters to the yttrium edge, the refinement was scaled to be 75% the central yttrium ions being in eight fold co-ordination sites and 25% to be in six fold co-ordination sites. This was chosen due to the generally high N1 from the single cluster work.

Table 4.14 – Multi Cluster Yttrium Data

	10YSZ		S2Y8		S5Y5		S8Y2		10ScSZ	
R Factor	18.70		27.43		17.12		27.89		Contains no	
Fit Index	0.00017		0.00049		0.0021		0.00061		Yttrium	
N1 (O)	6	8	6	8	6	8	6	8	-	-
R1 (O)	2.230	2.324	2.217	2.328	2.226	2.328	2.228	2.334	-	-
A1 (O)	0.010	0.014	0.008	0.014	0.007	0.015	0.010	0.013	-	-
R2 (m)	3.539	3.640	3.524	3.640	3.525	3.641	3.523	3.636	-	-
A2 (m)	0.007	0.011	0.006	0.010	0.004	0.010	0.004	0.009	-	-

In all three mixed metal refinements the fit has actually improved when applying two clusters to the data. This would seem to indicate that, unlike in the case of YSZ, the idea of two different yttrium sites is actually correct at this composition. Thus, it is likely that at least some yttrium ions are not in eight fold sites, even though statistically they could all be.

This contradicts the evidence of the single edge yttrium-oxygen distances (R1), which were the same in these samples and in 10YSZ, indicating a similar oxygen environment.

Multi Cluster Zirconium Work

In the case of zirconium, the refinement was scaled to be 75% the central zirconium ions being in six fold co-ordination sites and 25% to be in eight fold co-ordination sites, due to the generally low N1 from the single cluster work.

Table 4.15 – Multi Cluster Zirconium Data

	10YSZ		S2Y8		S5Y5		S8Y2		10ScSZ	
R Factor	20.44		23.9		23.20		24.87		28.12	
Fit Index	0.00042		0.00060		0.00054		0.00051		0.00074	
N1 (O)	6	8	6	8	6	8	6	8	6	8
R1 (O)	2.135	2.300	2.131	2.303	2.128	2.293	2.131	2.298	2.126	2.298
A1 (O)	0.007	0.004	0.007	0.004	0.008	0.005	0.009	0.007	0.011	0.006
R2 (m)	3.584	3.763	3.574	3.758	3.570	3.751	3.571	3.759	3.574	3.761
A2 (m)	0.019	0.028	0.018	0.026	0.017	0.025	0.018	0.018	0.017	0.015

In this case, similarly to YSZ, the fit has improved with two clusters over the single cluster case. Thus, similar conclusions can be drawn, that this is a more accurate picture of the system than a single cluster model.

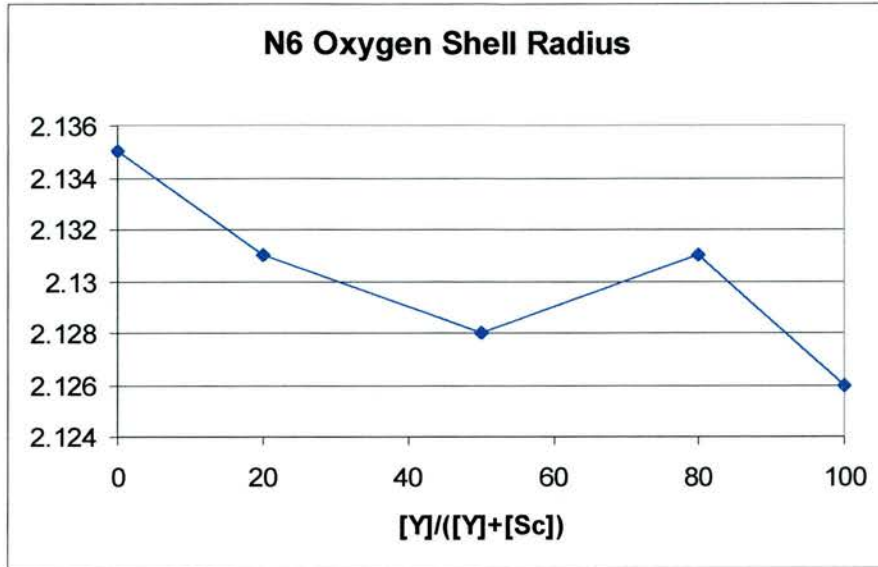


Figure 4.24 – R1 for the zirconium edge N6 cluster

Looking at the behaviour of the zirconium – oxygen distances, the distance decreases in the N6 cluster. The distance does not seem to change linearly in the N8 cluster, but is tending to decrease also.

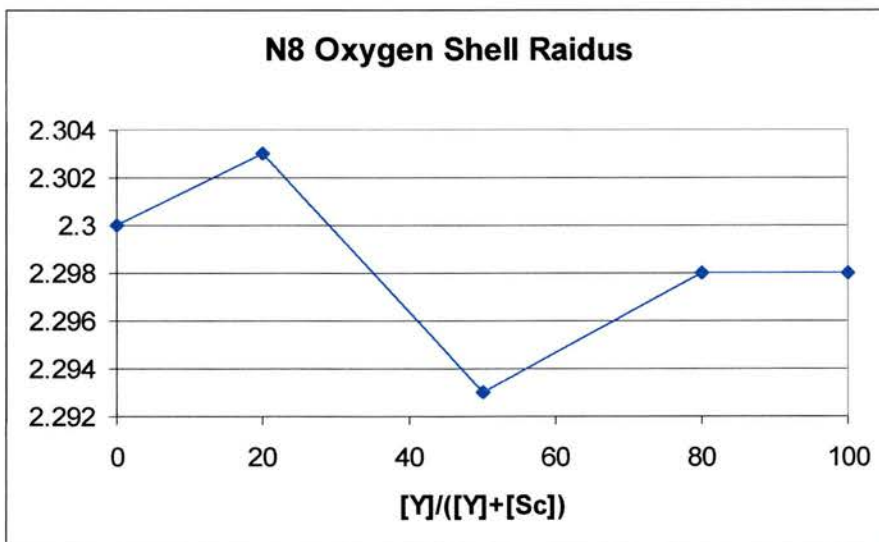


Figure 4.25 – R1 for the zirconium edge N8 cluster

YScSZ Discussion

These refinements show a system which is a transition between the two previous systems of YSZ and ScSZ. In particular, the zirconium data shows a definite transition over the range in the case of its R1 distances as it accommodates the change between the two systems. The transition between the two systems can be seen in the neutron diffraction data presented in the next chapter.

Again, the multi-cluster refinements are pointing to several different sites for the zirconium, with different metal clusters around them, evidence for a microdomain rather than a defect fluorite picture of the system. As this is also true on the yttrium edge, it appears that these microdomains are not element specific.

Discussion and Conclusions

The YSZ results echo the already overwhelming experimental evidence, but take it further. Yttria stabilised zirconia has traditionally been viewed as a defect fluorite type structure. More recent work has shown evidence of microdomains of ordered phases, embedded in an overall fluorite matrix. It is generally agreed that the concept of perfect disorder in this system is not entirely correct, and some form of ordering of vacancies takes place. It is the exact nature of this ordering which is in question.

The results from the two cluster work on YSZ suggest that the zirconium does indeed have two different environments, but that the yttrium probably does not until it is forced to. The yttria environment is almost certainly that of an eight-fold co-ordination

to oxygen - full co-ordination in a dilute solution. The great difference in the metal shells in these refinements indicates that the local structure is not a simple defect fluorite but something else, probably some form of microdomain.

This is contrasted when some amount of scandium is added, with the multi-cluster approach showing improvement in the quality of fit on both yttrium and scandium edges. This could well indicate a different form of vacancy clustering in YScSZ.

The ScSZ samples show the vacancies to be almost metal independent. The fact that the average co-ordination number falls NN to both atoms is very interesting, as this is not possible in an eight fold co-ordination system like the fluorite structure. It seems to indicate a move to a MX_6 system, such as the rutile structure. This is a possibility for the structure of the microdomains. These samples also show an interesting change between SC10 and SC11, which correspond to the two highest conducting and most stable compositions. This is possibly due to a phase change to the ordered rhombohedral $Sc_2Zr_7O_{17}$ structure in the microdomains.

All three sets of data would seem to indicate an order of preference of the siting of vacancies, which is NN to first scandium, then zirconium, with yttrium preferring to remain fully co-ordinated if at all possible. This is similar to the predictions of Zacate *et. al.*¹³ who predicted that scandium would be the same as zirconium. The differences we find to this are only minor.

References

- 1 C. B. Choudhary, H. S. Maiti and E. C. Subbarao, in *Solid Electrolytes and Their Applications*, ed. E. C. Subbarao, Plenum Press, New York, 1980, p. 1.
- 2 C. R. A. Catlow, A. V. Chadwick, G. N. Greaves and L. M. Moroney, *J. Am. Ceram. Soc.*, 1986, **69**, 272.
- 3 M. H. Tuilier, J. Dexpwrt-Ghys, H. Dexpert and P. Lagarde, *J. Solid State Chem.*, 1987, **69**, 153.
- 4 A. I. Goldman, E. Canova, Y. H. Kao, W. L. Roth and R. Wang, *EXAFS and Near Edge Structure III*, K. O. Hodgson, B. Hedman and J. E. Penner-Hahn, Springer Verlag, New York, 1984, pg. 442.
- 5 H. Morikawa, Y. Shimizugawa, F. Marumo, T. Harasawa, H. Ikawa, K. Tohji and Y. Udagawa, *J. Jpn. Ceram. Soc.*, 1988, **96**, 253.
- 6 Z. J. Shen, T. K. Li, K. Q. Lu and Y. Q. Zhao, *J. Chin. Silic. Soc.* 1988, **16**, 270.
- 7 D. Komyoji, A. Yoshiasa, T. Moriga, S. Emura, F. Kanamaru and K. Koto, *Solid State Ionics*, 1992, **50**, 291.
- 8 B. W. Veal, A. G. McKale, A. P. Paulikas, S. J. Rothman and L. J. Nowicki, *Physica B*, 1988, **150**, 234.
- 9 P. Li, I-W. Chen and J. E. Penner-Hahn, *Phys. Rev. B*, 1993, **48**, 10063.
- 10 P. Li, I-W. Chen and J. E. Penner-Hahn, *Phys. Rev. B*, 1993, **48**, 10074.
- 11 P. Li, I-W. Chen and J. E. Penner-Hahn, *Phys. Rev. B*, 1993, **48**, 10082.
- 12 P. Li, I-W. Chen and J. E. Penner-Hahn, *J. Am. Ceram. Soc.*, 1994, **77**, 118.
- 13 M. O. Zacate, L. Minervini, D. J. Bradfield, R. W. Grimes and K. E. Sickafus, *Solid State Ionics*, 2000, **128**, 243.

-
- 14 W. Yuren, L. Kunquant, W. Dazhi, W. Zhonghua and F. Zhengzhi, *J. Phys.: Condens. Matter*, 1994, **6**, 633.
- 15 G. E. Rush, A. V. Chadwick, I. Kosacki and H. U. Anderson, *J. Phys. Chem. B*, 2000, **104**, 9597.
- 16 S. Yamazaki, T. Matsui, T. Ohashi and Y. Arita, *Solid State Ionics*, 2000, **136-137**, 913.
- 17 Taken from Daresbury EXAFS course 2000, notes from which are available at <http://srs.dl.ac.uk/xrs/>
- 18 J. J. Barton, Z. Hussain and D. A Shirley, *Phys. Rev. B*, 1987, **35**, 933.
- 19 B. J. Mitchell, *PhD Thesis*, University of St. Andrews, 1998.
- 20 M. Borowski, personal communication.
- 21 F. Mosselmans, personal communication.
- 22 M. Newville, P. Livins, Y. Yacoby, E. A. Stern, and J. J. Rehr, *Phys. Rev. B*, 1993, **47**, 14126.
- 23 J. Chaboy, A. Marcelli and T. A Tyson, *Phys. Rev. B*, 1994, **49**, 11652.
- 24 U. Muller, *Inorganic Structural Chemistry*, John Wiley and Sons, Chichester, 1993.
- 25 A. R. West, *Basic Solid State Chemistry*, John Wiley and Sons, Chichester, 1984.
- 26 S. P. S Badwal, F. T. Ciacchi, S. Rajendran and J. Drennan, *Solid State Ionics*, 1998, **109**, 167.

Neutron Diffraction Studies on Doped Zirconia

EXPERIMENTAL	171
RESULTS	173
DISCUSSION	182
REFERENCES	183

Scandia stabilised zirconia has long been known to have high oxide ion conductivity,¹ higher in fact than the 8 mol% YSZ used in many solid oxide fuel cell (SOFC) test systems. However, the more complex phase equilibria in this system, as shown in Figure 5.1, and the traditionally high price of scandia have for years prevented anything but small scale investigations. With various political issues resolved and more scandia coming to market, the price of this material has fallen considerably making it a feasible candidate for SOFC electrolytes and thus worthy of further study.

The problem of the complex phase assembly of scandia stabilised zirconia can be addressed in several ways. One of the most promising is to co-dope zirconia with both scandia and yttria. This has not been extensively studied, although initial work by Badwal *et. al.*² shows considerable promise. A small amount (ca 2 mol%) of yttria doped additionally into scandia zirconia will stabilise the desired fluorite phase down to room temperature. As can be seen from the phase diagram, illustrated in Figure 5.1, the fluorite phase is never thermodynamically stable at room temperature in the scandia-only system. Interestingly, reports have also indicated that the co-doped system is also mechanically tougher than either YSZ or ScSZ,³ which is a particularly useful attribute for devices manufactured from this ceramic. Doping scandia stabilised zirconia with yttria does reduce the oxide ion conductivity, but it is still higher than that of 8 mol% YSZ, and is the highest conducting composition in the YSZ family.

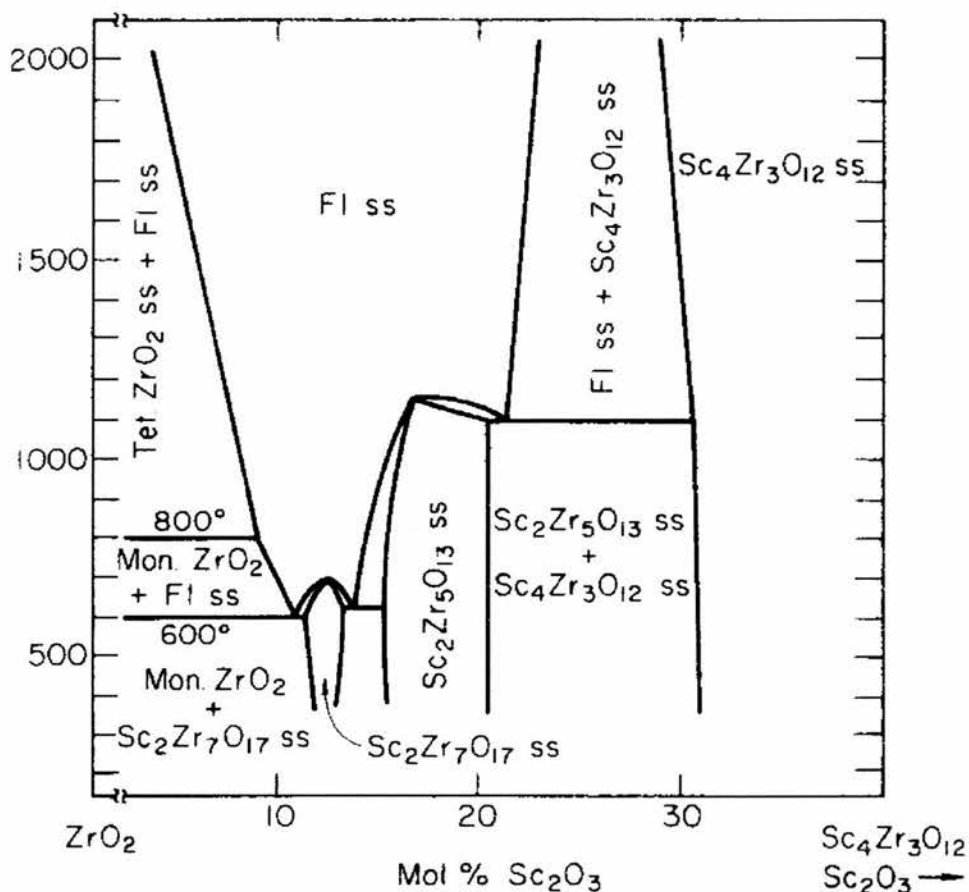


Figure 5.1 – Phase Diagram of the $\text{Sc}_2\text{O}_3\text{:ZrO}_2$ System

Experimental

A range of samples, as illustrated in the ternary system below, were prepared. The samples were concentrated in the high zirconia region of the diagram, as this is the technologically interesting part of the system. These compositions are those with the highest oxide ion conductivity.

Samples were all prepared as a series rather than as individual samples, to minimise the effects of any errors in sample processing. Two series were prepared,

$(\text{Sc}_2\text{O}_3)_{0.07}(\text{ZrO}_2)_{0.93}$ to $(\text{Sc}_2\text{O}_3)_{0.14}(\text{ZrO}_2)_{0.86}$ and $(\text{Sc}_2\text{O}_3)_{0.1}(\text{ZrO}_2)_{0.9}$ to $(\text{Y}_2\text{O}_3)_{0.1}(\text{ZrO}_2)_{0.9}$. In each case a large batch of each end member was weighed from dry oxides and ball-milled in a zirconia ball mill. The intermediate members of the series were prepared by mixing the correct proportions of each end member. (E.g. $(\text{Y}_2\text{O}_3)_{0.05}(\text{Sc}_2\text{O}_3)_{0.05}(\text{ZrO}_2)_{0.9}$ is made from a 50:50 mix of the two end members. Using this method, even if the initial calculations are inaccurate, it is known that the spacing between the samples is regular.) These mixtures were again ball-milled, then uni-axially pressed into pellets and fired in platinum crucibles. Platinum crucibles were used as they are far better conductors of heat than alumina and thus better for the quenching stage of preparation. All the firings were designed to stabilise the high temperature phases at room temperature by quenching them. The samples were placed in the furnace at 900°C and then ramped to 1500°C at $100^\circ\text{C}/\text{hr}$. They were fired at 1500°C for 48 hours before being cooled at $100^\circ\text{C}/\text{hr}$ to 900°C , from where they were quenched in air to room temperature. The phases $\text{Sc}_2\text{Zr}_5\text{O}_{17}$ and $\text{Sc}_2\text{Zr}_5\text{O}_{17}$ were both prepared in a similar manner from dry oxides.

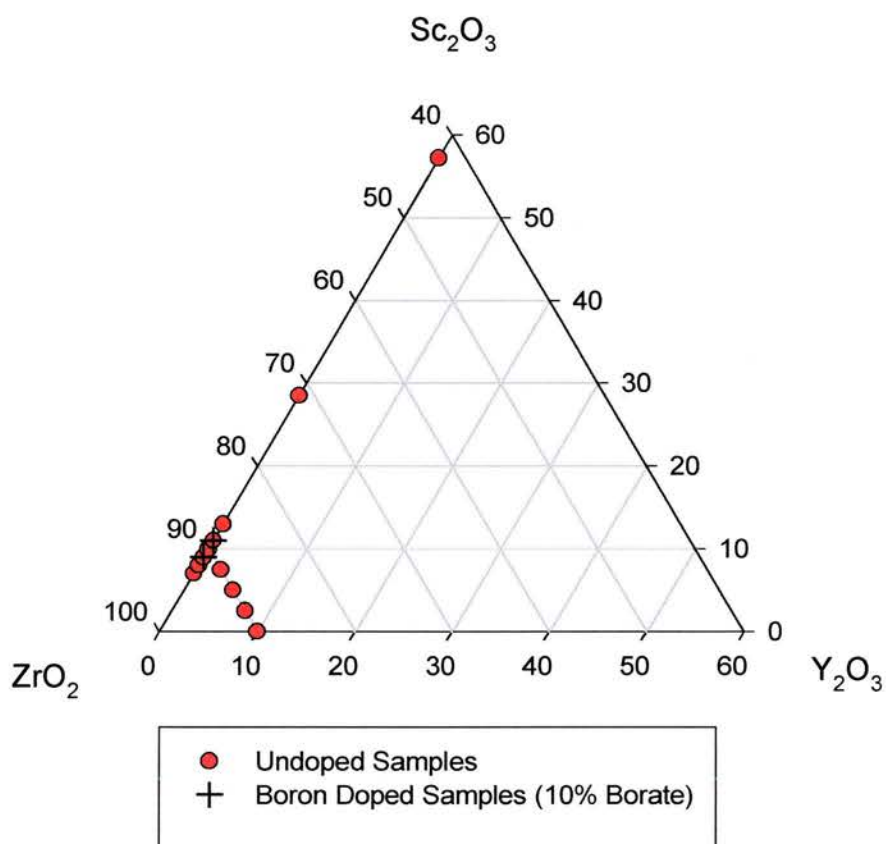


Figure 5.2 – Samples analysed at Studsvik

Results

The following diffraction data were collected on the instrument NPD at Studsvik at room temperature in runs averaging four hours. This was long enough to allow the maximum peak to reach ca. 10,000 counts. All data was refined using the FullPROF Rietveld refinement program.

The samples dealt with here are along the tie-line of $(Y_2O_3)_{0.1}(ZrO_2)_{0.9}$ to $(Sc_2O_3)_{0.075}(Y_2O_3)_{0.025}(ZrO_2)_{0.9}$ and $(Sc_2O_3)_{0.08}(ZrO_2)_{0.92}$. All of the refined samples are cubic and the basic statistics of their Rietveld refinements are presented in Table 5.1.

Table 5.1 – Collated Refinement Results

Sample	R-Factor	Cell Edge	Oxygen Biso	Cation Biso
$(Sc_2O_3)_{0.08}(ZrO_2)_{0.92}$	7.98	5.081	3.184	1.362
$(Sc_2O_3)_{0.075}(Y_2O_3)_{0.025}(ZrO_2)_{0.9}$	5.01	5.107	2.494	1.114
$(Sc_2O_3)_{0.05}(Y_2O_3)_{0.05}(ZrO_2)_{0.9}$	4.48	5.120	2.470	1.027
$(Sc_2O_3)_{0.025}(Y_2O_3)_{0.075}(ZrO_2)_{0.9}$	4.10	5.135	2.483	0.954
$(Y_2O_3)_{0.1}(ZrO_2)_{0.9}$	4.32	5.148	2.487	0.886

All of these refinements were performed in the same way, using the Gaussian peak shapes. Attempts to refine the peak shape using a Pseudo-Voigt peak shape were less successful.

A plot showing the results from a typical refinement is shown in Figure 5.3. As can be seen there is clearly a good fit to the cubic fluorite structure, although there does seem to be some structure in the background that is not being refined. This leads to a larger R-factor than ideal.

At this point it is instructive to consider previous studies of yttria stabilised zirconia. Similar diffuse background features were reported by Irvine and Gibson⁴ for 8 mol% Y_2O_3 92 mol% ZrO_2 . These diffuse features were lost on heating to above 650°C.

The diffuse features were attributed to short range order giving rise to a micro domain structure that was quite different to the average structure at lower temperatures.^{5,6} Not only did this microdomain structure manifest itself in a diffuse superstructure in the neutron diffraction pattern, it also affected the temperature factors of the anion sublattice. The ITFs for the oxygens were shown to consist of two components, a static one, (B_{static}) due to short range order and the normal temperature factor (B_{temp}) that grew to dominate at high temperatures.

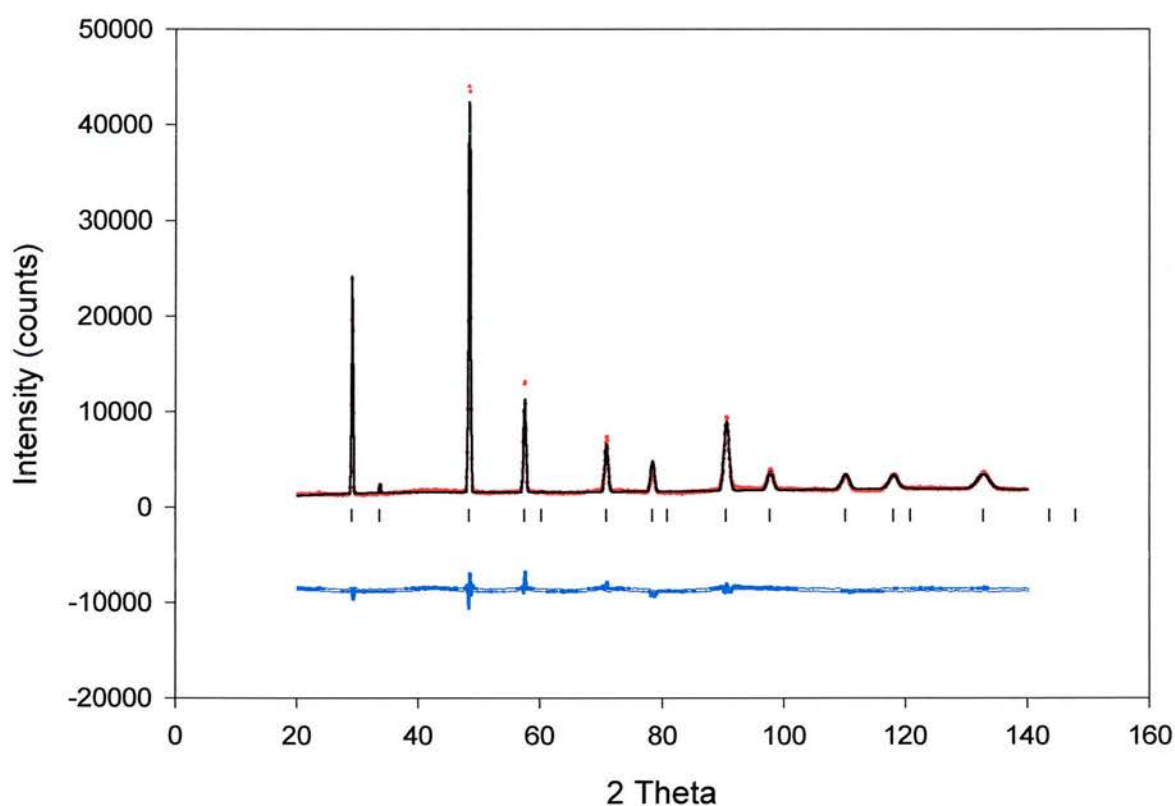


Figure 5.3 - Refined and observed diffraction data for $(\text{Sc}_2\text{O}_3)_{0.08}(\text{ZrO}_2)_{0.92}$

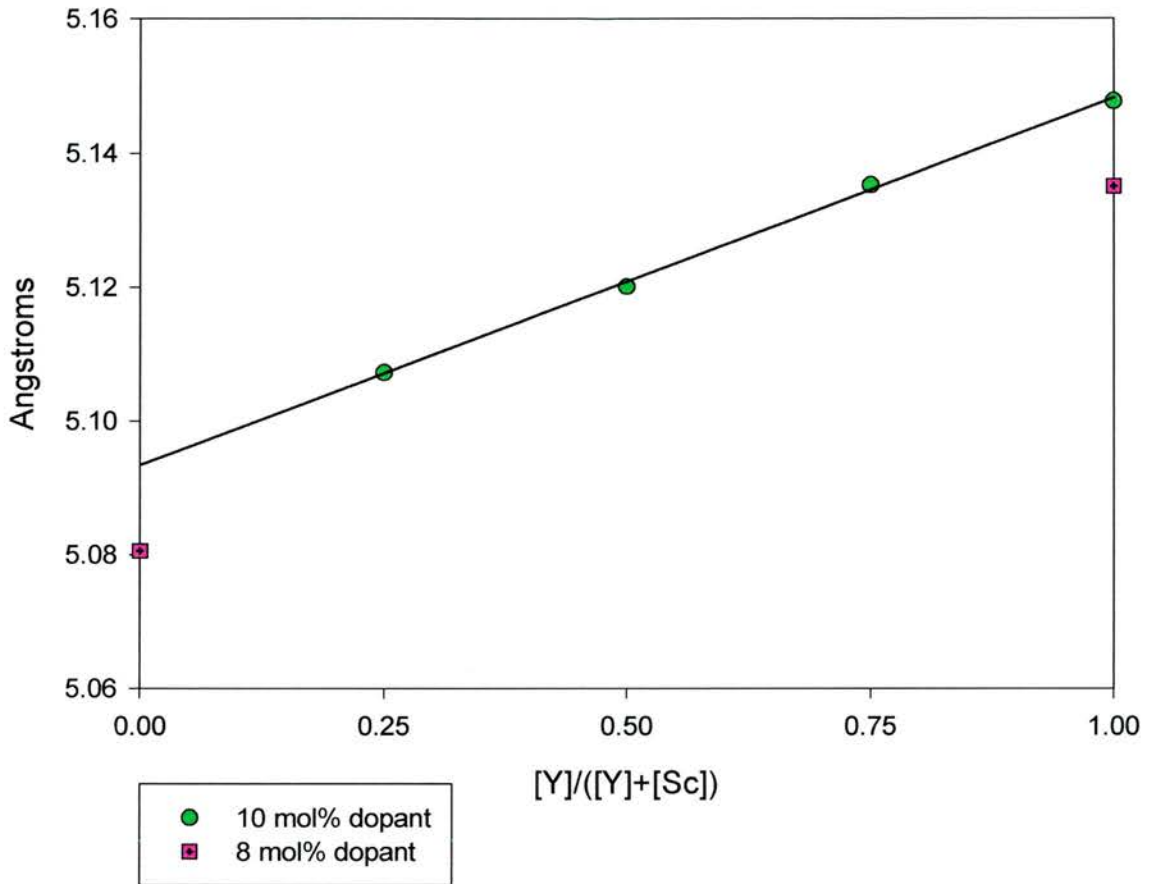


Figure 5.4 - Unit cell parameter as a function of composition

The unit cell dimensions follow the trend that we would expect, as shown in Figure 5.4. As scandium is smaller than yttrium we would predict that the unit cell would shrink linearly with falling yttria content, as seen in the neutron data. As can be seen from the linear fit of the 10 mol% data and the similar gap between it and the 8 mol% data these samples seem to follow Vegard's Law.

The 10 mol% Sc_2O_3 90 mol% ZrO_2 sample has not been fully refined as it is not single phase, thus the data is not presented.

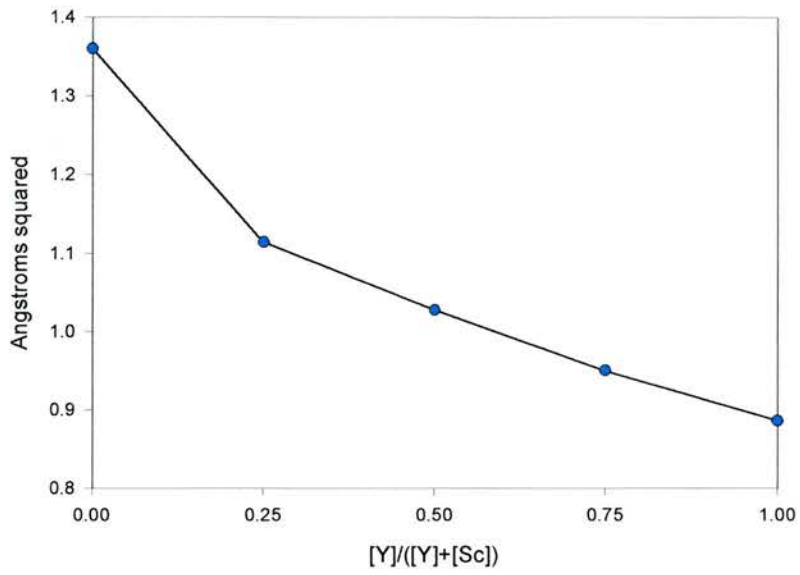


Figure 5.5 - Changes in cation B_{iso} with composition

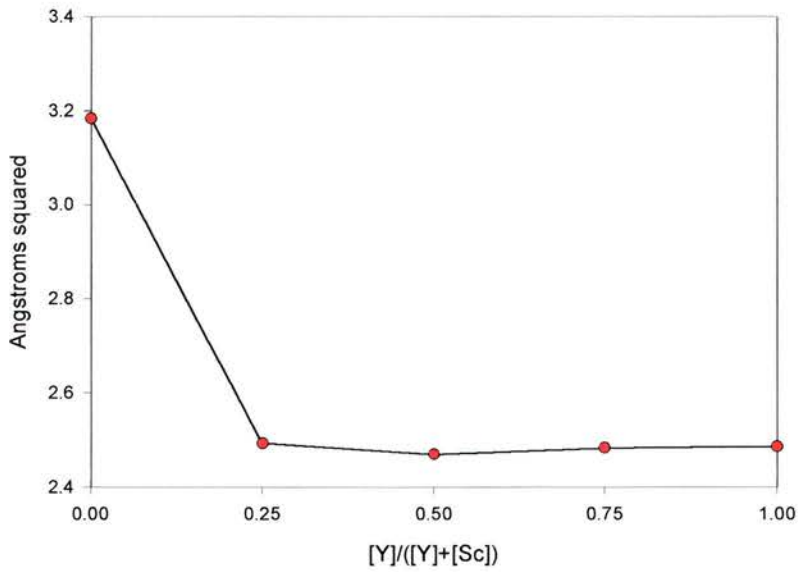


Figure 5.6 - Changes in oxygen B_{iso} with composition

The two graphs of the temperature factors in the system (Figures 5.5 and 5.6) tell a more interesting story. The cation temperature factors fall in an almost linear fashion with increasing yttria, while the oxygen temperature factors are almost identical, with the exception of the scandia only sample, which is considerably higher. It seems that in scandia substituted samples both cation and anion sub-lattices are significantly distorted from ideal in the microdomains whereas in the yttria-substituted sample it is the anion sub-lattice that is predominately affected. Addition of some yttria to the scandia substituted sample reduces the oxygen distortions significantly, apparently breaking some short range Sc-O clustering.

This stabilisation by a small amount of yttrium is supported by the paper of Badwal *et. al.*² who claim that even 2 mol% yttria in a similar system is enough to stabilise the cubic phase at room temperature, whereas the scandia-only system is only meta-stable.

The linear nature of the cation temperature factors seems to show that the Scandia, like Oxygen exhibits short range static displacements, whereas Yttrium exhibits little static disorder. This hypothesis could be tested by performing high temperature studies, as disorder would be anticipated at higher temperatures.

In the following figures diffraction patterns are presented from a range of compositions amplifying the intensity to demonstrate the modulation features in the baseline. The larger these features, the larger the R-factor.

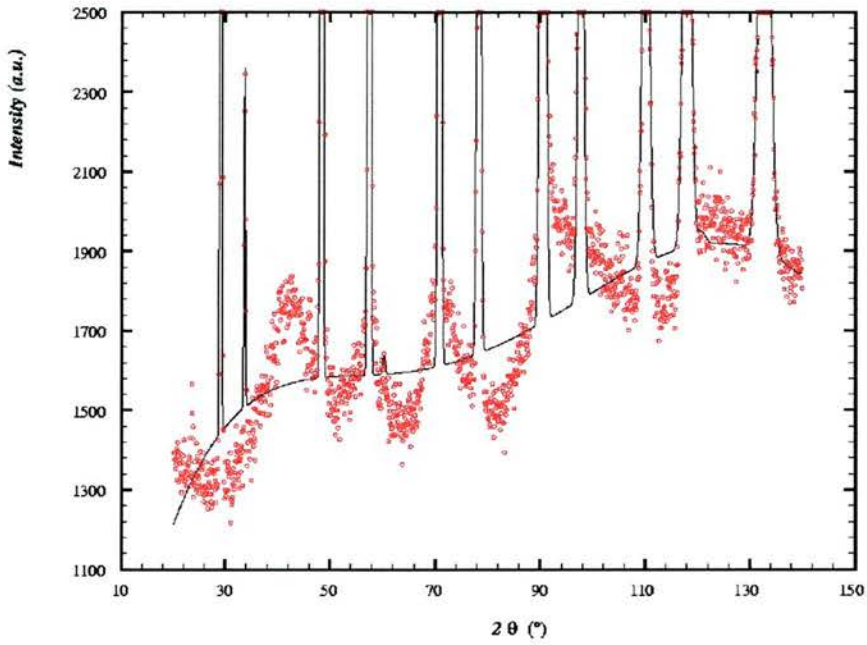


Figure 5.7 - $(\text{Sc}_2\text{O}_3)_{0.08}(\text{ZrO}_2)_{0.92}$ Baseline showing a clear modulation. The black line is the Rietveld fit and the red points are data.

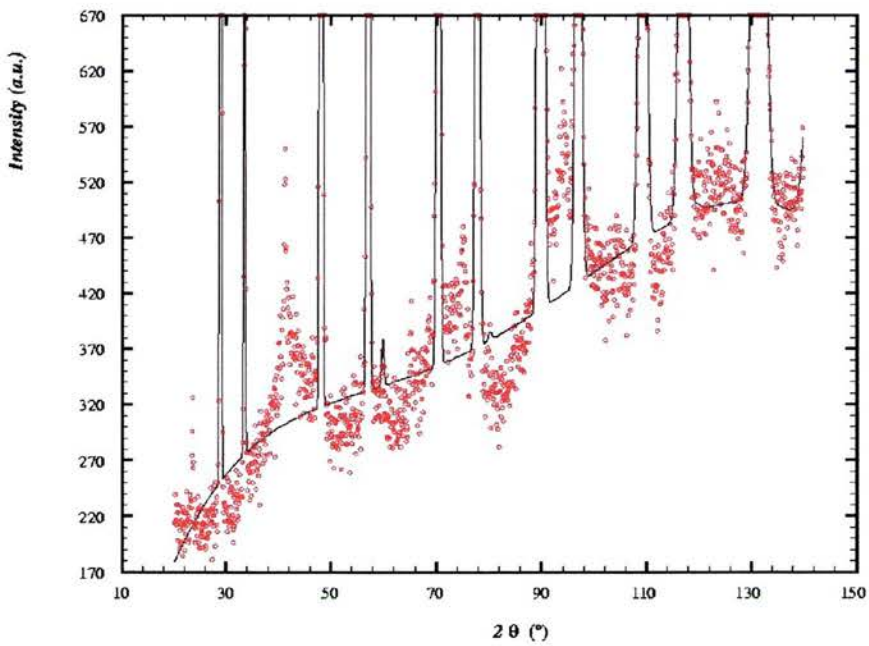


Figure 5.8 - $(\text{Sc}_2\text{O}_3)_{0.025}(\text{Y}_2\text{O}_3)_{0.075}(\text{ZrO}_2)_{0.9}$ Baseline showing a clear modulation. The black line is the Rietveld fit and the red points are data.

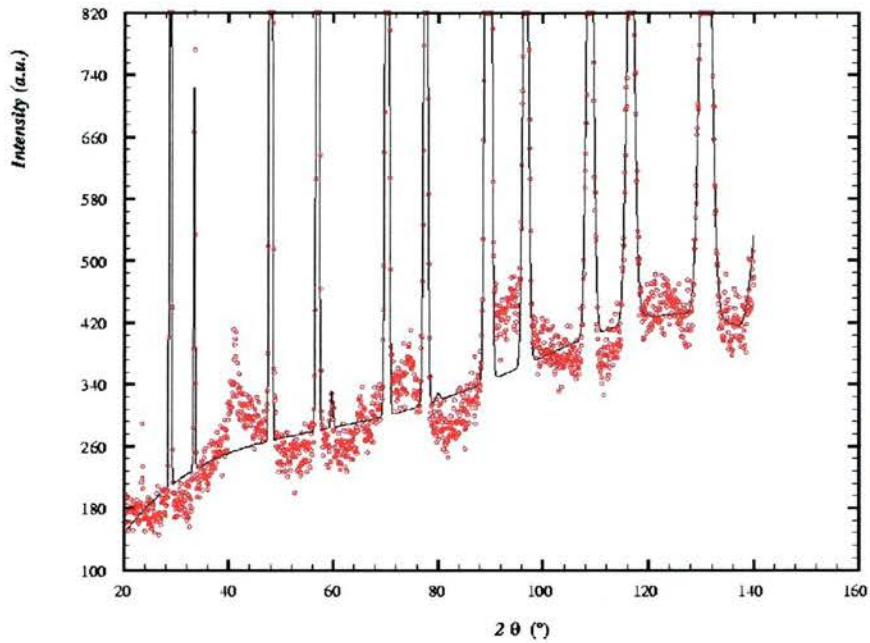


Figure 5.9 - $(\text{Sc}_2\text{O}_3)_{0.05}(\text{Y}_2\text{O}_3)_{0.05}(\text{ZrO}_2)_{0.9}$ Baseline showing a clear modulation . The black lines are the Rietveld fit and the red points are data.

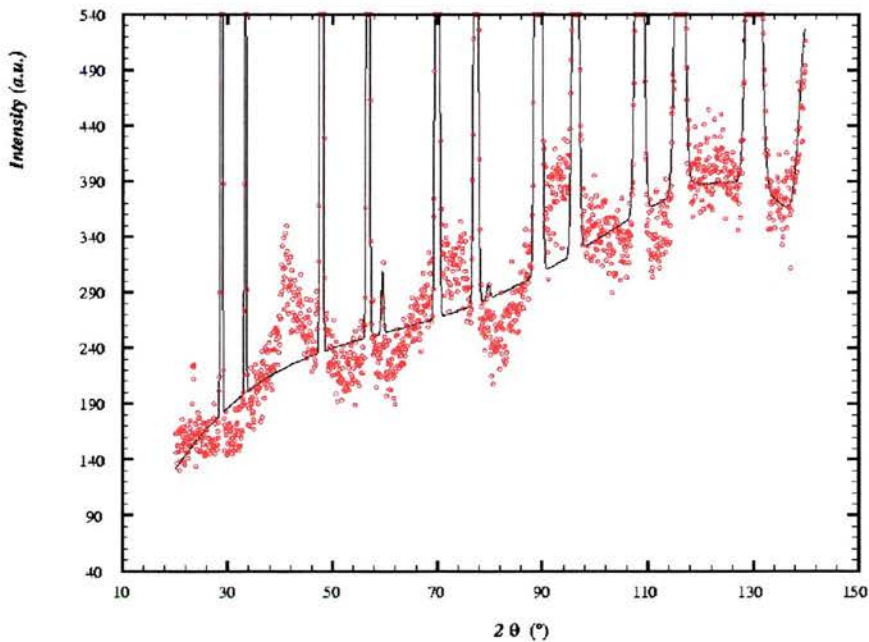


Figure 5.10 - $(\text{Sc}_2\text{O}_3)_{0.075}(\text{Y}_2\text{O}_3)_{0.025}(\text{ZrO}_2)_{0.9}$ Baseline showing a clear modulation . The black line is the Rietveld fit and the red points are data.

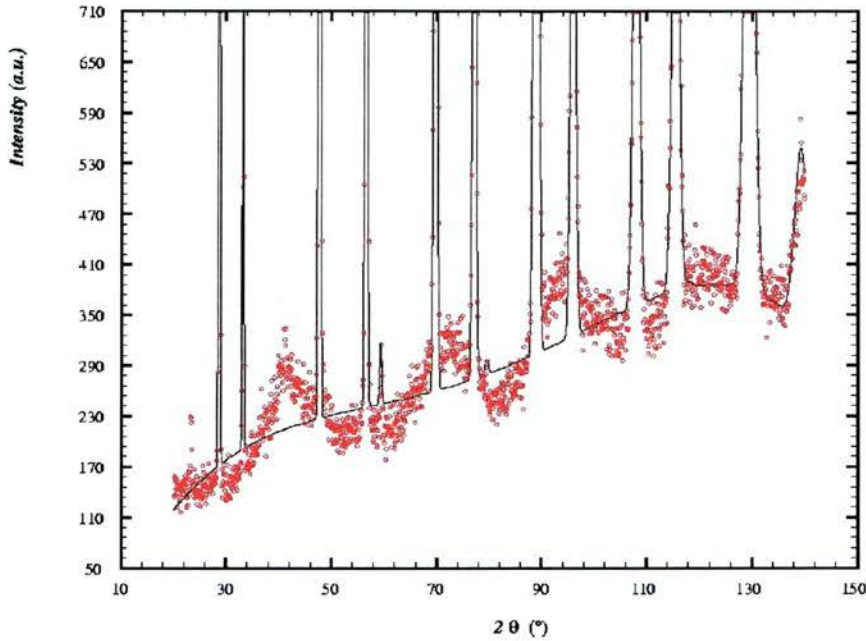


Figure 5.11 - $(\text{Y}_2\text{O}_3)_{0.1}(\text{ZrO}_2)_{0.9}$ Baseline showing a clear modulation . The black line is the Rietveld fit and the red points are data.

As can be seen from the backgrounds shown in figures 5.7 to 5.11, further work would be necessary to model the background correctly; however it should be noted that there is important structural information in this modulation.

All five patterns show an unusual modulation across the width of the spectrum. This pattern has not been previously reported in data from NPD so we do not believe it to be instrument related. The modulation shows peaks at 42° , 59° , 71° , 92° and 120° 2theta.

Discussion

The unusual modulation has not been reported before in zirconia systems, however Gibson and Irvine.⁷ reported diffuse scattering causing minor peaks in between the major peaks which they attributed to the formation of microdomains. Their pattern is reproduced in Figure 11.

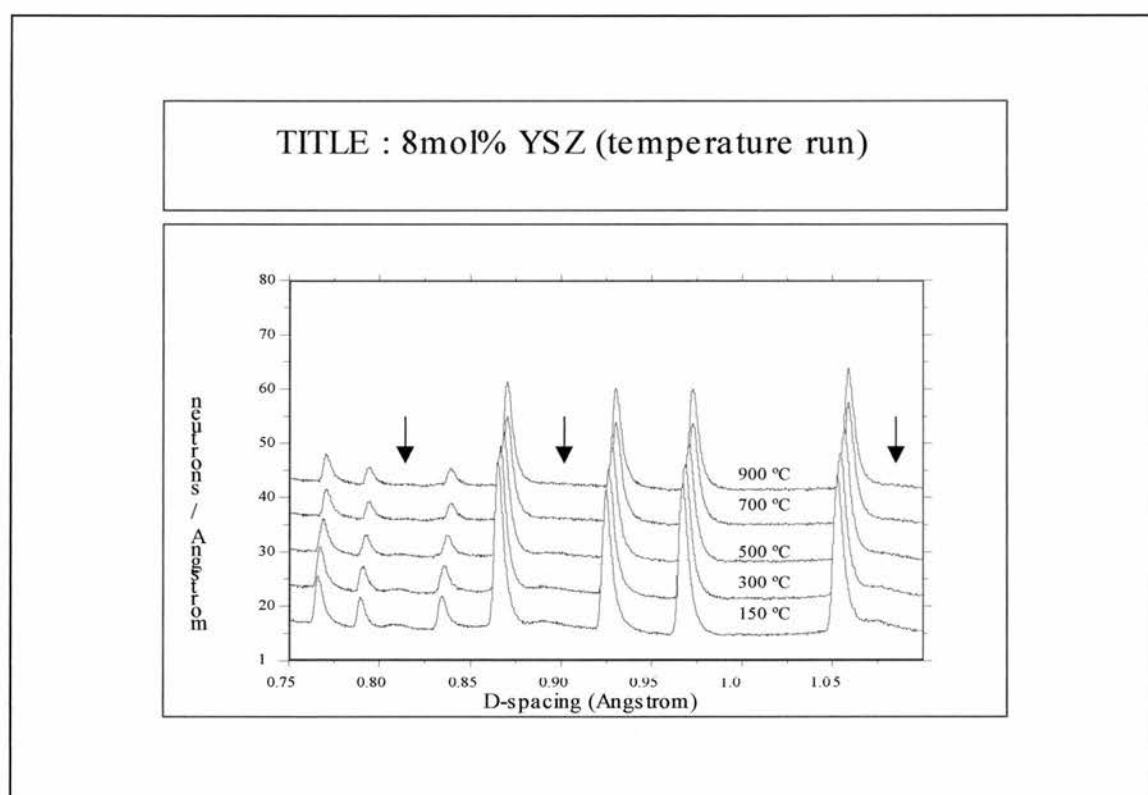


Figure 11 – Diffuse scattering peaks reported by Gibson and Irvine

The modulation in the background can possibly be explained by an ordering of oxygen vacancy (and perhaps the scandium) clusters into micro-domains. This will be discussed further in the next chapter.

References

- 1 T. H. Etsell and S.N. Flengas, *Chem. Rev.*, 1970, **70**, 339.
- 2 F. T. Ciacchi, S.P.S. Badwal and J. Drennan, *J. Eur. Ceram. Soc.*, 1991, **7**, 185.
- 3 S. Terauchi, H. Takizawa, T. Endo, S. Uchida, T. Terui and M. Shimada, *Mater. Lett.*, 1995, **23**, 273.
- 4 I. R. Gibson and J.T.S. Irvine, *J. Mater. Chem.*, 1996, **6**, 895.
- 5 S. García-Martín, M. A. Alario-Franco, D. P. Fagg, A. J. Feighery and J.T.S. Irvine, *Chem. Mater*, 2000, **12**, 1729.
- 6 J. T. S. Irvine, A. J. Feighery, D. P. Fagg and S. García-Martín, *Solid State Ionics*, 2000, **136/137**, 879.
- 7 I. R. Gibson and J.T.S. Irvine, *J. Mater. Chem.*, 1996, **6**, 895.

Discussion and Conclusions

DISCUSSION	185
CONCLUSIONS	187
REFERENCES	190

Discussion

The main focus of this study relates to the difference between the local structure and the overall bulk material. It is becoming increasingly apparent that the defect fluorite model is not correct in these systems, so the question becomes, what is the correct model?

The neutron diffraction work presented in the last chapter show an unusual modulation in the background which has been attributed to the formation of small regions where the vacancies have ordered in some manner, so-called microdomains. This is not a new idea, it was postulated by Gibson and Irvine¹ to explain small peaks in the neutron patterns of YSZ over a range of temperatures and it has been suggested by other workers before and since. The presence of the small peaks has been known since the 1970s.

The idea of microdomains has gained considerable currency recently and the focus of much research has turned to the nature and structure of the microdomains themselves. Drennan and Auchterlonie² reviewed the long running discussions on the

causes of the diffuse scattering peaks and came down on the side of microdomains of ordered oxygen vacancies. Electron microscopy evidence for these was presented.

Goff *et. al.*³ reported microdomains of roughly 15 angstroms across in YSZ, with a microdomain structure based on tetragonal zirconia in the yttrium region and a structure based on $Zr_3Y_4O_{12}$ in the higher yttrium region.

Garcia–Martin *et. al.*^{4,5} proposed two types of microdomains in the system $(1-x)Y_{0.5}Zr_{0.5}O_{1.75} - xY_{0.75}Nb_{0.25}O_{1.75}$ for $0 \leq x \leq 1$. In this case the zirconium end of the tie line had microdomains based on a structure similar to C-type. This smoothly changed to a structure based on pyrochlore as the solid solution moved towards the niobium end.

Villella *et. al.*⁶ reported that distortions around dopants were not necessarily the same as those around the host zirconium, data that this work agrees with completely. They also reported that the distortions were highly element specific. This also matches what was seen here, with strong differences between yttrium and scandium doping.

Zacate *et. al.*⁷ proposed that size effects were in fact dominant, along with oxygen lattice relaxation. They proposed that larger dopants would be NNN to vacancies and smaller dopants would be NN to the vacancies. The crossover point would be scandium. This matches what we have seen, with vacancies being NN to the zirconium rather than the larger yttrium in YSZ but an even spread of vacancies in ScSZ. This model makes no mention of clustering beyond this however, and a simple rule of size disagrees with the specification by Villella that effects are element specific.

Yamazaki *et. al.*⁸, working on the related system of ceria doped with Gd and Y proposed four different models, base on the fluorite system, but could not conclusively say which was preferable. No mention of microdomains was made, they preferred to talk about clusters around single or double vacancies.

All this work shows that the doping of zirconia and related materials is actually extremely complex, with many different structures being possible.

Conclusions

In the case of the materials reported here, it is interesting to note the good correlations between the data from the neutron diffraction and the EXAFS. This underlines the point that many different types of studies are required to fully elucidate any complete structural picture.

The neutron diffraction patterns show that there is some form of diffuse scattering. It also indicated an increase in cation disorder as the dopants were changed from yttrium to scandium. This is probably entirely due to the small scandium shifting off its ideal site.

The scandium will be shifting, because it must accommodate some change in local order. This change in local order is shown by the ScSZ EXAFS, where both metals are in co-ordination environments of less than eight. This was also seen in the co-doped system, where the co-ordination number of yttrium also fell. As this is not

possible in the defect fluorite structure, some form of local rearrangement to a MO_6 environment is probably occurring. The suggested system would be the rutile structure, that smaller cations take up in oxides. As this is not by broad band techniques such as XRD and neutron diffraction, it is probably happening in the microdomains.

Further EXAFS on the ScSZ system shows what appears to be a sharp phase change between the two highest conducting samples. This is attributed to a phase change in the microdomains, probably from tetragonal-like to a rhombohedral $\text{Sc}_2\text{Zr}_7\text{O}_{17}$ -like system.

Further work on this is extremely complex system is obviously required. The main experimental suggestion would be further collection of scandium edge data. This would be extremely time consuming, but would be worthwhile as there is certain to be more information in the refinements, if they were not so noisy.

This work was initially a study of potential SOFC electrolytes. While the work has diverged from this, a few points about it are worth raising.

Firstly, the borate doped YSZ, while an interesting system in its own right, is not a suitable electrolyte material due to its lower oxide ion conductivity than a comparable undoped YSZ and due to the stability problems discussed earlier. Even if this were not the case, the difficult preparation would probably prevent large-scale manufacture of the system.

On the remaining work, YSZ is already the electrolyte of choice test bed systems. Interestingly, Siemens – Westinghouse use 10 mol% YSZ, rather than the higher conducting 8 mol%, on the grounds of long term stability (ca 50,000 hours). It is well known that the conductivity of ScSZ degrades over time due to the precipitation of the low temperature rhombohedral phase, making it unsuitable for a commercial fuel cell.

Co-doping of yttria and scandia has shown itself to be an excellent idea, as it is single phase cubic and of very high conductivity. If the long term stability is as good as that of 10 mol% YSZ, something that has not been tested to date, then it is probably a more attractive electrolyte to the commercial sector than either YSZ, due to its higher conductivity, or many of the new perovskites currently being studied in academia. This is because of the increased conductivity coupled with the decades of experience in the technologies associated with a zirconia based electrolyte, much of which would have to be replaced if an entirely new class of electrolyte were to be used.

In conclusion, it is the considered opinion of the author that YScSZ is the most attractive electrolyte currently available for solid oxide fuel cells.

References

- 1 I. R. Gibson and J.T.S. Irvine, *J. Mater. Chem.*, 1996, **6**, 895.
- 2 J. Drennan and G. Auchterlonie, *Solid State Ionics*, 2000, **134**, 75.
- 3 J. P. Goff, W. Hayes, S. Hull, M. T. Hutchings and K. N. Clausen, *Phys. Rev. B* 1999, **59**, 104101.
- 4 S. García-Martín, M. A. Alario-Franco, D. P. Fagg, A. J. Feighery and J.T.S. Irvine, *Chem. Mater*, 2000, **12**, 1729.
- 5 J. T. S. Irvine, A. J. Feighery, D. P. Fagg, S. Garcia-Martin, *Solid State Ionics*, 2000, **136-137**, 879.
- 6 P. VILLELLA, S. D. Conradson, F. J. Espinosa-Faller, S. R. Foltyn, K. E. Sickafus and J. A. Valdez, *Phys. Rev. B* 2001, **64**, 104101.
- 7 M. O. Zacate, L. Minervini, D. J. Bradfield, R. W. Grimes and K. E. Sickafus, *Solid State Ionics*, 2000, **128**, 243.
- 8 S. Yamazaki, T. Matsui, T. Ohashi and Y. Arita, *Solid State Ionics*, 2000, **136-137**, 913.